DISSERTATION

INSIGHTS INTO THE BIOSPHERE-ATMOSPHERE EXCHANGE OF ORGANIC GASES FROM SEASONAL OBSERVATIONS OVER A PONDEROSA PINE FOREST

Submitted by

S. Ryan Fulgham

Department of Chemistry

In partial fulfillment of the requirements

For the Degree of Doctor of Philosophy

Colorado State University

Fort Collins, Colorado

Summer 2020

Doctoral Committee:

Advisor: Delphine Farmer

Jay M. Ham
Akkihebbal R. Ravishankara
Alan Van Orden

ABSTRACT

INSIGHTS INTO THE BIOSPHERE-ATMOSPHERE EXCHANGE OF ORGANIC GASES FROM SEASONAL OBSERVATIONS OVER A PONDEROSA PINE FOREST

The biosphere-atmosphere exchange of organic gases over forests contributes to the formation of air pollution and the availability of forest nutrients. Forests can be both sources and sinks of volatile and semi-volatile organic compounds to the atmosphere. The role that forests play in controlling organic acid concentrations remains poorly understood, with multiple model-measurement comparisons reporting missing sources of formic acid. Large, missing sources of organic acids have been identified over different forested environments. Despite substantial seasonal variability in forest productivity and environmental conditions, a paucity of observations, during seasons other than summertime, is available. Although forest fires are a major source of hazardous organic gases and particulate matter, few measurements of semi-volatile organic compounds emitted by forest fires are available from within 1 km of the fire. Detection further-afield cannot disambiguate between chemistry at the source of the fire and chemical aging as a smoke plume traverses the atmosphere. Near-field observations are needed to characterize emissions attributable to combustion and pyrolysis processes.

To improve understanding of processes that control the atmospheric budgets of organic acids, water-soluble pollutants with physicochemical properties similar to organic acids, and fire-emitted phenolic compounds, this dissertation reports measurements of the biosphere-atmosphere exchange of a suite of organic gases over a Rocky Mountain ponderosa pine forest in Colorado over four, seasonally-representative measurement campaigns. First, we report seasonally

persistent, upward fluxes of organic acids, which are neither explained by direct emissions nor secondary production. Second, we present evidence for equilibrium partitioning into and out of water films on forest surfaces as both a missing source and sink of isocyanic acid and small alkanoic acids. Finally, we report significant enhancement of organic acids, phenolic compounds, and other nitrogen containing compounds during initiation of a controlled forest fire compared with the remainder of the burn. Nitrated phenols are rapidly produced and enhanced more than phenolic precursors during initial, higher temperature conditions. We attribute greater enhancement of nitrated phenols to high NO_x emissions under higher temperature conditions.

ACKNOWLEDGEMENTS

Without the encouragement I received and discipline that I learned from my mother, Vickie Watts, stepfather, Charles Watts, and grandparents, Alex and Virginia Gonzales, I would not have developed the confidence and determination needed to succeed in graduate school. I also acknowledge the untimely loss of my mother in October 2016 and grandmother in October 2019 as well as the countless sacrifices they made for me. I dedicate this work in part as a capstone to the education they envisioned for me. I thank my wife, Raven Bough, and our mischievous, but loving, dog-children, Effie and Merle, for their love and steadfast emotional support no matter how crazy I may have seemed / been at the time. I thank Dr. Michael Link for becoming my best friend in Colorado. His reliable scientific knowledge, adventurous spirit, and commitment to self-growth have enriched my life. I thank my past mentors, Dr. Nina Baghai-Riding, Dr. Chuck Smithhart, Dr. Joe Bentley, and Lacey Fitts for being generous with their time outside of the classroom. They gave me my first taste of research and stimulated my scientific curiosity. I thank my sister and brother-in-law, Ashley and Jeff Laurenzo, for their friendship and for acting as the foundation of my family, particularly through difficult losses and changing family dynamics. I thank my spiritual mentor, Dave Alford, for always being there to listen and laugh at me when I needed him to. I thank my academic mentors, Dr. Delphine Farmer and Dr. Ingrid Ulbrich, for teaching an unsophisticated person like me how to become a professional scientist, both in practice and identity. I thank the Farmer Group for being consummate colleagues and, in recent years, epitomizing positivity. Last, but certainly not least, I thank death metal for brutalizing me every step of the way.

DEDICATION

I dedicate this work in memory of Cora Bell, my first high school Chemistry teacher. Her hard work teaching and advocating for science inspired students of all ages and skin colors in our racially divided Mississippi school districts. Mrs. Bell convinced me that I could be a good chemist and set me on the educational path that culminates with this dissertation.

TABLE OF CONTENTS

CHAPTER 1

INTRODUCTION TO THE ROLE OF FORESTS IN ATMOSPHERIC CHEMISTRY AND THE IMPORTANCE OF ATMOSPHERIC MEASUREMENTS OVER FORESTS

1.1 Forests and atmospheric chemistry

Among the most widespread ecotypes on Earth, forests cover 4.06×10^9 ha, or >30% of all terrestrial environments.[1] The United States alone has 360×10^6 ha of forested land, or 33% of the total land area.[2] Most of the carbon in the terrestrial biosphere is stored in forests, both as living (600 - 1000 Pg (petagrams)) and dead (1200 Pg) biomass – nearly three times the amount of carbon in the atmosphere (>700 Pg).[3] Of the atmospheric carbon, forests emit approximately half of all reactive carbon into the atmosphere and ~10 times more volatile organic compounds (VOCs) than all VOC emissions of anthropogenic origin.[4,5] The vast majority of reactive carbon emitted from forests is ultimately converted to CO_2. This is one way forests impact the global radiative budget. Forests also drive the chemistry of the atmosphere. Conversion of emissions from forested environments proceeds by reactions with atmospheric oxidants, a process that impacts air quality, stratospheric ozone, and global climate. Forest VOC emissions photo-oxidize to produce tropospheric ozone (in the presence of nitrogen oxides (NO_x)) and organic particulate matter, both contributors to poor air quality.[6,7]

Human activities in the Anthropocene perturb the chemistry of the atmosphere and produce deleterious effects on forests. Acid precipitation is a noteworthy example. As human activities industrialized, the burning of fossil fuels increased in importance for the generation of power and heat. Fossil fuel burning emits large quantities of sulfur dioxide (SO_2) and NO_x into the atmosphere, which are readily oxidized to form sulfuric acid (H_2SO_4) and nitric acid

(HNO_3).[8] These pollutants are removed from the lower atmosphere by wet and dry deposition and increase the acidity of precipitation. In the United States, acid deposition damaged red spruce, sugar maple, and yellow cedar trees in the Northeastern temperate forests, reduced the pH of lakes and streams, and reduced populations of pH-sensitive microbes, invertebrates, and animals.[9,10] Nitrogen deposition is another major source of pollution damaging to forests. Following the advent of the Haber-Bosch process of artificial nitrogen fixation process in 1909, human production of ammonia led to significant increases in emissions.[11] Because nitrogen is frequently a limiting nutrient, ammonia is predominately applied to agricultural fields for nitrogen fertilization, from which a large fraction is volatilized to the atmosphere. These reduced nitrogen emissions in concert with NO_x emissions from combustion engines of cars, trucks, and heavy equipment, ultimately deposit nitrogen to forests, which shifts nutrient balances and acidifies soils and water bodies. Enhanced nitrogen in forest nutrient balances can lead to nitrogen saturation, which is linked to forest decline.[12] Excess nitrogen can induce other nutrient imbalances in leached calcium, mobilized aluminum, and magnesium.[13] Besides impacting climate and human health, ozone is toxic to plants by inducing stomatal closure and shutting down photosynthesis.[14] Ozone is mainly produced chemically through oxidation of methane, carbon monoxide, and VOCs by hydroxyl radical (OH) in the presence of NO_x. Ozone concentrations in the lower troposphere have tripled since preindustrial times.[15] Ozone pollution can be exacerbated regionally by high NO_x pollution from urban areas upwind of forests.[16] Although VOC emissions from forests contribute to ozone formation, they also destroy ozone through ozonolysis reactions. However, reactions of ozone with VOCs produce oxygenated VOCs, which enhance the formation of secondary organic aerosol, a pollutant.[17]

Observations of gases and particles over forests have identified and verified many of the important contributions forests make to the chemistry of the atmosphere. For example, larger concentrations of OH have been measured over forests than predicted by chemical models.[18] This discovery stimulated research of the oxidation pathways of isoprene, which accounts for approximately one-third of all biogenic VOC emissions. Extensive, process-level research led to improved model-measurement agreement. Forest measurements have revealed the damage human activity has done to forested environments. At Hubbard Brook Experimental Forest, Gene Likens and colleagues showed foliar damage and acidification of lakes and streams from acid deposition.[19] At Rocky Mountain National Forest in Colorado, flux measurements of reactive nitrogen showed that local agriculture and transportation pollution have a negative impact on ecosystem health and park visibility.[20] Field surveys of many forests have shown foliar damage by ozone.[21]

Measurements over forests are needed to reconcile ongoing questions in atmospheric chemistry. Daily and seasonal variability in isoprene emissions is not captured by current model parameterizations in some forested environments.[22] Large upward fluxes of organic acids over coniferous, deciduous, and mixed canopy forests suggest an unknown source of organic acids.[23–25] Measurements of bi-directional particle fluxes over forests challenge deposition-only aerosol models and point to a need for observations of in-canopy sources and sinks.[26] To protect forests, improve forest management strategies with respect to air quality and climate, and to better understand the role forests play in atmospheric chemistry, more observational studies are needed.

1.2 Dissertation overview

This dissertation presents seasonally representative measurements of organic gases over a Rocky Mountain ponderosa pine forest and explores processes that contribute to biosphere-atmosphere exchange.

In Chapter 2 we measured eddy covariance fluxes of oxidized volatile organic compounds over a ponderosa pine forest in Colorado over four, seasonally representative measurement campaigns in 2016. Observations point to an underestimated ecosystem source of organic acids (e.g. in-canopy chemistry of large or multifunctional terpenoids), an overestimated dry deposition sink (potentially due to the arid environment), and/or an unresolved sink of organic acids in the upper boundary layer. Forests are potentially large sources of atmospheric organic acids in warmer seasons, but further investigation into dry deposition mechanisms and in-canopy chemistry is warranted.

Chapter 3 presents evidence that water films and dew droplets on surfaces in a ponderosa pine forest act as both sources and sinks of small gaseous organic acids, including isocyanic acid, by an equilibrium phase-partitioning process.

Chapter 4 reports rapid formation of gaseous nitrated phenolic compounds from a controlled forest fire when the fire is at its hottest and produces NO_x most efficiently.

REFERENCES

(1) FAO. *Global Forest Resources Assessment 2020: Key Findings*; FAO: Rome, Italy, 2020. https://doi.org/10.4060/ca8753enAlso Available in:Spanish French.

(2) Jaffe, D. A.; O'Neill, S. M.; Larkin, N. K.; Holder, A. L.; Peterson, D. L.; Halofsky, J. E.; Rappold, A. G. Wildfire and Prescribed Burning Impacts on Air Quality in the United States. *J. Air Waste Manag. Assoc.* **2020**, *70* (6), 583–615. https://doi.org/10.1080/10962247.2020.1749731.

(3) Falkowski, P.; Scholes, R. J.; Boyle, E.; Canadell, J.; Canfield, D.; Elser, J.; Gruber, N.; Hibbard, K.; Högberg, P.; Linder, S.; Mackenzie, F. T.; Iii, B. M.; Pedersen, T.; Rosenthal, Y.; Seitzinger, S.; Smetacek, V.; Steffen, W. The Global Carbon Cycle: A Test of Our Knowledge of Earth as a System. *Science* **2000**, *290* (5490), 291–296. https://doi.org/10.1126/science.290.5490.291.

(4) Goldstein, A. H.; Galbally, I. E. Known and Unexplored Organic Constituents in the Earth's Atmosphere. *Environ. Sci. Technol.* **2007**, *41* (5), 1514–1521. https://doi.org/10.1021/es072476p.

(5) Guenther, A. The Contribution of Reactive Carbon Emissions from Vegetation to the Carbon Balance of Terrestrial Ecosystems. *Chemosphere* **2002**, *49* (8), 837–844. https://doi.org/10.1016/S0045-6535(02)00384-3.

(6) Kavouras, I. G.; Mihalopoulos, N.; Stephanou, E. G. Formation of Atmospheric Particles from Organic Acids Produced by Forests. *Nature* **1998**, *395* (6703), 683–686. https://doi.org/10.1038/27179.

(7) Fares, S.; McKay, M.; Holzinger, R.; Goldstein, A. H. Ozone Fluxes in a Pinus Ponderosa Ecosystem Are Dominated by Non-Stomatal Processes: Evidence from Long-Term Continuous Measurements. *Agric. For. Meteorol.* **2010**, *150* (3), 420–431. https://doi.org/10.1016/j.agrformet.2010.01.007.

(8) Galloway, J. N. Atmospheric Acidification: Projections for the Future. *Ambio* **1989**, *18* (3), 161–166.

(9) Hawley, G. J.; Schaberg, P. G.; Eagar, C.; Borer, C. H. Calcium Addition at the Hubbard Brook Experimental Forest Reduced Winter Injury to Red Spruce in a High-Injury Year. *Can. J. For. Res.* **2006**, *36* (10), 2544–2549. https://doi.org/10.1139/x06-221.

(10) Houle, D.; Tremblay, S.; Ouimet, R. Foliar and Wood Chemistry of Sugar Maple along a Gradient of Soil Acidity and Stand Health. *Plant Soil* **2007**, *300* (1), 173–183. https://doi.org/10.1007/s11104-007-9401-7.

(11) Sutton, M. A.; Erisman, J. W.; Dentener, F.; Möller, D. Ammonia in the Environment: From Ancient Times to the Present. *Environ. Pollut.* **2008**, *156* (3), 583–604. https://doi.org/10.1016/j.envpol.2008.03.013.

(12) Aber, J. D.; Nadelhoffer, K. J.; Steudler, P.; Melillo, J. M. Nitrogen Saturation in Northern Forest EcosystemsExcess Nitrogen from Fossil Fuel Combustion May Stress the Biosphere. *BioScience* **1989**, *39* (6), 378–386. https://doi.org/10.2307/1311067.

(13) Nodvin, S. C.; Van Miegroet, H.; Lindberg, S. E.; Nicholas, N. S.; Johnson, D. W. Acidic Deposition, Ecosystem Processes, and Nitrogen Saturation in a High Elevation Southern Appalachian Watershed. *Water. Air. Soil Pollut.* **1995**, *85* (3), 1647–1652. https://doi.org/10.1007/BF00477216.

(14) Sadiq, M.; Tai, A. P. K.; Lombardozzi, D.; Val Martin, M. Effects of Ozone-Vegetation Coupling on Surface Ozone Air Quality via Biogeochemical and Meteorological Feedbacks. *Atmospheric Chem. Phys.* **2017**, *17* (4), 3055–3066.

(15) Lombardozzi, D.; Levis, S.; Bonan, G.; Hess, P. G.; Sparks, J. P. The Influence of Chronic Ozone Exposure on Global Carbon and Water Cycles. *J. Clim.* **2015**, *28* (1), 292–305. https://doi.org/10.1175/JCLI-D-14-00223.1.

(16) Böhm, M.; McCune, B.; Vandetta, T. Ozone Regimes in or near Forests of the Western United States: I. Regional Patterns. *J. Air Waste Manag. Assoc.* **1995**, *45* (4), 235–246. https://doi.org/10.1080/10473289.1995.10467363.

(17) Kroll, J. H.; Ng, N. L.; Murphy, S. M.; Flagan, R. C.; Seinfeld, J. H. Secondary Organic Aerosol Formation from Isoprene Photooxidation. *Environ. Sci. Technol.* **2006**, *40* (6), 1869–1877. https://doi.org/10.1021/es0524301.

(18) National Academies of Sciences, E., and Medicine. *The Future of Atmospheric Chemistry Research: Remembering Yesterday, Understanding Today, Anticipating Tomorrow*; The National Academies Press: Washington, DC, 2016. https://doi.org/10.17226/23573.

(19) Likens, G. E.; Bormann, F. H. Acid Rain: A Serious Regional Environmental Problem. *Science* **1974**, *184* (4142), 1176–1179. https://doi.org/10.1126/science.184.4142.1176.

(20) Benedict, K. B.; Carrico, C. M.; Kreidenweis, S. M.; Schichtel, B.; Malm, W. C.; Collett, J. L. A Seasonal Nitrogen Deposition Budget for Rocky Mountain National Park. *Ecol. Appl.* **2013**, *23* (5), 1156–1169. https://doi.org/10.1890/12-1624.1.

(21) Chappelka, A. H.; Samuelson, L. J. Ambient Ozone Effects on Forest Trees of the Eastern United States: A Review. *New Phytol.* **1998**, *139* (1), 91–108. https://doi.org/10.1046/j.1469-8137.1998.00166.x.

(22) Pressley, S.; Lamb, B.; Westberg, H.; Flaherty, J.; Chen, J.; Vogel, C. Long-Term Isoprene Flux Measurements above a Northern Hardwood Forest. *J. Geophys. Res. Atmospheres* **2005**, *110* (D7). https://doi.org/10.1029/2004JD005523.

(23) Alwe, H. D.; Millet, D. B.; Chen, X.; Raff, J. D.; Payne, Z. C.; Fledderman, K. Oxidation of Volatile Organic Compounds as the Major Source of Formic Acid in a Mixed Forest Canopy. *Geophys. Res. Lett.* **2019**, *46* (5), 2940–2948. https://doi.org/10.1029/2018GL081526.

(24) Schobesberger, S.; Lopez-Hilfiker, F. D.; Taipale, D.; Millet, D. B.; D'Ambro, E. L.; Rantala, P.; Mammarella, I.; Zhou, P.; Wolfe, G. M.; Lee, B. H.; Boy, M.; Thornton, J. A. High Upward Fluxes of Formic Acid from a Boreal Forest Canopy. *Geophys. Res. Lett.* **2016**, 2016GL069599. https://doi.org/10.1002/2016GL069599.

(25) Fulgham, S. R.; Brophy, P.; Link, M.; Ortega, J.; Pollack, I.; Farmer, D. K. Seasonal Flux Measurements over a Colorado Pine Forest Demonstrate a Persistent Source of Organic Acids. *ACS Earth Space Chem.* **2019**. https://doi.org/10.1021/acsearthspacechem.9b00182.

(26) Walker, J. T.; Beachley, G.; Zhang, L.; Benedict, K. B.; Sive, B. C.; Schwede, D. B. A Review of Measurements of Air-Surface Exchange of Reactive Nitrogen in Natural Ecosystems across North America. *Sci. Total Environ.* **2020**, *698*, 133975. https://doi.org/10.1016/j.scitotenv.2019.133975.

CHAPTER 2

SEASONAL FLUX MEASUREMENTS OVER A COLORADO PINE FOREST DEMONSTRATE A PERSISTENT SOURCE OF ORGANIC ACIDS[1]

2.1 Introduction

Organic acids are both numerous and omnipresent in the lower troposphere.[1–6] Organic acids are molecules with one or more carboxylic acid functional groups and may account for ~25% of non-methane volatile organic compounds globally in the gas and particle phases.[3] Organic acids can comprise up to 50% of organic aerosol mass, particularly in areas dominated by biogenic emissions.[7,8] This contribution to aerosol loading impacts global climate and air quality, and thus human and ecosystem health.[9,10] Organic acids contribute to free acidity and cloud water acidity and deplete condensed hydroxyl radical (OH) concentrations in clouds.[3,11,12] Their impacts on the carbon cycle, human health, and ecosystem health are well known, but the atmospheric budgets of organic acids are poorly understood. Atmospheric models consistently underpredict measured ambient concentrations of formic acid, suggesting an underestimation of sources and/or an overestimation of sinks.[12–15] Studies of organic acids, other than formic and acetic acids, remain largely unexplored from both modeling and measurement approaches.[16]

Atmospheric organic acids have primary and secondary sources that are both biogenic and anthropogenic. Terrestrial ecosystems provide several primary, biogenic sources of organic acids. Terrestrial vegetation emits formic acid on the order of 2–8 nmol m^{-2} min^{-1} per plant and globally 0.9–6 Tg yr^{-1}.[17–20] Formic, acetic, propionic, butyric, lactic, and keto acids are common

[1]Fulgham, S.R., Brophy, P., Link, M.F., Ortega, J., Pollack, I., Farmer, D.K., 2019. Seasonal flux measurements over a Colorado pine forest demonstrate a persistent source of organic acids. ACS Earth and Space Chemistry, 3(9), pp.2017-2032.

volatile products of soil microbes and are emitted from a variety of soils and leaf litters.[21,22] Ants of the Formicinae subfamily are estimated to contribute to global formic acid emissions of 0.6 Tg yr^{-1}.[23] Primary, anthropogenic organic acid sources include a variety of industrial chemical processes and combustion reactions. Secondary oxidation of hydrocarbons is a prolific source of organic acids.[1,12,14,15] Formation reactions include ozonolysis of unsaturated hydrocarbons,[24,25] reactions between stabilized Criegee intermediates and water vapor,[26] and addition of OH to carbonyl groups in the aqueous phase.[11,27] Monoterpene reactions with OH produce short-chain organic acids, including formic, acetic, butyric and methacrylic acid.[28] While the chemical mechanisms remain unclear, photooxidation of acetone has been found to be a source of formic acid.[29] Biomass burning is also a source of both organic acids and precursor molecules.[30] Overall, Stavrakou et al. estimate global atmospheric sources of formic acid to be 36 Tg yr^{-1}: 69% biogenic, 11% direct anthropogenic, 8% direct pyrogenic, and 12% indirect anthropogenic and pyrogenic.[15]

Several sinks are known to remove organic acids from the atmosphere. Short-chain, water-soluble organic acids are primarily removed by wet deposition.[16] For example, total organic acids account for 118–244 TgC yr^{-1} lost to wet deposition.[31] Dawson and Farmer derive an average lifetime for formic acid with respect to wet deposition of 5 days.[32] Dry deposition of organic acids is poorly constrained by measurements but is estimated as equivalent to wet deposition.[31] Global formic acid removal rates by dry deposition have been estimated at 12.7–49.5 Tg yr^{-1}, corresponding to a lifetime of 7–14 days.[15] Many short-chain alkanoic acids are relatively inert to atmospheric oxidation. For example, the atmospheric lifetime of formic acid to photochemical oxidation by OH is ~30 days.[14,33] However, many keto acids, unsaturated acids, and longer-chained organic acids react more favorably with OH.[34] Alkanoic acids, like acetic

acid, dominantly react with OH by deprotonation of the acidic hydrogen; similar reactions may also occur for other small alkanoic acids.[35] The multifunctional, oxygenated products of these reactions possess lower volatility and thus efficiently uptake onto particulate matter and cloud droplets.[36]

Model studies incorporate these production and loss processes to investigate the scientific community's understanding of atmospheric organic acids. Most work focuses on formic and/or acetic acids in the summer, consistently finding large discrepancies between model predictions and measurements. Using satellite measurements and a global chemical transport model, Stavrakou et al. find that the standard model misses 100 Tg yr^{-1} of formic acid production worldwide and suggest terpene oxidation is the missing source.[15] Adding isoprene oxidation mechanisms to a global model also underpredicts formic acid, particularly in the northern midlatitudes.[12] Both studies ascribe underpredictions to multiphase chemistry and subsequent loss of formic acid during aerosol aging. Millet et al. add even more formation mechanisms, including formation from stabilized Criegee intermediates and tautomerization of acetaldehyde, to a chemical transport model but still underestimate measurements over a deciduous forest in Alabama.[14] RO_2+OH reactions pose an intriguing organic acid source, but one with such large uncertainty and shallow vertical gradients that these reactions are unlikely the cause of model-measurement discrepancy for formic acid in the boundary layer.[14] As such, Millet et al. show a model-measurement disagreement so large that unrealistic changes to the model are needed to close the discrepancy – for example, increasing isoprene chemistry sources by a factor of 3 or plant emissions by a factor of 26.[14]

Tower-based measurements of ambient organic acids can provide insight into landscape sources and sinks. Canopy-scale eddy fluxes are direct measurements of net vertical exchange

over a forest – i.e. the difference of local sources and sinks. Several studies have measured organic acid fluxes by direct eddy covariance.[6,13,37–43] Most researchers report bi-directional formic acid fluxes with the bulk of the studies finding net deposition. For example, Alwe et al. found upward fluxes dominated during warm and dry conditions over a mixed-canopy forest, potentially due to in-canopy chemistry.[13] Schobesberger et al. observed large net emissions of formic acid over a boreal forest canopy in Hyytiälä, Finland;[6] and observations by Nguyen et al. could account for only half of the expected deposition over an Alabama forest.[40] Mattila et al. noted vertical gradients over a peri-urban site during both daytime and nighttime in Colorado consistent with a surface source of formic acid.[44] These studies point to a large, missing atmospheric source of formic acid.

Previous work has been limited to formic and/or acetic acids, likely due to their prevalence in the atmosphere and ease of calibration. However, organic acids in the atmosphere are diverse, and cover a range of relevant chemical properties (e.g. Henry's Law constant, solubility, vapor pressure).[8,45–49] They present an intriguing opportunity to probe not only ecosystem sources of organic acids, but also the potential of chemical properties of gas-phase molecules to control their sinks.

A key challenge in probing sources and sinks of organic acids is the lack of seasonal data coverage. Most published flux measurements are conducted in summer, when plant photosynthetic activity and ecosystem sources are likely at a maximum – and are typically limited to days or weeks due to high demand for labor, computational power, and instrument availability coupled with filtering of data for quality assurance. This may lead to an inherent bias in estimates of terrestrial sources and sinks.

To this end, we conducted the Seasonal Particles in Forests Flux studY (SPiFFY), with the aim of investigating interactions between semi-volatile organic compounds and particle fluxes over a sub-alpine forest across multiple seasons. Here, we present seasonally representative eddy covariance flux measurements of six organic acids: formic, propionic, methacrylic, butyric, valeric, and heptanoic acids from a ponderosa pine forest where total VOCs are dominated by monoterpene and 2-methyl-3-buten-2-ol (MBO) emissions. To constrain primary sources of the six organic acids, we measured direct emissions of the acids from pine trees and soils with branch and soil enclosures. We reproduce observed fluxes via implementing temperature-dependent parameterizations. Finally, we construct flux budgets for the six acids to explore the relative importance of different sources and sinks for the organic acids across the seasons.

2.2 Site description

SPiFFY consisted of four, seasonally-representative intensive measurement campaigns at the Manitou Experimental Forest Observatory (MEFO): winter (1 February – 1 March 2016), spring (15 April – 15 May 2016), summer (15 July – 15 August 2016), and fall (1 October – 1 November 2016). A preliminary summer campaign took place in 2015 (1 July – 15 August 2015) and was used to pilot these experiments; however, only measurements from the 2016 campaign that were optimized for data collection in this environment are utilized in this analysis. Manitou Experimental Forest Observatory (39.1006 °N, 105.0942 °W) is an atmospheric observation station located in central Colorado, U.S.A. Semi-arid, sub-alpine (2280–2840 m above sea level) Rocky Mountain ponderosa pine forest surrounds the site to the north, south, and west. Ortega et al. provide a detailed description of both the site and forest.[50] Average canopy height at the measurement location was approximately 16 m with sparse coverage. Various herbaceous and woody plants grew in the understory. Approximately 1 km to the east of MEFO is a creek

drainage and Colorado state highway 67. The two-lane highway typically experienced light traffic from recreational vehicles, forest workers, and local residents.

Seasonal meteorology is summarized in Table 2.1. Temperature changed substantially between seasons: -1±8 °C (mean±standard deviation) in winter, 4±7 °C in spring, 20±7 °C in summer, and 8±8 °C in fall. The maximum recorded temperature (30 m above ground level, a.g.l.) during our study was 30 °C (17 July 2016), and the minimum recorded temperature (30 m a.g.l.) was -22 °C (3 February 2016). Means of relative humidity range from 50–70% for all seasons. Nighttime relative humidity rarely exceeded 80%; daytime relative humidity seldom falls below 20%. Seasonal variability in ambient temperature and relative humidity is shown in Figure 2.1. Consistent with previous observations at the site, daytime winds predominantly traveled from north to south.[50] At night, above-canopy winds drained towards the north. Average wind speeds (30 m a.g.l.) were light to gentle-moderate (<4.0 m s^{-1}). Total annual rainfall at the site was 30 cm in 2016.[51] Light afternoon thunderstorms frequently occurred in summer, with cumulative precipitation of 2 cm during the summer campaign. Light snowfall (<10 cm total precipitation) occurred at the beginning of October 2016, otherwise the fall campaign was devoid of precipitation. Two substantial snowstorms (>30 cm accumulation per event) happened during both winter and spring (3–4 and 23 February 2016, 15–16 April 2016, and 28 April – 1 May 2016). Most of the snow cover melted between storms. Characteristic of the Colorado Front Range, sunny days persisted at Manitou. Down-welling photosynthetic photon flux density (PPFD) at 3 m a.g.l. regularly exceeded 1000 µmol m^{-2} s^{-1} during all seasons characterized in this work.

We installed sonic anemometers and inlets for flux measurements on the 30 m walk-up ‘chemistry’ tower at the Manitou site, with instruments housed in a nearby mobile trailer. We

also collected measurements of nitrogen oxides (NO_x=NO+NO_2), ozone (O_3), carbon monoxide (CO), and sulfur dioxide (SO_2) during these seasonal experiments. Descriptions for these measurements are in appendix (A1.2). Section 2.4 contains details of the estimated flux footprint.

2.3 Measurements

2.3.1 Organic acid measurements

We measured gaseous formic {HCOOH}, propionic {CH_3CH_2COOH}, methacrylic {$CH_3C(CH_2)COOH$}, butyric {$CH_3(CH_2)_2COOH$}, valeric {$CH_3(CH_2)_3COOH$}, and heptanoic acids {$CH_3(CH_2)_5COOH$} with an acetate high resolution time-of-flight chemical ionization mass spectrometer (hereafter referred to as CIMS; Tofwerk AG and Aerodyne Research, Inc.). We used acetate reagent ions throughout SPiFFY, except during five days in summer and three days during fall when we used iodide reagent ion chemistry. This manuscript focuses only on acetate CIMS data. The sensitivity of acetate CIMS does not substantially depend upon ambient water vapor concentrations unlike I^-, CF_3O^-, and H_3O^+ CIMS, which have typically been used for previous flux measurements. Importantly, we note that while acetate CIMS cannot distinguish between structural isomers, the technique has little sensitivity to most other functional groups, so we relate signals to their most likely detected structures (i.e. carboxylic acids). However, some of these structures do have multiple structural isomers that maintain the acidic functionality. For example, we detect the deprotonated product of $C_4H_8O_2$, which represents the sum of butyric and isobutyric acid (hereafter referred to as "butyric acid" for simplicity); other isomers, such as acetoin, do not possess adequately acidic hydrogen atoms for detection by acetate reagent ions. Similarly, $C_7H_{14}O_2$ (hereafter referred to as "heptanoic acid" for simplicity) represents the sum of all C_7-alkanoic acids. Both CIMS and acetate ionization mechanisms are described thoroughly elsewhere and are briefly described here.[52–55]

In this technique, sample air enters the ion-molecule reactor (IMR, 70 mbar) and mixes with an orthogonal stream of acetate reagent ions. Acetate reagent ions are thought to initially cluster in the IMR and then decluster in the atmospheric pressure interface to produce declustered, deprotonated analyte ions further downstream in the CIMS.[53] Ionized analytes pass through both short and big segmented, RF-only quadrupoles before entering a series of ion transfer lenses. A voltage drop of 19 V between the ion lenses (skimmer and 2nd quadrupole entrance plate) keeps the CIMS in a declustering mode, minimizing the detection of acetate-analyte clusters. After transmission, sample ions are orthogonally extracted, separated, and detected in the time-of-flight (ToF) region. Signal from the micro-channel plate detector (Photonis Inc.) is amplified by 11x, pre-averaged on an analog-to-digital converter (ADQ 1600, SP Devices), transferred to a computer (Dell Technologies, Inc.) by USB 2.0, and extracted at 15 kHz into the data acquisition system (ToFDAQ). All measurements are averaged to 5 Hz time resolution. Mass resolutions >3.5x10^3 (m/Δm) and total counts >8x10^5 ions per spectrum are maintained during winter, spring, and the first two weeks of summer, at which point instrument sensitivity dropped to 2x10^5 ions per spectrum for the duration of the study.

A reduced pressure inlet (Figure A1.1), similar to that described by Brophy and Farmer, samples air, although a durable perfluoroalkoxy alkane (PFA) inlet replaces the glass inlet.[52] Gases and particles enter a 1/4 in. PFA three-way tee (Swagelok) and flow through 11 cm of 1/8 in. i.d. (1/4 in. o.d.) fluorinated ethylene propylene (FEP) tubing. The flow is split with a sample bypass flow (40 L min^{-1}, volumetric flow; 30 L min^{-1}, standard flow), removing gases orthogonally from the main flow line with the aim of minimizing particle interferences, and a particle bypass flow (10 L min^{-1}), pulling additional sample air through the inlet. Both flows are pumped by a single Triscroll 600 pump (Varian, Inc.). Gas sample moves from the inlet through

30 m of 3/8 in. i.d. (1/2 in. o.d.) FEP and tubing diameter reduces to 1/8 in. i.d. (1/4 in. o.d.) with a Swagelok reducing union. Finally, the CIMS subsamples at 4.5 L min^{-1}. A PFA three-way tee positioned between the sample bypass line and IMR enables calibration gas addition (described below). The remaining sample bypass air flow recombines with the particle bypass flow, modulated by an inlet flow and pressure control box. Particle bypass and sample bypass flows are each measured by analog mass flow meters (MKS Instruments, model 179) prior to recombination. After recombining the particle bypass and sample bypass lines in the inlet box, a Baratron pressure transducer (MKS Instruments, model 750) monitors pressure, which we maintain at 350 mbar with a fast-acting, bidirectional needle valve (Aalborg Instrument and Controls, Inc., model SMV20-SVD2-A) and a PID loop automated with LabVIEW (National Instruments Corporation).

The inlet system described above is designed to minimize differences in sampling residence times for different measured species (e.g., reduced inlet and sampling line pressure). We find little influence of the long tubing length for the inlet from the tower on instrument time response owing to turbulent flow in the inlet line (e.g., Reynold's numbers of >4000 for this sampling system). The residence time in the inlet tubing between the inlet tip at the top of the tower and the CIMS inside the trailer is 3 s. This is a similar to the lag-covariance time of 4 s determined for the segment of tubing between the sonic anemometer and the CIMS detector (Figure A1.2). Emission peaks for all acids occur at or very close to zero lag-time lending confidence to the use of one lag time for multiple organic acid fluxes. Additionally, signal peaks at zero lag time clearly emerge from background noise evident at positive and negative lag times. We evaluated the response time of the system at MEFO by overflowing the inlet at the top of the tower with UZA and waiting for the detector signal to fall to zero. The resultant signal-decays

from ambient concentrations are fit well by a single exponential decay function, with e-folding times ranging from 0.59–4.6 s for calibrated organic acids. Formic acid e-folding times are similar regardless of UZA overflow location (2.9 s at inlet on top of tower versus 2.7 s at CIMS inlet in ground trailer), suggesting that most wall interactions happen in the ion-molecule reaction chamber of the CIMS (Figure A1.3). Previous measurements of other VOCs and OVOCs typically ignore potential dampening effects in high frequency signal fluctuations due to wall interactions. Such interactions are known to occur and cause delays in response time in even short segments of Teflon tubing on the order of seconds and up to several minutes for low volatility compounds.[56] Further, spectral analysis suggests little dampening in the sampling lines (Sect. 2.4). Thus, we ignore attenuation due to wall interactions for the volatile organic acids described herein.

The CIMS was calibrated on-line once every 1–2 hours using an automated calibration source. Calibrations included standard additions of formic, propionic, methacrylic, and butyric acids during all seasons; external standards of formic acid during winter and spring; and standard additions of valeric and heptanoic acids during summer and fall. System blanks were performed during every calibration period. Section A1.1 provides details of the calibration timeline and sample data.

We process CIMS data according to standard practices using ToFware version 2.5.7. Prior to high resolution peak fitting, CIMS signals (mV ns s^{-1}) are baseline corrected and converted to counts s^{-1} by normalizing with a single-ion signal. We mass calibrate CIMS data using ≥10 fully resolved ions known to be in the spectrum m/z 32–283 (CHO_2^-, $C_2H_3O_2^-$, NO_2^-, NO_3^-, I^-, Cl^-, O_2^-, $C_{12}H_{23}O_2^-$, $C_{13}H_{25}O_2^-$, $C_{14}H_{27}O_2^-$, $C_{15}H_{29}O_2^-$, $C_{16}H_{31}O_2^-$, $C_{18}H_{35}O_2^-$, CF_3^-, $C_2F_3O_2^-$, and $C_{12}H_3Cl_4O^-$). We identify and fit peaks based on exact peak masses and established

rules of covalent bonding. The resulting peak areas are normalized by total acetate ion signal area and multiplied by the total ion signal area measured during system blanks. We calculate mixing ratios of the six organic acids for which we have permeation standards by subtracting backgrounds (system blank) and dividing by immediately preceding bi-hourly sensitivities. Calibration periods take approximately 15 minutes. In preparation for eddy covariance analysis, we truncate each time series into one, 30-minute continuous flux period and re-align the mixing ratio time series forward by 4 s to account for offsets in time between acquisition of CIMS and wind speed data (Figure A1.2). We thus report one 30-minute average value of flux per species per hour.

The CIMS was coupled to a branch enclosure during summer and soil chambers during fall to constrain direct emissions of organic acids from ponderosa pine and soils, respectively. Appendix section A1.2.1 contains details of these measurements systems.

2.3.2 Sonic anemometer

A Windmaster Pro sonic anemometer (Gill Instruments Limited, Lymington, U.K.) mounted 30 m a.g.l. measures three-dimensional wind speed vectors and temperature. Data are transmitted via RS-422 and logged at 5 Hz time resolution with ToFDAQ data acquisition software (Tofwerk AG). The anemometer model requires a firmware correction affecting vertical wind speeds (w). Positive w values +16.6% and negative w values +28.9% are corrected according to the manufacturer's specifications.[57] We flag spikes in anemometer data with a median absolute deviation filter following the methods described in Mauder et al.[58] Flagged values are replaced by linear interpolation unless >10 consecutive flags are found, in which case the entire flux period is removed from subsequent analysis. We flagged less than 0.5% of points from each wind vector or temperature time series. We rotate wind vectors to a natural coordinate

system by double rotation before trimming the time series to match the CIMS data flux periods in preparation for eddy covariance calculations.[59]

2.4 Eddy Covariance Calculations

We calculate the vertical flux of each of the six organic acids by the eddy covariance method. Eddy covariance fluxes are quasi-continuous and represent a spatially integrated footprint.[60] We calculate the flux between the surface and point of measurement for each flux period from the appropriately lagged 5 Hz mixing ratio (or temperature for sensible heat flux) and vertical wind speed data by Eq. (1):

$$F = \overline{w'C'} \quad (1)$$

where F is the vertical flux (ppt_v m s^{-1}, which can be converted to nmol m^{-2} h^{-1}, or °C m s^{-1}, which can be converted to W m^{-2}), C is the mixing ratio (ppt_v) (or temperature (°C)), w is vertical wind speed (m s^{-1}), and ′ refers to instantaneous deviations from the 30-minute mean. We note that at MEFO during SPiFFY 1 ppt_v m s^{-1} is on average equivalent to 107.5 nmol m^{-2} h^{-1}. All fluxes are reported as nmol m^{-2} h^{-1}. The sign convention is such that a positive flux value represents an upward flux from the surface to the atmosphere. A negative flux value represents a downward flux from the atmosphere towards the surface. We do not correct the calculated CIMS fluxes with temperature heat spectra due to the lack of substantial, high-frequency spectral attenuation (<1% of total flux) in organic acid co-spectral analyses. Since the sample line pressure is controlled for constant pressure, we do not apply the Webb-Pearman-Leuning correction.[61] Relative humidity corrections are applied to neither flux, nor concentrations as the instrument sensitivity for acetate CIMS has a negligible dependence on water vapor at the relative humidity ranges observed at MEFO.[53] Horizontal sensor separation between the sonic

anemometer and inlet is also negligible. We investigate each flux period to ensure that data meet three key assumptions. Any flux period that fails a test is removed from subsequent analysis.

(1) Turbulence at the measurement height must be well-developed. Friction velocity (u*) is a measure of horizontal wind shear forces, which is closely linked to atmospheric stability. Here, turbulence is considered to be well-developed when $u^* > 0.14$ m s^{-1}. We apply u*-filtering to exclude flux periods for which advection may yield spurious fluxes. Several studies have tabulated u* thresholds for various types of environments, finding that minimum u* thresholds for forested sites vary between 0.1 – 0.15 m s^{-1}.[62–64]. Values of 84%, 78%, 79%, and 77% of the data pass the turbulence test in winter, spring, summer, and fall, respectively.

(2) Fluxes must remain in steady state within the 30-minute flux period. A stationarity test determines the mean of six consecutive 5-minute segments relative to the full 30-minute flux period; flux periods are considered to pass when the deviation is <30%.[65] Values of 39–66%, 38–51%, 89–93%, and 43–65% of the data meet the stationarity criterion in winter, spring, summer, and fall, respectively.

(3) During the fall, the United States Forest Service conducted several prescribed burns to thin vegetative detritus from forest floors. The burns include a large, adjacent parcel of forest to MEFO. To exclude biomass burning contributions from organic acid measurements in the fall, flux periods with observable CO spikes in the time series are excluded. Values of 98% and 100% of data pass CO filtering in fall and other seasons, respectively.

Overall, 36–62%, 35–46%, 4–48%, and 36–58% of flux periods during winter, spring, summer, and fall, respectively, meet quality control criteria described above (ranges represent

the different organic acid analytes: formic acid most frequently passed the filters, heptanoic acid least frequently). 82% of the daytime data and 49% of the nighttime flux periods meet the quality control criteria described above for formic acid. Heptanoic acid fails to meet quality control criteria during all summer flux periods.

Fluxes represent the pine forest fetch. We calculate footprints for each season using a canopy height of 16 m and displacement height of 10.7 m.[66] Under stable conditions (Monin-Obukhov length (L) > 0), 90% flux contours are long, >2000 m north-south, and narrow, >1000 m east-west. Unstable footprints (L < 0) are more evenly distributed, extending >400 m in all directions (Figure A1.4). While many footprints include Colorado Highway 67, 1 km east of MEFO, we find no statistical difference in the distribution of organic acid fluxes when flux periods including the highway are excluded. We exclude no flux periods on the basis of footprints.

During flux periods with low turbulence, trace gases can be stored in canopy air, particularly in canopies with dense foliage, which inhibit eddy penetration. Without vertical gradient measurements of organic acids, we do not estimate the storage term during any season at SPiFFY. However, a previous organic acid eddy flux study over a boreal forest (Leaf Area Index (LAI) = 6.3) determined the storage term for formic and acetic acids to be negligible. The canopy at MEFO is less dense (LAI = 1.14) allowing more penetration of eddies carrying organic acids.[39] More importantly, organic acid flux data is filtered to exclude flux periods with low turbulence, in which canopy storage of trace gases is more pronounced. We thus ignore the storage term for organic acid fluxes in this work.

We use spectral analysis to investigate the quality of CIMS flux measurements. Co-spectral densities of vertical wind speed and mixing ratio represent the organic acid flux as a

function of frequency, a proxy for eddy size. Average cospectral densities (Figure A1.5) are calculated for all organic acids during each season between 9:00 and 15:00 local time. Here, "local time" refers to Mountain Daylight time (UTC –6) during spring, summer, and fall campaigns, and Mountain Standard time (UTC –7) during the winter campaign. Cospectra of temperature flux (sonic temperature and vertical wind speed) are similar to organic acid cospectra, demonstrating that high frequency variations are not significantly attenuated by the inlet at frequencies <2.5 Hz. Averaging times are long enough, time resolutions fast enough, and organic acids detection sufficiently sensitive to observe an inertial subrange in the spectra for all acids. We hypothesize that reducing and controlling inlet pressure in the closed-path system obviates the need for spectral transformation. We note that substantial spectral attenuation may occur at frequencies >2.5 Hz; however, frequencies beyond the Nyquist frequency (2.5 Hz here) are obfuscated by aliasing.

Time-lagged covariance functions between vertical wind speeds and mixing ratios of organic acids provide a useful calculation of uncertainty in eddy covariance fluxes. The covariance at lag times far exceeding the flux integral timescale represent the combined random instrument noise and environmental fluctuations that contribute to measured fluxes.[67,68] We calculate the flux detection limit for an individual organic acid for a single flux period as 3σ of covariances lagged 30–60 s, in both positive and negative directions. Observed fluxes of formic acid consistently exceed the detection limit for two-thirds of the flux periods, while observed methacrylic acid fluxes were often below detection limit (Table 2.3). More daytime fluxes exceeded detection limit than nighttime fluxes.

2.5 Results

MEFO experienced clean continental air with occasional intrusions of polluted, urban air from Denver or Colorado Springs. SO_2 concentrations are generally below 1 ppb_v but spike above 1.5 ppb_v during some evenings when winds are northeasterly or southeasterly (i.e. from Front Range cities). NO_x concentrations trend similarly with wind direction at MEFO and are consistent with past measurements. Ozone rarely exceeds 60 ppb_v even during peak photochemistry in the summer. The ozone maximum was 97 ppb_v on 28 July. Seasonal measurements of trace gases, including organic acids, are summarized in Table 2.2.

MEFO is similar to other coniferous forest sites in terms of formic acid concentrations. Daytime formic acid at MEFO peaked at 2 - 6 ppb_v in the summer, comparable to peak observations (2 - 3 ppb) over a boreal forest in Finland during summer 2015.[6]
Formic acid mixing ratios are 10 – 100x higher than other organic acids. Mixing ratios for all organic acids are an order of magnitude higher in warmer seasons (summer and fall) than in colder seasons (winter and spring). All six organic acids follow the same diel trends within a given season. In the summer, organic acids increase at sunrise, reach a late afternoon or evening maximum, and then decrease overnight in all seasons (Figure 2.2). A mid-morning (~9:00 local time) reduction in all organic acid mixing ratios occurs most days and is consistent with the breakup of the nocturnal boundary layer. Formic, propionic, butyric, and valeric acids follow the same diel trends as previous measurements in the Colorado Front Range, although summer formic acid at the Boulder Atmospheric Observatory is about a factor of 2 higher than at MEFO.[44]

Organic acid fluxes are consistently upward throughout all four seasons. We note that though this paper focuses on small organic acids, other compounds, such as isocyanic acid, exhibit downward fluxes, which will be the focus of future publications. This indicates persistent

ecosystem sources of all six organic acids (Figure 2.2). Diel cycles in flux differ from concentration. Fluxes increase from near-zero at sunrise and peak at mid-day, before decreasing back to zero (within measurement uncertainty) near sunset. Downward organic acid fluxes are rare, accounting for only 6 – 15% of all unfiltered fluxes and 1 – 8% of all quality-filtered fluxes exceeding the flux detection limit. Most (> 99%) downward flux events occurred at nighttime. Organic acid fluxes are approximately an order of magnitude lower in winter and spring than in summer and fall.

We calculate exchange velocity (V_{ex}, cm s^{-1}) as the flux divided by the average concentration of the flux period for each acid. Positive exchange velocities represent emission rates from the forest, while negative exchange velocities represent deposition rates. V_{ex} provides a flux normalized by concentration, thus enabling comparison of biosphere-atmosphere exchange rates across different sites subject to different concentration regimes. V_{ex} is equivalent in magnitude to deposition velocity (V_{dep}), but opposite in sign convention ($V_{ex} = -V_{dep}$). V_{ex} is commonly used to denote the average vertical rate of exchange between the measurement height and the surface, particularly for eddy flux measurements of oxygenated volatile organic compounds.[6,13,37,40,69–71] Despite formic acid having orders of magnitude higher concentration than the other organic acids, the exchange velocities are all of the same order of magnitude in the spring and summer. In contrast, during the colder spring and winter months, formic acid emission rates are again much higher than the other acids, indicating that the fluxes may be driven by different processes for the different organic acids.

2.6 Discussion

The observed organic acid mixing ratio and flux diel cycles require a daytime source coupled to a rapid (i.e. lifetime of hours) sink. Summer observations are similar to previous

studies: mixing ratios peak in the mid-day, similar to summertime measurements in forests[2,40,72] and urban sites.[49] The upward formic acid flux maximizes in the middle of the day, similar to formic acid flux observations at Hyytiälä.[6]

Large canopy-level emissions at MEFO indicate that formic acid is potentially an important source of reactive atmospheric carbon. In summer 2010, Kaser et al. measured 0.50 mg m^{-2} h^{-1} (37 μmolC m^{-2} h^{-1}) mid-day average monoterpene emission fluxes - only 10 times larger than summer 2016 mid-day median formic acid fluxes of 3.8 μmolC m^{-2} h^{-1}.[39]

Despite measuring a sizeable range of organic acid concentrations across the seasons, we observe no evidence of a compensation point (i.e. no consistent shift from emission to deposition as ambient concentrations increase), contrary to observations over a tropical forest by Jardine et al. (Figure A1.7).[37]

The upward organic acid fluxes persist through the seasons. Compiling the data demonstrates that organic acid fluxes increase exponentially with temperature (Figure 2.3) and vapor pressure deficit (Figure A1.8), decrease exponentially with relative humidity, but do not correlate with photoactive photon flux density (PPFD) ($r^2 < 0.10$ for formic acid) or O_3 ($r^2 < 0.15$). These correlations initially appear consistent with a direct plant source of the organic acids to the atmosphere, but closer inspection reveals evidence for other sources.

The strong temperature dependence of the observed organic acid fluxes follows the exponential temperature equation used by ecosystem emissions models for light independent plant VOC emissions. For example, the Model of Emissions of Gases and Aerosols from Nature (MEGAN)[73] models monoterpene fluxes as:

$$E = E_f e^{\beta(T-T_s)} \quad (2)$$

where E_f is the basal emission rate (nmol m^{-2} h^{-1}) at a standard temperature (T_s, 303 K), T is the ambient temperature in Kelvin, and β represents a temperature scaling factor, assigned a value of 0.09 K^{-1} for monoterpenes, which sets the emission to E_f at T_s. We fit the canopy-level flux data from all seasons to Eq. (2) to derive E_f and calculate basal emission rates of 4700±210 nmol m^{-2} h^{-1} for formic, 59±3.2 nmol m^{-2} h^{-1} for propanoic, 12±0.9 nmol m^{-2} h^{-1} for methacrylic, 66±3.2 nmol m^{-2} h^{-1} for butyric, 20±2.2 nmol m^{-2} h^{-1} for valeric, and 17±3.2 nmol m^{-2} h^{-1} for heptanoic acids**.** The model accounts for only 15 - 53% of the variance of the organic acid fluxes.

Nighttime fluxes are particularly problematic as nocturnal temperatures are high enough to result in a much larger predicted nighttime emission than the near-zero flux we observed. Of course, this analysis ignores contributions of dry deposition to the observed flux, which could improve model-measurement agreement. Incorporating light into the model, as with the Parameterized Canopy Environment Emission Activity (PCEEA) model, provides a better representation of the diel cycle than the temperature-only MEGAN model but underestimates daytime upward fluxes and fails to improve the correlation coefficients (r^2 = 0.15-0.53 for temperature only; 0.24-0.50 for temperature and light).[74] The weak correlation coefficients suggest that while application of a primary ecosystem source may improve the model-measurement discrepancies for formic acid over forests described above, a direct source may be mechanistically inaccurate. Further, formic acid basal emissions of 4700 nmol m^{-2} h^{-1} are 7x larger than the 30 μg m^{-2} h^{-1} basal emissions used in previous studies to estimate formic acid emissions from trees and shrubs in forest ecosystems.[6,12] Thus direct plant emissions are unlikely the sole source of the organic acids.

We observe few downward fluxes, meaning that local dry deposition is insufficient to overwhelm the sources and control the atmospheric lifetimes of any of the organic acids.

The observed, net ecosystem organic acid flux is temperature-dependent, occurs only during the daytime, and persists throughout the seasons. Here, we evaluate four possible contributing sources of organic acids: primary emissions from (1) plants, (2) soils, and (3) ants, plus (4) secondary, in-canopy chemistry of other biogenic VOC emissions. We compare these sources to predicted dry deposition sinks and consider the organic acid flux budget at MEFO.

2.6.1 Plant Emissions

Plants emit C1 – C7 alkanoic acids and are a plausible primary source of observed upward flux. Plants produce formic acid by oxidizing glyoxylic acid, methanol, and formaldehyde and by reducing CO_2 to formate.[75,76] Biochemical production mechanisms of the other organic C_2-C_7 acids discussed herein are scarce. To the best of our knowledge, direct emissions of propionic, methacrylic, butyric, valeric, and heptanoic acids from plants may be presented here for the first time. This could also be evidence of very rapid secondary chemical formation of organic acids from biogenic precursors.

Correlations of temperature and vapor pressure deficit with organic acid fluxes are consistent with direct plant emissions as are the observed seasonal trends in organic acid fluxes. Plant metabolism, including the formic acid-forming processes of ethylene synthesis and methanol oxidation, slows during colder seasons due to reduced temperatures and available sunlight. Likewise, organic acid emissions decrease by an order of magnitude between warm (summer and fall) and cold (winter and spring) seasons.

However, measurements of organic acid emissions from plants suggest relatively small fluxes - at least an order of magnitude smaller than known oxidative precursors such as isoprene and monoterpenes.[34] MEGAN incorporates leaf cuvette and branch enclosure measurements into emission factors used to predict plant emissions for formic, acetic, and pyruvic acids.[73] Applying

the MEGAN temperature parameterization to MEFO predicts a summer mid-day leaf-level formic acid flux of 170 nmol m^{-2} h^{-1}, in comparison to the observed 3400 nmol m^{-2} h^{-1}.

We can further refine these estimates of primary biogenic emission using previous studies of pine tree emissions of formic acid. To the best of our knowledge, there are no previous measurements of C3-C7 organic acid emissions from plants, let alone pine trees. Villanueva-Fierro et al. measured a mass emission rate of 210 ng_{HCOOH} $g_{d.w.}^{-1}$ h^{-1} from ponderosa pine in Central New Mexico.[77] Kesselmeier et al. measured an average mass emission rate of 333 ng_{HCOOH} $g_{d.w.}^{-1}$ h^{-1} from Italian stone pine (*Pinus pinea* L).[78] Dense pine forests with LAIs on the order of 2.5 – 4.0 have pine needle biomass densities of 400 – 900 $g_{d.w.}$ m^{-2}, and we estimate 200 $g_{d.w.}$ m^{-2} pine needle density at MEFO (LAI = 1.14).[79] We estimate formic acid basal emission rates from ponderosa pine trees (E_f), mass emission rate (E_{needle}, ng $g_{d.w.}^{-1}$ h^{-1}) and the density of pine needles in a characteristic area of forest (ρ_{needle}, $g_{d.w.}$ m^{-2}) from

$$E_f = E_{needle}\rho_{needle} \quad (3)$$

Using the two published pine mass emission rates, we calculate a basal emission rate for formic acid of 910 – 1500 nmol m^{-2} h^{-1}, smaller than the 4700 nmol m^{-2} h^{-1} calculated from the ecosystem scale fluxes (Figure 2.3). Scaling these emission potentials to MEFO according to Eq. (2) using $\alpha = 0.09$ and $T_s = 303$ K, we predict that direct plant emissions from ponderosa pine would account for mid-day fluxes of 630 – 1000 nmol m^{-2} h^{-1} of formic acid in summer and 140 – 220 nmol m^{-2} h^{-1} in winter. For comparison, Schobesberger et al. estimated a summer afternoon primary plant emission of formic acid at Hyytiala as ~5 ppt_v m s^{-1} (~500 nmol m^{-2} h^{-1}).[6] Besides predicted emissions for Italian stone pine, these literature-based estimates suggest that plant emissions account for little of the observed upward flux.

We compare these literature-based estimates of plant emissions to actual branch enclosure measurements. We enclosed a ponderosa pine branch ~5 m a.g.l. in a Teflon bag and sampled the concentration gradient between ambient air outside versus inside the bag with the CIMS (see Sect. A1.2.1 for details). We observed very small primary plant emissions of organic acids with these *in situ* branch enclosures (Table 2.4). Scaling our observed leaf-level emission of formic acid to the forest leaf area, results in a direct plant flux of formic acid of 94 nmol m^{-2} h^{-1}, just 2.5% of the summer daily maximum.

Our branch enclosure measurements suggest that while primary plant emissions are negligible for formic acid, they may be relatively important sources of the other organic acids during cold seasons. For example, during winter, plant emissions of butyric acid account for a large fraction (62%) of the measured flux + dry deposition. During spring, plant emissions overestimate (190%) the butyric acid flux budget.

2.6.2 Soil and Leaf Litter Emissions

Soils and leaf litter can be direct sources of multiple organic acids via microbial activity.[80,81] Microbes of the *Propionibacterium* genus synthesize propanoic acid from succinate or pyruvate intermediaries following glycolysis. Similarly, butyric acid is synthesized by glycolytically-formed pyruvate oxidizing to Acetyl CoA; butyric acid can be further processed by fermentation. Mixed acid synthesis can produce formic, acetic, lactic, butyric, and succinic acids through alternate end-pathways to fermentation for many microbes. Ubiquitous methanotrophic bacteria synthesize formic acid from subsequent steps following the oxidation of methane prior to initiation of the serine cycle.

Sanhueza and Andreae measured daily average formic acid emissions of 0.14 nmol m^{-2} s^{-1} from dry, savannah soils in Venezuela.[82] Based on these measurements, Paulot et al. developed an exponential relationship between soil emissions of HCOOH (E_{soil}) and temperature:[12]

$$E_{soil} = Ae^{((\beta \times T)-1)} \quad (4)$$

where A is the basal emission rate from soil (nmol m^{-2} h^{-1}), β is the temperature sensitivity, and T is soil temperature (°C). Paulot et al. found A = 1.7 x 10^{-3} nmol m^{-2} s^{-1} and β = 0.119 °C^{-1}.[12] The dry, deep, sandy loamy soils at MEFO have similar attributes to the savannah soils with neutral pH (6.1 – 7.8) and minimal organic content (1 – 4 %).[50] Mielnik et al. measured soil formic acid fluxes of a similar magnitude (0.01 – 0.15 nmol m^{-2} s^{-1}) from Colorado soils, including samples from MEFO collected in spring and summer 2018.[21] The Colorado soils showed larger basal emission rates but suppressed temperature dependences (A = 0.11 nmol m^{-2} s^{-1} and β = 0.028 °C^{-1}) relative to the tropical savannah soils. Based on these studies, we calculate that soil emits 49 – 300 nmol m^{-2} h^{-1} of formic acid during summer (1.3 – 8% of observed ecosystem flux) and 6.2 – 180 nmol m^{-2} h^{-1} during winter (2.9 - 84% of observed ecosystem flux). However, soil emissions depend on soil moisture, and these calculations do not consider that or potential emissions from leaf litter – nor do they provide soil emissions for organic acids other than formic or acetic acid.

We conducted *in situ* soil chamber experiments during fall 2016 to observationally constrain soil / forest floor emissions of formic and other organic acids. Gray et al. describe the soil chambers in detail.[83] We installed three chambers within the flux footprint into soil that was covered in needle detritus. Organic acid emissions from the chambers are consistently small, accounting for <1% of the observed fall fluxes (Table 2.4). Soils emit more formic acid than the other organic acids, consistent with a methanotrophic bacteria source. The observed formic acid emission is an order of magnitude smaller than the previous two studies, which we speculate is

due to (i) the cooler ambient temperatures than those explored in laboratory experiments, (ii) potential organic acid uptake by the needle litter layer, and (iii) the very dry conditions during the soil chamber studies. MEFO experienced no precipitation for ~4 weeks during the fall before soil chamber measurements were conducted, and the soil was likely much drier than previous lab or field experiments. Considering both the literature and *in situ* chamber constraints, soils are a small atmospheric source for any of the organic acids.

The persistent upward fluxes observed during winter and spring raise the question of snow as an organic acid source. A thick (>30 cm) layer of snow covered the forest floor at MEFO four times during SPiFFY – twice during winter and twice during spring. Surprisingly, these events impacted neither the diel cycle, nor the magnitude of organic acid fluxes (Figure 2.4).

2.6.3 Ant Emissions

Formicine ants emit formic acid for defense and alarm signaling.[23] *Formica podzolica* is an abundant ant species at a nearby site in the forest (39.1° N, 105.0833° W).[84] We estimate ant emissions at Manitou by Eq. (5) following Graedel and Eisner:[23]

$$F_{ants} = \frac{\rho_a m_a \psi}{\delta} \quad (5)$$

where F_{ants} is formic acid flux from *Formica* sp. ants, ρ_a is the estimated density of ants (100 – 600 ants m^{-2}), m_a is average ant mass (5 mg), φ is fraction of ant body mass present as volatilizable formic acid (0.02), and δ is the timescale for formic acid release (0.5 yr). Ant density is based upon two studies of *Formica* ant ecology in Colorado, which found colony densities between 15 – 115 mounds ha^{-1}.[85,86] Assuming 5 x 10^5 ants $mound^{-1}$, we estimate ant densities between 100 – 600 ants m^{-2}. We calculate that ants contribute 54 – 300 nmol m^{-2} h^{-1} of the formic acid flux in the summer, or 1 – 8 % of the measured daily maximum formic acid flux.

Ants hibernate in the colder seasons, and we assume they are negligible formic acid sources in winter and spring at Manitou. Ants and other fauna are not known sources of the other five organic acids.

2.6.4 In-canopy Chemistry

Multi-generational oxidation of volatile organic compounds produces much of the knownformic acid budget.[12,14,15] For example, monoterpenes with terminal alkenes, such as beta pinene and limonene, can be oxidized by O_3 to form stabilized Criegee intermediates (CH_2OO). The Criegee biradical can then react with readily available water vapor ($k = 1 \times 10^{-17}$ cm^3 $molec^{-1}$ s^{-1}) and generate formic acid. In fact, H_2O + different Criegee intermediates and HO_2 or RO_2 + a peroxyacyl radical constitute the primary formation reactions for alkanoic acids employed by the Master Chemical Mechanism via the website: http://mcm.leeds.ac.uk/MCM.[87,88]

Organic acid formation throughout a well-mixed boundary layer should not affect observed ecosystem-atmosphere fluxes unless there is a strong vertical gradient in production. However, in-canopy chemistry is a known phenomenon in which fast chemical reactions on the timescale of forest canopy residence times (<10 min) create vertical gradients in concentration below the sensor height and thus an observed turbulent flux. In-canopy chemistry is thought to cause enhanced deposition fluxes of O_3 and enhanced upward fluxes of NO_x, NO_y, and secondary organic aerosol.[89–92] Production reactions must be faster than the canopy air exchange rate below the sensor height to cause observed upward fluxes, requiring substantial emissions of very reactive precursors. However, ponderosa pine trees are strong emitters of monoterpenes and other VOCs.[39,93] Alwe et al. speculate that in-canopy chemistry is responsible for upward formic acid fluxes, providing correlations between formic acid and oxidized organic compounds as

supporting evidence.[13] In-canopy ozonolysis and OH oxidation of biogenic VOC emissions are thus potential ecosystem sources of organic acids.

Several lines of evidence point to the possible role of in-canopy chemistry in the observed MEFO ecosystem source of organic acids. The temperature-dependence of observed organic acid emissions is similar to that of biogenic VOC precursors, and monoterpenes in particular. Kaser et al. (2013) found temperature-dependent fit parameters for Eq. (2) of $E_f = 0.50$ mg m^{-2} h^{-1} and $\beta = 0.12$.[39] Using these parameters and ambient temperatures measured during SPiFFY, we estimate monoterpene emissions of 0 – 0.49 mg m^{-2} h^{-1}, which accounts for 0 - 36 μmolC m^{-2} h^{-1} of organic carbon atoms, compared to the 0 – 3.8 μmolC m^{-2} h^{-1} observed emission for formic acid. There is little correlation between formic acid flux and either O_3 or PPFD, which would influence available O_3 or OH, but the oxidant might not be the limiting reactant in the organic acid production. Thus a clear correlation is not necessarily expected.

For in-canopy chemistry to produce an observed upward organic acid flux, several requirements must be met. First, in-canopy production must outcompete in-canopy deposition. Second, the forest must have enough oxidant in the canopy and emit enough fast-reacting VOCs so as to outcompete production of organic acids above the sensor height on the timescale of canopy-atmosphere exchange – thereby producing a vertical gradient in organic acids. Ponderosa pines at Manitou emit 2-methyl-3-buten-2-ol (MBO) (50.2 % of total BVOC emissions) and monoterpenes (33.5 %), which account for ~62 % of the OH reactivity at the site.[94] NO^+ CIMS measured isoprene concentrations of ~ 200 ppt_v at MEFO.[95]

Multi-generational reactions of O_3 and OH with terpenes produce formic acid. Formic acid yields from MBO are 6 – 8% with OH and 3% with O_3.[96] Formic acid yields from

monoterpenes are 4 - 11% with OH and 7% with O_3.[97,98] We calculate the chemical production by:

$$Flux_{HCOOH} = Flux_{precursor} \times k_{oxidant} \times C_{oxidant} \times \tau \times Y \quad (6)$$

where $Flux_{HCOOH}$ is the predicted chemical production flux of formic acid, $Flux_{precursor}$ is the average daily maximum flux of MBO from Kaser et al. or the average daily maximum flux of monoterpenes calculated from the E_f and β parameters of Kaser et al. given observed meteorological conditions and Eq. (2),[39] $k_{oxidant}$ is the rate constant of the corresponding precursor with OH or O_3, $C_{oxidant}$ is the concentration of OH or O_3, τ is the canopy residence time, and Y is the appropriate molar yield. The canopy residence time is estimated from the findings of Martens et al., who report residence times for radon, a transport tracer for CO_2 exchange between the atmosphere and a forest canopy.[99] Given summertime daily maximum fluxes of 0.31 mg m^{-2} h^{-1} for monoterpenes and 2.2 mg m^{-2} h^{-1} for MBO, an estimated canopy OH concentration of $1x10^6$ molec cm^{-3}, a canopy residence time of 10 minutes, and rate constants (k_{OH}) of $1x10^{-10}$ and $3.9x10^{-11}$ cm^3 $molec^{-1}$ s^{-1} for monoterpenes and MBO, respectively, we predict 45 and 42 nmol m^{-2} h^{-1} formic acid from in-canopy OH oxidation of monoterpenes and MBO, respectively. In-canopy OH oxidation calculated according to Eq. (6) accounts for at most 1% (monoterpenes) and 1% (MBO) of the average midday measured formic acid flux of 3500 nmol m^{-2} h^{-1}. Using the same biogenic hydrocarbon emissions, a measured average daily maximum O_3 concentration of $107x10^{10}$ molec cm^{-3} (~60 ppb_v), and k_{ozone} values of $3.9x10^{-15}$ and $8.6x10^{-18}$ cm^3 $molec^{-1}$ s^{-1} for monoterpenes and MBO, respectively, we calculate formic acid fluxes of 1190 and 2.5 nmol m^{-2} h^{-1} following Eq. (6). These afternoon maximum production fluxes account for 35% and <1% of the net formic acid flux from monoterpene and MBO ozonolysis, respectively. We note that formic acid yields vary with oxidant exposure, and

in-canopy chemistry must occur within 10 minutes to contribute to an observed upward flux, so these yields used in these calculations represent upper estimates.[28]

These back-of-the-envelope calculations thus imply that in-canopy oxidation of reactive biogenic VOCs – and ozonolysis of monoterpenes in particular – may be substantial components of the observed organic acid flux. Ozone changes little across the seasons (Table 2.2), but the temperature decreases substantially in the winter and spring – meaning that the temperature-dependent monoterpene and MBO emissions will also decrease. Thus, we estimate that in-canopy chemistry will cause 120 nmol m^{-2} h^{-1} of formic acid flux in the winter, or 59% of the observed flux.

OH oxidation of monoterpenes produces 0.002-0.06% molar yields of methacrylic and butyric acids, which would result in upward fluxes of 3.0 and 2.5 nmol m^{-2} h^{-1} of methacrylic and butyric acids, respectively, in summer.[28] Here, we calculate chemical production with a weighted average assuming 33.3% of total monoterpenes each represented by alpha pinene, beta pinene, and limonene. A more detailed canopy chemistry model may be able to better constrain some of the potential sources that we identify here. For example, peroxy radicals are present at MEFO in mixing ratios as high as 180 ppt_v and can react with other RO_2 or HO_2 radicals to produce gaseous organic acids.[100]

2.6.5 Flux Budget

We combine the observational and literature-derived constraints on each of the organic acid sources and sinks to create a flux budget. We focus on mid-day fluxes, when the observed ecosystem organic acid sources are at their largest. We calculate dry deposition with a resistance model, including canopy resistance improvements from Nguyen et al.[40,101] A detailed description of the resistance model is provided in Sect. A1.3. The observed flux is the net result of sources

minus sinks, so we calculate an organic acid source term as the sum of observed flux plus calculated dry deposition.

We compare the 'bottom-up' formic acid source (i.e. sum of individually calculated components discussed above) to the 'top-down' source determined as the sum of observed flux+calculated dry deposition. We see excellent agreement for formic acid sources at night, but strong discrepancies in the day (Figure 2.5). Chemical production, specifically rapid ozonolysis of monoterpenes in the canopy, is predicted to be the single largest source of formic acid. Thus, we find a missing / underestimated formic acid source and potentially an overestimated formic acid sink. With the exception of methacrylic acid, canopy-level fluxes are far larger in warm seasons than cold seasons (Figure 2.6). During winter, summer, and fall, sizeable upward fluxes of formic acid are missing in the budgets. During spring, we overestimate sources (or underestimate sinks). This is one season with substantial snow cover, which we speculate may affect dry deposition, although this observation may also be the result of uncertainties around the relatively small observed flux. Secondary chemical production is the most important predicted source of formic acid across all seasons. In contrast, neither methacrylic nor butyric acid sources are controlled by chemical production. Most of these acids' budgets are controlled by missing sources except for during cold seasons when plant emissions become an important source for butyric acid. Like formic acid, butyric acid shows a missing sink or overestimated source during spring.

There are three ways to improve the comparison of modeled vs. observed organic acid fluxes: (1) ecosystem source component(s) may be missing or underestimated, (2) missing and/or underestimated source(s) in combination with overestimated deposition, or (3) there may be a

missing sink that is greatly enhanced above the sensor height relative to below. Missing sources could include:

- In-canopy chemistry of sesquiterpenes, which are emitted from ponderosa pines[102] and react rapidly with O_3,[103] though their organic acid yields are unknown. Ponderosa pines also emit other terpenoids, including methyl chavicol, which are also likely oxidized to form organic acids.[104] We also note that different monoterpene isomers produce different amounts and distributions of organic acids.[28]
- Reactions of O_3 with ecosystem sources (e.g. epicuticular waxes, cellulose or lignin on branch surfaces, exposed pine resins, and/or organic matter on soil surfaces); while ozonolysis of plant biomass has been noted to produce formic acid,[105] the lack of correlation between ozone and upward organic acid fluxes makes this unlikely.
- Dew or water layers on ecosystem surfaces may act as an organic acid reservoir, absorbing organic acids at night, and then evaporating and releasing them during the day. Studies of ammonia have found that surface moisture can account for a sizable fraction of morning emissions.[106] We would expect a morning increase in formic acid emissions from the forest, which is seen in the concentration and flux data (Figure 2.2).
- Direct emissions from biogenic sources not constrained with measurements in this study, such as herbaceous plants on the forest floor, tree trunks, fallen branches, and pine resins.[3,107–109]

Alternately, the top-down approach may overestimate the organic acid sinks. Removal of organic acid by OH radicals or O_3 are negligible relative to dry deposition and cannot account for the model-measurement discrepancy. However, our understanding of dry deposition of

oxygenated VOCs is limited, and a more likely source of uncertainty. While not included in our dry deposition resistance model, volatile organic acids can be lost to particles through gas-particle partitioning and reactions at particle surfaces. However, previous studies suggest that aqueous-phase partitioning does not contribute significantly to ambient organic acid mixing ratios with calculated organic acid losses to particles of 6.1×10^{-11} - 2.4×10^{-8} ppb_v.[44] MEFO in the summer and fall is typically arid, and is thus likely to have limited water surfaces, to which the water-soluble organic acids in this study could be lost. Gases may not be removed to forest surfaces with the same efficiency as wetter environments. Further investigation of dry deposition mechanisms for oxidized organic species is essential for understanding the role of the terrestrial biosphere in regulating organic acid concentrations in the atmosphere.

Organic acid loss processes that are far faster above the sensor height than below would create a decreasing vertical gradient throughout the boundary layer and an apparent upward flux. That is, the flux discrepancy could be driven by an atmospheric loss process rather than an ecosystem source. Possible organic acid loss processes above the sensor height include: entrainment of clean air from the free troposphere, removal by dissolution in cloud droplets, or more rapid photolysis or oxidation higher up in the boundary layer. One possible chemical loss for organic acids that are unexplored in the atmospheric chemistry literature is the esterification reaction of carboxylic acids with alcohols, such as methanol. An atmospheric loss process that is enhanced with altitude would also explain the diel cycles in organic acid mixing ratio: the afternoon drop-off in organic acid mixing ratio requires a rapid loss process. While dry deposition is typically invoked to explain diel cycles from ground observations of nitric acid (HNO_3), the organic acid flux measurements during SPiFFY are upward throughout the day. Thus ecosystem sources consistently outcompete dry deposition. A removal process higher in the

atmosphere would help explain both the observed upward flux and the short lifetime implied by the mixing ratio diel cycle. However, we note that Mattila et al. did not observe any evidence for strong sinks higher in the boundary layer from vertical profiles of organic acids in the Front Range of Colorado, and that those vertical profile observations were more consistent with surface-level sources such as ozonolysis of surface organic matter, such as vegetation, soils, or organic films.[21]

2.7 Conclusions

We observe a consistent ecosystem source of organic acids throughout all four seasons at this semi-arid ponderosa pine forest site. Organic acid fluxes from the forest increase exponentially with temperature similar to monoterpene fluxes. MEFO is clearly a net source of organic acids to the atmosphere throughout the year although the fluxes are largest in the warmer summer and fall months. The observed emission fluxes can be partially accounted for by known and observed primary and secondary sources; however, the relative importance of these sources varies for each organic acid. Soils and pine trees are predicted to be negligible sources of formic acid relative to in-canopy chemical production, but may be more important for other organic acids, particularly in colder seasons when emissions of reactive terpenoids and subsequent in-canopy chemistry are small. Formic acid may be a valuable tracer for the chemical flux of ozone. Assuming a daytime ozone flux of ~-40μmol m^{-2} h^{-1}, a production flux of 1190 nmol m^{-2} h^{-1} suggests that ~3% of the ozone flux signal could be attributed to formic acid production from ozonolysis reactions with monoterpenes. A missing source (or overestimated sink below the canopy height – or underestimated sink above) remains not only for formic acid, but also butyric and methacrylic acids. Potential organic acid sources include in-canopy gas or surface oxidation chemistry, or interaction with water layers on ecosystem surfaces. We may also be

overestimating dry deposition in the arid Colorado environment and/or ignoring organic acid sinks higher in the boundary layer. Our observations highlight the uncertainties in understanding the sources and sinks of even the simplest oxidized VOCs in the atmosphere and point to a need for a deeper mechanistic understanding of dry deposition of organic gases, emission of larger and multi-functional terpenoids, and rapid oxidation chemistry occurring in forest canopies. Removal processes for organic acids remain puzzling, as the diel concentration profiles suggest a strong afternoon sink, but our flux observations demonstrate that dry deposition is insufficient to outcompete the ecosystem sources.

Chapter 2 Figures

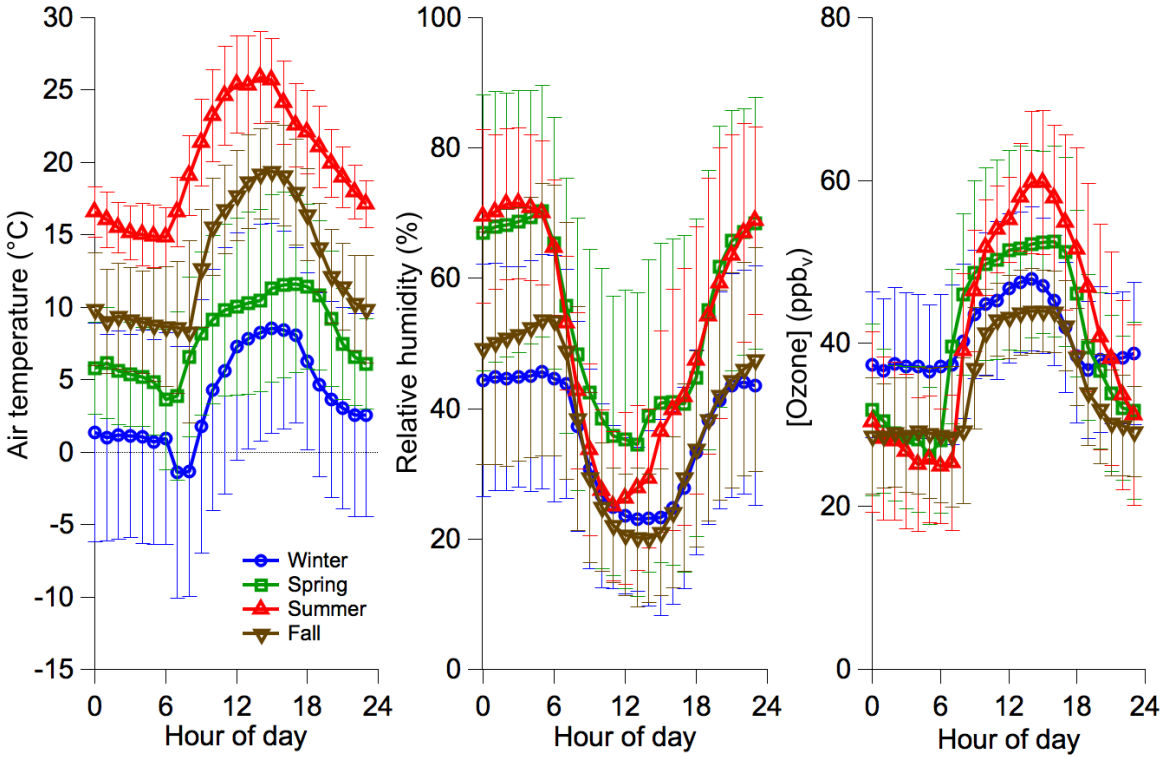

Figure 2.1. Seasonally averaged temperature (left), relative humidity (center), and ozone mixing ratios (right) during the measurement campaigns vary across the seasons. Points represent hourly averages with error bars encompassing ±1 standard deviation. Hours of day are derived from local time, which we define as Mountain Daylight time (UTC -6) for spring, summer, and fall seasons and Mountain Standard time (UTC -7) for the winter season.

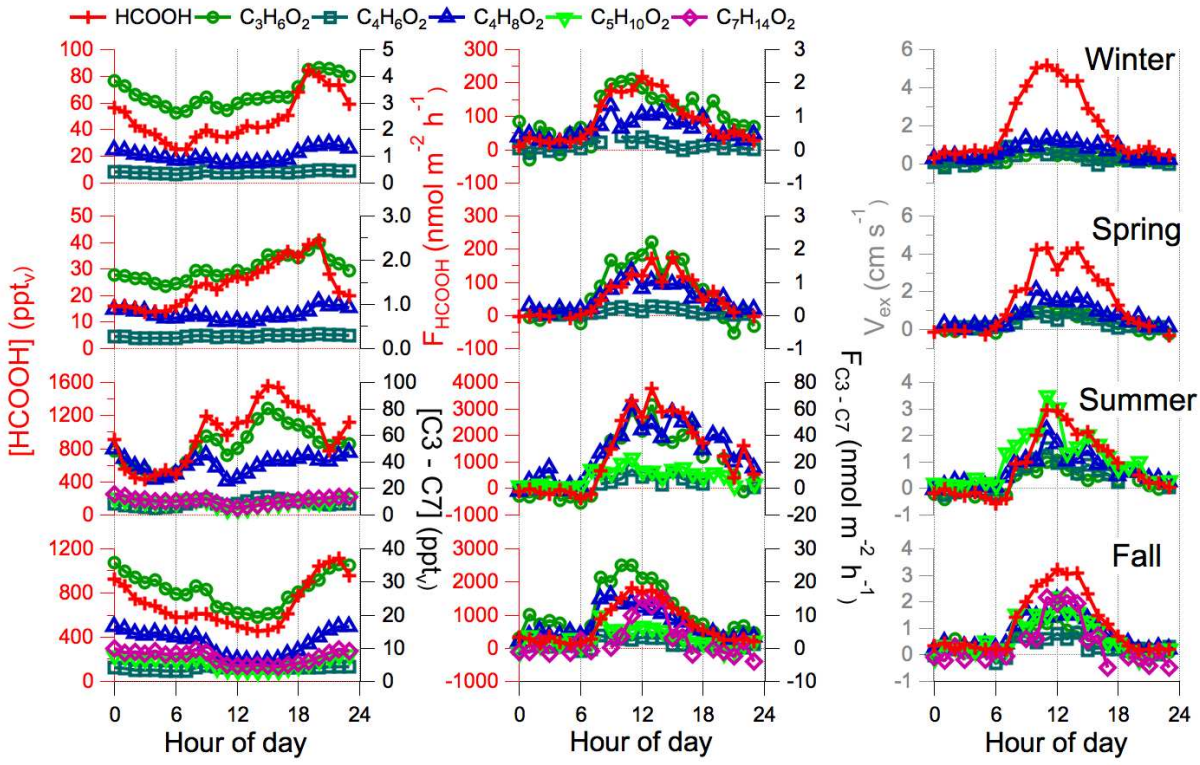

Figure 2.2. Seasonal diel mixing ratios (ppt$_v$, left), fluxes (nmol m^{-2} h^{-1}, middle), and exchange velocities (cm s^{-1}, right) for six organic acids. Data points represent seasonal, hourly medians. Fluxes and exchange velocities are filtered according to Sect. 2.4. From top to bottom, seasons are winter, spring, summer and fall. For mixing ratio and flux plots, formic acid mixing ratio is on the left axis, and propionic, methacrylic, butyric, valeric, and heptanoic acids are on the right axis. Upward fluxes and exchange velocities are evident for all organic acids during the daytime with average nighttime fluxes approaching zero. See Figures A1.9-A1.14 for additional details.

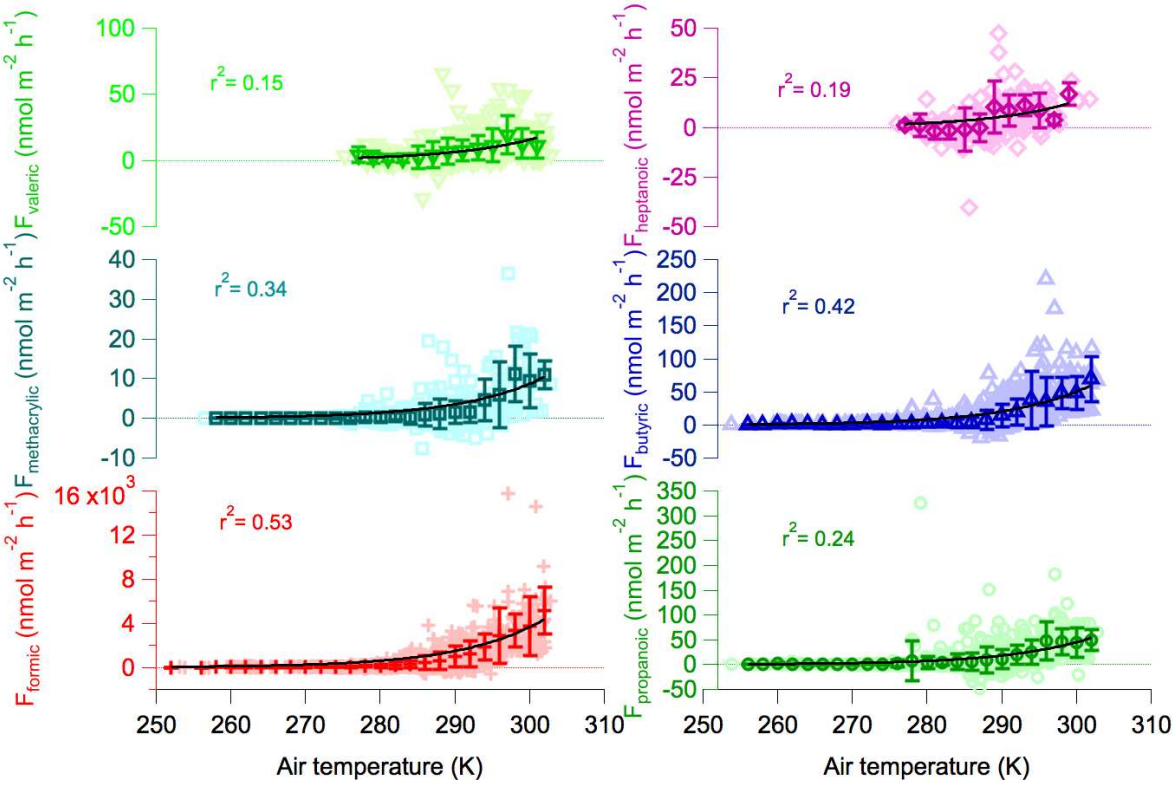

Figure 2.3. Organic acid fluxes increase with ambient air temperature at MEFO. The black lines represent an exponential fit of the form, $F_{net} = F_{std} e^{0.09(T-303)}$ (see Eq. (2)), where F_{net} is the quality-filtered canopy flux, F_{std} is standard emission at 303 K, and T is the temperature separated into 2 K bins (all seasons). Error bars represent the standard deviation of each bin. We determine correlation coefficients (r^2) for the model versus the observational data. Winter and spring data are absent for valeric and heptanoic acids due to the lack of calibrations during those seasons.

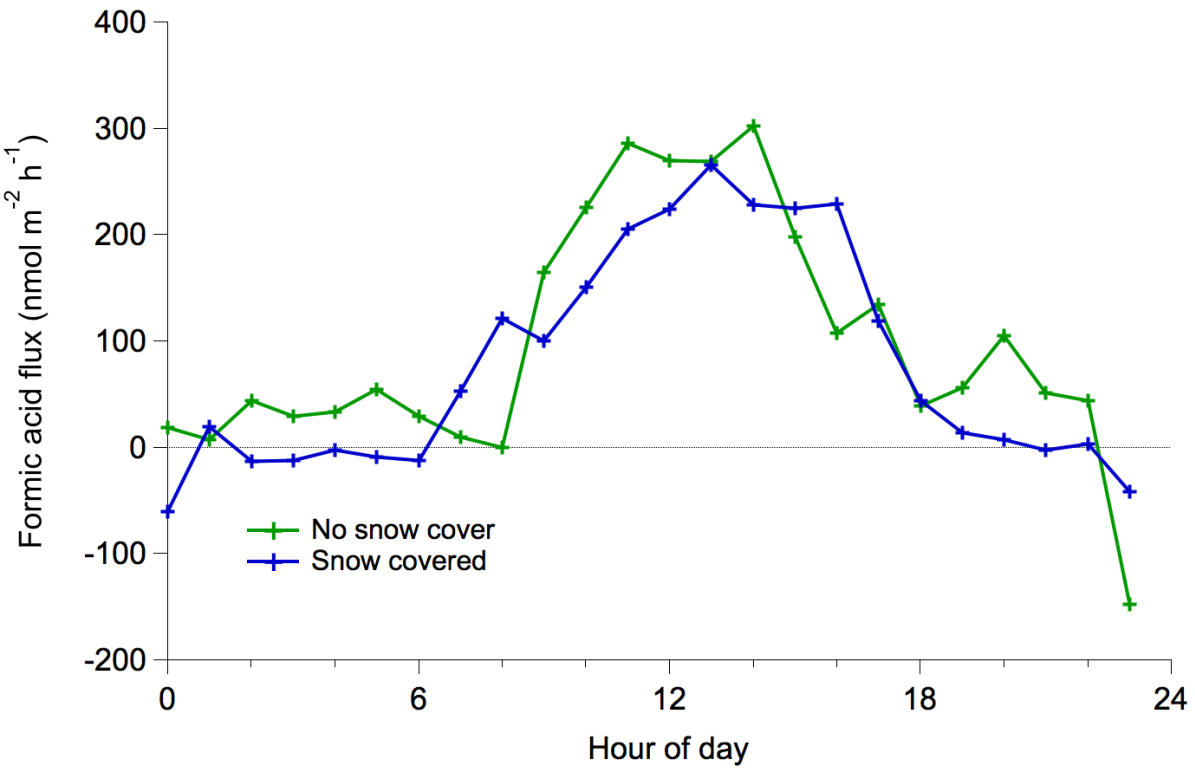

Figure 2.4. Diel averaged formic acid fluxes from 25 February 2016 (blue) and 17 February 2016 (green) are not substantively different in magnitude or trend with snow-covered ground (>30 cm) or bare ground in the same season and at afternoon maximum temperatures of 9.4°C and 13°C, respectively.

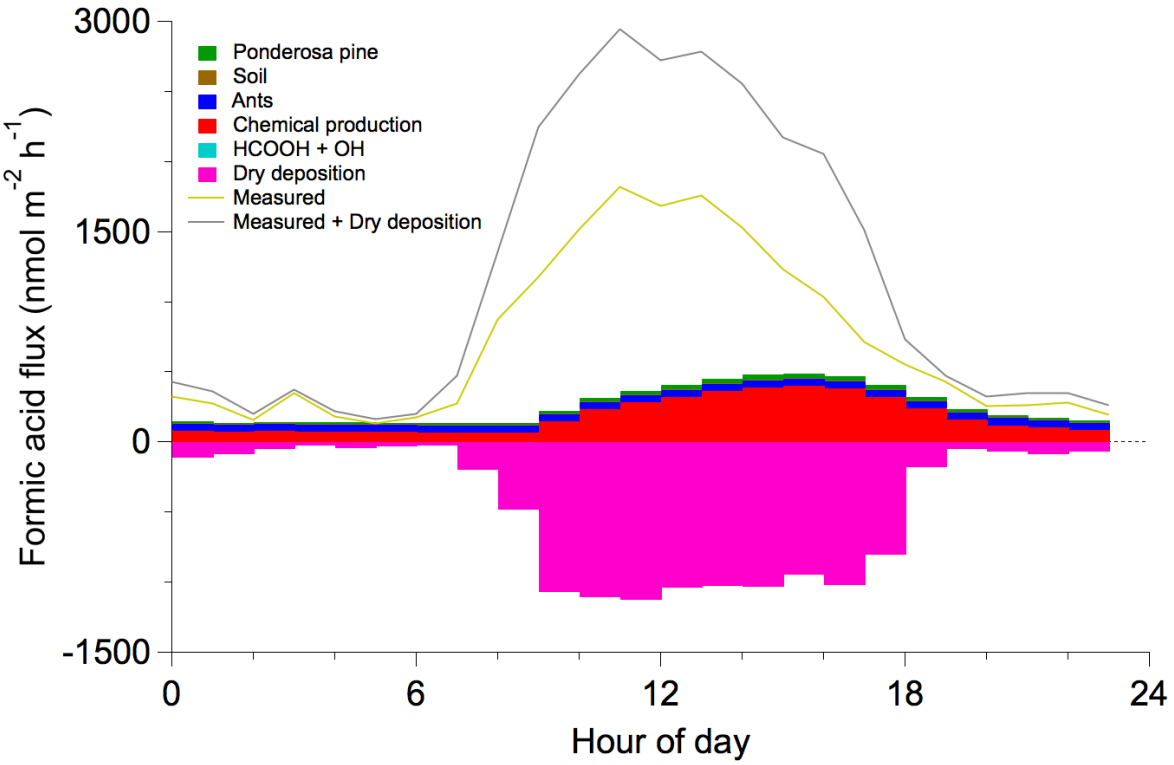

Figure 2.5. Diel formic acid flux budget for SPiFFY fall campaign. Budget totals represent the sum of all sources and sinks – measured, where available, and modeled using upper-bound estimates. The budget total accounts for approximately one-third of the measured daytime flux. The budget total poorly recreates the substantial difference between day and nighttime fluxes seen in the measured fluxes.

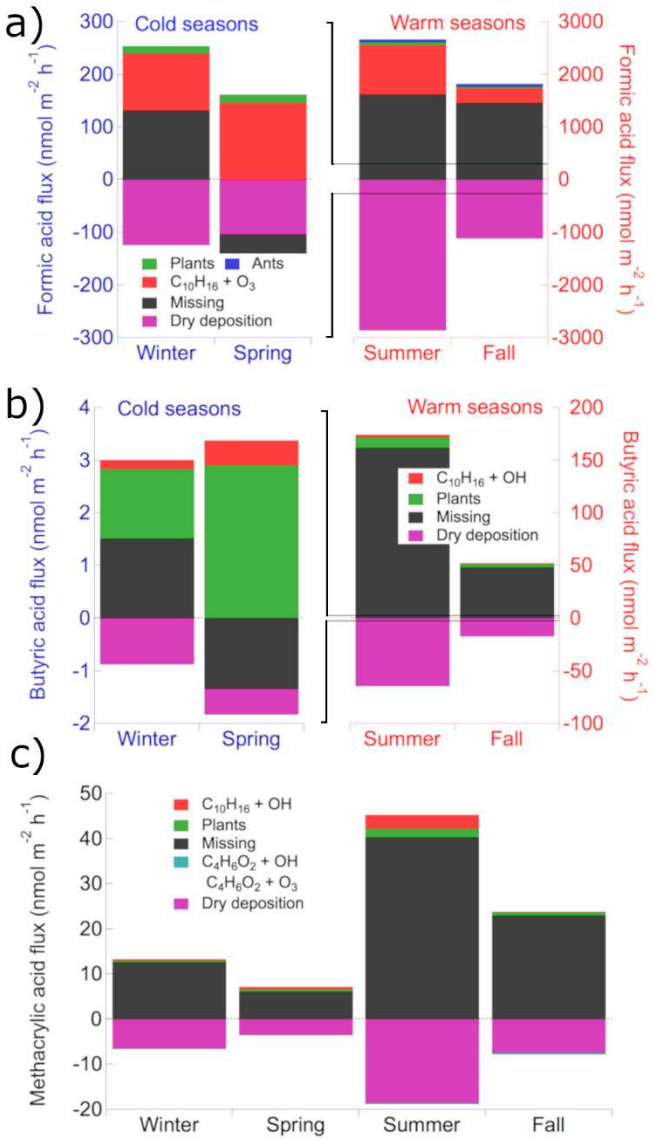

Figure 2.6. Seasonal budgets of a) formic, b) butyric, and c) methacrylic acid fluxes (nmol m^{-2} h^{-1}) increase in magnitude substantially during summer and fall. Winter and spring (cold seasons, blue) are separated from summer and fall (warm seasons, red) for butyric and formic acid budgets. Brackets relate the scale of cold season axes to the warm seasons. Budget values are chosen according to the hour of day at which the sum of the measured flux and dry deposition is maximized during each season.

Chapter 2 Tables

Table 2.1. Seasonal averages ± 1 standard deviation of environmental conditions at MEFO (measurements taken at 27.8 m a.g.l.). Seasonal maxima and minima are in parentheses. Daytime hours are taken as 8:00–18:00 local time, and nighttime hours 19:00–7:00. PPFD is measured at the U.S. Forest Service main office (~2 km east of the site) and includes down-welling solar radiation at 3 m a.g.l.

		Relative Humidity (%)	Temperature (°C)	Wind Speed (m s^{-1})	Wind direction (°)	PPFD (μmol m^{-2} s^{-1})
		μ ± σ	μ ± σ	μ ± σ	μ	μ ± σ
		(min – max)	(min – max)	(min – max)		(min – max)
	Day	30 ± 10	7 ± 5	4 ± 2	314	200 ± 300
Winter		(8.0 – 88)	(-7.0 – 16)	(0.25 – 11)		(0.0 – 1000)
	Night	40 ± 20	0 ± 5	3 ± 1	154	
		(15 – 89)	(-13 – 11)	(0.22 – 6.9)		
	Day	40 ± 20	10 ± 6	4 ± 2	279	280 ± 400
Spring		(0.0 – 93)	(-3.7 – 21)	(0.0 – 18)		(0.0 – 1300)
	Night	60 ± 20	3 ± 5	2 ± 1	161	
		(0.0 – 93)	(-8.1 – 18)	(0.0 – 10)		
	Day	30 ± 20	23 ± 4	3 ± 1	119	330 ± 400
Summer		(0.0 – 86)	(11 – 29)	(0.0 – 10)		(0.0 – 1200)
	Night	60 ± 20	14 ± 3	2 ± 1	145	
		(7.0 – 91)	(5.7 – 29)	(0.10 – 10)		
	Day	30 ± 10	15 ± 4	3 ± 2	343	290 ± 400

Fall		(0.0 – 92)	(0.5 – 23)	(0.0 – 11)		(0.0 – 1200)
	Night	50 ± 20	6 ± 5	2 ± 1	146	
		(13 – 92)	(-7.1 – 20)	(0.20 – 12)		

Table 2.2. Seasonal averages ± standard deviations of organic acid (parts per trillion by volume, ppt_v) and trace gas (parts per billion or parts per million by volume, ppb_v or ppm_v) mixing ratios at MEFO. Seasonal maxima and minima are in parentheses. Daytime hours are 8:00 – 18:00 local time. Nighttime hours are 19:00 – 7:00.

	Winter	Spring	Summer	Fall
	$\mu \pm \sigma$	$\mu \pm \sigma$	$\mu \pm \sigma$	$\mu \pm \sigma$
	(min – max)	(min – max)	(min – max)	(min – max)
CH_2O_2	60 ± 60	30 ± 20	1200 ± 900	800 ± 500
(ppt_v)	(below detection limit (b.d.l.) – 950)	(b.d.l. – 150)	(66 – 8600)	(86 – 5200)
$C_3H_6O_2$	4 ± 2	2 ± 1	60 ± 40	30 ± 20
(ppt_v)	(b.d.l. – 25)	(b.d.l. – 11)	(b.d.l. – 380)	(b.d.l. – 170)
$C_4H_6O_2$	0.4 ± 0.2	0.3 ± 0.1	10. ± 8	4 ± 3
(ppt_v)	(b.d.l. – 9.2)	(b.d.l. – 2.8)	(b.d.l. – 140)	(b.d.l. – 27)
$C_4H_8O_2$	1.1 ± 0.7	0.9 ± 0.6	40 ± 30	12 ± 9
(ppt_v)	(b.d.l. – 22)	(b.d.l. – 7.4)	(b.d.l. – 250)	(b.d.l. – 87)
$C_5H_{10}O_2$	n/a	n/a	13 ± 9	6 ± 5
(ppt_v)			(b.d.l. – 85)	(b.d.l. – 59)
$C_7H_{14}O_2$	n/a	n/a	20 ± 10	10 ± 9
(ppt_v)			(b.d.l. – 210)	(b.d.l. – 140)
O_3	40 ± 10	40 ± 10	40 ± 20	35 ± 9
(ppb_v)	(0.40 – 84)	(1.5 – 82)	(1.1 – 97)	(4.0 – 60.)

NO_x	n/a	n/a	1.4 ± 0.9	1 ± 1
(ppb_v)			(0.42 – 6.9)	(b.d.l. – 8.1)
SO_2	n/a	n/a	0.6 ± 0.3	0.4 ± 0.3
(ppb_v)			(b.d.l. – 2.8)	(b.d.l. – 1.6)

Table 2.3. Percentage of organic acid fluxes (F_{acid}) that exceed corresponding flux detection limits (F_{unc}) during each season (see text for details of calculation). Fluxes in parentheses separate the percentages of qualifying flux periods between daytime (8:00–18:00; left) and nighttime (19:00–7:00; right). The CIMS was not calibrated for valeric and heptanoic acids in winter and spring, therefore fluxes for these acids during cold seasons are not available (n/a).

Season	Percentage (%) of flux periods in which $F_{acid} > F_{unc}$ (daytime, nighttime)					
	Formic	Propionic	Methacrylic	Butyric	Valeric	Heptanoic
Winter	68	16	9.0	26	n/a	n/a
	(89, 51)	(25, 9)	(14, 5)	(42, 14)		
Spring	68	35	17	45	n/a	n/a
	(90, 49)	(52, 20)	(22, 13)	(69, 24)		
Summer	65	40	27	47	40	23
	(86, 46)	(53, 29)	(41, 16)	(68, 28)	(55, 26)	(37, 11)
Fall	64	21	12	29	19	10
	(92, 40)	(35, 9)	(16, 8)	(48, 11)	(29, 11)	(14, 6)

Table 2.4. Column 3 contains branch enclosure measurements of 6 organic acid emissions from a representative ponderosa pine. The percentage of average daily maximum fluxes represented by enclosure emissions follow in column 4. Averages of three soil chamber measurements of 6 volatile organic acid fluxes from soil and leaf litter and the percentage of the average daily maximum flux accounted for by the chamber average complete the table.

Organic acid name	Branch enclosure		Soil chamber	
	flux (nmol m^{-2} h^{-1})	% of measured flux	flux (nmol m^{-2} h^{-1})	% of measured flux
Formic	94	2.5	1.1×10^{-2}	<1
Propionic	26	41	6.9×10^{-4}	<1
Methacrylic	2.6	18	-2.2×10^{-7}	<1
Butyric	15	24	3.8×10^{-4}	<1
Valeric	7.3	32	1.8×10^{-4}	<1
Heptanoic	2.7	12	6.7×10^{-5}	<1

REFERENCES

(1) Chebbi, A.; Carlier, P. Carboxylic Acids in the Troposphere, Occurrence, Sources, and Sinks: A Review. *Atmos. Environ.* **1996**, *30* (24), 4233–4249. https://doi.org/10.1016/1352-2310(96)00102-1.

(2) Hellén, H.; Schallhart, S.; Praplan, A. P.; Petäjä, T.; Hakola, H. Using in Situ GC-MS for Analysis of C2–C7 Volatile Organic Acids in Ambient Air of a Boreal Forest Site. *Atmos Meas Tech* **2017**, *10* (1), 281–289. https://doi.org/10.5194/amt-10-281-2017.

(3) Khare, P.; Kumar, N.; Kumari, K. M.; Srivastava, S. S. Atmospheric Formic and Acetic Acids: An Overview. *Rev. Geophys.* **1999**, *37* (2), 227–248. https://doi.org/10.1029/1998RG900005.

(4) Liggio, J.; Moussa, S. G.; Wentzell, J.; Darlington, A.; Liu, P.; Leithead, A.; Hayden, K.; O'Brien, J.; Mittermeier, R. L.; Staebler, R.; Wolde, M.; Li, S.-M. Understanding the Primary Emissions and Secondary Formation of Gaseous Organic Acids in the Oil Sands Region of Alberta, Canada. *Atmospheric Chem. Phys.* **2017**, *17* (13), 8411–8427. https://doi.org/10.5194/acp-17-8411-2017.

(5) Mellouki, A.; Wallington, T. J.; Chen, J. Atmospheric Chemistry of Oxygenated Volatile Organic Compounds: Impacts on Air Quality and Climate. *Chem. Rev.* **2015**, *115* (10), 3984–4014. https://doi.org/10.1021/cr500549n.

(6) Schobesberger, S.; Lopez-Hilfiker, F. D.; Taipale, D.; Millet, D. B.; D'Ambro, E. L.; Rantala, P.; Mammarella, I.; Zhou, P.; Wolfe, G. M.; Lee, B. H.; Boy, M.; Thornton, J. A. High Upward Fluxes of Formic Acid from a Boreal Forest Canopy. *Geophys. Res. Lett.* **2016**, 2016GL069599. https://doi.org/10.1002/2016GL069599.

(7) Vogel, A. L.; Äijälä, M.; Brüggemann, M.; Ehn, M.; Junninen, H.; Petäjä, T.; Worsnop, D. R.; Kulmala, M.; Williams, J.; Hoffmann, T. Online Atmospheric Pressure Chemical Ionization Ion Trap Mass Spectrometry (APCI-IT-MSn) for Measuring Organic Acids in Concentrated Bulk Aerosol – a Laboratory and Field Study. *Atmos Meas Tech* **2013**, *6* (2), 431–443. https://doi.org/10.5194/amt-6-431-2013.

(8) Yatavelli, R. L. N.; Stark, H.; Thompson, S. L.; Kimmel, J. R.; Cubison, M. J.; Day, D. A.; Campuzano-Jost, P.; Palm, B. B.; Hodzic, A.; Thornton, J. A.; Jayne, J. T.; Worsnop, D. R.; Jimenez, J. L. Semicontinuous Measurements of Gas–Particle Partitioning of Organic Acids in a Ponderosa Pine Forest Using a MOVI-HRToF-CIMS. *Atmos Chem Phys* **2014**, *14* (3), 1527–1546. https://doi.org/10.5194/acp-14-1527-2014.

(9) Davidson, C. I.; Phalen, R. F.; Solomon, P. A. Airborne Particulate Matter and Human Health: A Review. *Aerosol Sci. Technol.* **2005**, *39* (8), 737–749. https://doi.org/10.1080/02786820500191348.

(10) IPCC. *Fifth Assessment Report: Climate Change 2013: The Physical Science Basis, Contribution of Working Group I to the Fifth Assessment Report of the Intergovernmental Panel on Climate Change*; 5.

(11) Jacob, D. J. Chemistry of OH in Remote Clouds and Its Role in the Production of Formic Acid and Peroxymonosulfate. *J. Geophys. Res. Atmospheres* **1986**, *91* (D9), 9807–9826. https://doi.org/10.1029/JD091iD09p09807.

(12) Paulot, F.; Wunch, D.; Crounse, J. D.; Toon, G. C.; Millet, D. B.; DeCarlo, P. F.; Vigouroux, C.; Deutscher, N. M.; González Abad, G.; Notholt, J.; Warneke, T.; Hannigan, J. W.; Warneke, C.; de Gouw, J. A.; Dunlea, E. J.; De Mazière, M.; Griffith, D. W. T.; Bernath, P.; Jimenez, J. L.; Wennberg, P. O. Importance of Secondary Sources in the Atmospheric Budgets of Formic and Acetic Acids. *Atmos Chem Phys* **2011**, *11* (5), 1989–2013. https://doi.org/10.5194/acp-11-1989-2011.

(13) Alwe, H. D.; Millet, D. B.; Chen, X.; Raff, J. D.; Payne, Z. C.; Fledderman, K. Oxidation of Volatile Organic Compounds as the Major Source of Formic Acid in a Mixed Forest Canopy. *Geophys. Res. Lett.* **2019**, *46* (5), 2940–2948. https://doi.org/10.1029/2018GL081526.

(14) Millet, D. B.; Baasandorj, M.; Farmer, D. K.; Thornton, J. A.; Baumann, K.; Brophy, P.; Chaliyakunnel, S.; de Gouw, J. A.; Graus, M.; Hu, L.; Koss, A.; Lee, B. H.; Lopez-Hilfiker, F. D.; Neuman, J. A.; Paulot, F.; Peischl, J.; Pollack, I. B.; Ryerson, T. B.; Warneke, C.; Williams, B. J.; Xu, J. A Large and Ubiquitous Source of Atmospheric Formic Acid. *Atmos Chem Phys* **2015**, *15* (11), 6283–6304. https://doi.org/10.5194/acp-15-6283-2015.

(15) Stavrakou, T.; Müller, J.-F.; Peeters, J.; Razavi, A.; Clarisse, L.; Clerbaux, C.; Coheur, P.-F.; Hurtmans, D.; De Mazière, M.; Vigouroux, C.; Deutscher, N. M.; Griffith, D. W. T.; Jones, N.; Paton-Walsh, C. Satellite Evidence for a Large Source of Formic Acid from Boreal and Tropical Forests. *Nat. Geosci.* **2012**, *5* (1), 26–30. https://doi.org/10.1038/ngeo1354.

(16) Hellén, H.; Schallhart, S.; Praplan, A. P.; Petäjä, T.; Hakola, H. Using in Situ GC-MS for Analysis of C2-C7 Volatile Organic Acids in Ambient Air of a Boreal Forest Site. **2016**.

(17) Andreae, M. O.; Talbot, R. W.; Andreae, T. W.; Harriss, R. C. Formic and Acetic Acid over the Central Amazon Region, Brazil: 1. Dry Season. *J. Geophys. Res. Atmospheres* **1988**, *93* (D2), 1616–1624. https://doi.org/10.1029/JD093iD02p01616.

(18) Keene, W. C.; Galloway, J. N. Organic Acidity in Precipitation of North America. *Atmospheric Environ. 1967* **1984**, *18* (11), 2491–2497. https://doi.org/10.1016/0004-6981(84)90020-9.

(19) Kesselmeier, J. Exchange of Short-Chain Oxygenated Volatile Organic Compounds (VOCs) between Plants and the Atmosphere: A Compilation of Field and Laboratory Studies. *J. Atmospheric Chem.* **2001**, *39* (3), 219–233. https://doi.org/10.1023/A:1010632302076.

(20) Kesselmeier, J.; Bode, K.; Gerlach, C.; Jork, E.-M. Exchange of Atmospheric Formic and Acetic Acids with Trees and Crop Plants under Controlled Chamber and Purified Air Conditions. *Atmos. Environ.* **1998**, *32* (10), 1765–1775. https://doi.org/10.1016/S1352-2310(97)00465-2.

(21) Mielnik, A.; Link, M.; Mattila, J.; Fulgham, S. R.; Farmer, D. K. Emission of Formic and Acetic Acids from Two Colorado Soils. *Environ. Sci. Process. Impacts* **2018**. https://doi.org/10.1039/C8EM00356D.

(22) Peñuelas, J.; Asensio, D.; Tholl, D.; Wenke, K.; Rosenkranz, M.; Piechulla, B.; Schnitzler, J. p. Biogenic Volatile Emissions from the Soil. *Plant Cell Environ.* **2014**, *37* (8), 1866–1891. https://doi.org/10.1111/pce.12340.

(23) Graedel, T. E.; Eisner, T. Atmospheric Formic Acid from Formicine Ants: A Preliminary Assessment. *Tellus B* **1988**, *40B* (5), 335–339. https://doi.org/10.1111/j.1600-0889.1988.tb00107.x.

(24) Calvert, J. G.; Su, F.; Bottenheim, J. W.; Strausz, O. P. Mechanism of the Homogeneous Oxidation of Sulfur Dioxide in the Troposphere. *Atmospheric Environ. 1967* **1978**, *12* (1), 197–226. https://doi.org/10.1016/0004-6981(78)90201-9.

(25) Horie, O.; Neeb, P.; Limbach, S.; Moortgat, G. K. Formation of Formic Acid and Organic Peroxides in the Ozonolysis of Ethene with Added Water Vapour. *Geophys. Res. Lett.* **1994**, *21* (14), 1523–1526. https://doi.org/10.1029/94GL01174.

(26) Calvert, J. G.; Madronich, S. Theoretical Study of the Initial Products of the Atmospheric Oxidation of Hydrocarbons. *J. Geophys. Res. Atmospheres* **1987**, *92* (D2), 2211–2220. https://doi.org/10.1029/JD092iD02p02211.

(27) Chameides, W. L.; Davis, D. D. Aqueous-Phase Source of Formic Acid in Clouds. *Nature* **1983**, *304* (5925), 427–429. https://doi.org/10.1038/304427a0.

(28) Friedman, B.; Farmer, D. K. SOA and Gas Phase Organic Acid Yields from the Sequential Photooxidation of Seven Monoterpenes. *Atmos. Environ.* **2018**, *187*, 335–345. https://doi.org/10.1016/j.atmosenv.2018.06.003.

(29) Chattopadhyay, A.; Chatterjee, P.; Chakraborty, T. Photo-oxidation of Acetone to Formic Acid in Synthetic Air and Its Atmospheric Implication https://pubs.acs.org/doi/full/10.1021/acs.jpca.5b04905 (accessed Dec 10, 2018). https://doi.org/10.1021/acs.jpca.5b04905.

(30) Crutzen, P. J.; Andreae, M. O. Biomass Burning in the Tropics: Impact on Atmospheric Chemistry and Biogeochemical Cycles. *Science* **1990**, *250* (4988), 1669–1678. https://doi.org/10.1126/science.250.4988.1669.

(31) Goldstein, A. H.; Galbally, I. E. Known and Unexplored Organic Constituents in the Earth's Atmosphere. *Environ. Sci. Technol.* **2007**, *41* (5), 1514–1521. https://doi.org/10.1021/es072476p.

(32) Dawson G. A.; Farmer J. Carl. Soluble Atmospheric Trace Gases in the Southwestern United States: 2. Organic Species HCHO, HCOOH, CH3COOH. *J. Geophys. Res. Atmospheres* **2012**, *93* (D5), 5200–5206. https://doi.org/10.1029/JD093iD05p05200.

(33) Wine, P. H.; Astalos, R. J.; Mauldin, R. L. Kinetic and Mechanistic Study of the Hydroxyl + Formic Acid Reaction. *J. Phys. Chem.* **1985**, *89* (12), 2620–2624. https://doi.org/10.1021/j100258a037.

(34) Graedel, T. E. *Chemical Compounds in the Atmosphere*; Academic Press, 1978.

(35) Rosado-Reyes, C. M.; Francisco, J. S. Atmospheric Oxidation Pathways of Acetic Acid. *J. Phys. Chem. A* **2006**, *110* (13), 4419–4433. https://doi.org/10.1021/jp0567974.

(36) Graedel, T. E.; Weschler, C. J. Chemistry within Aqueous Atmospheric Aerosols and Raindrops. *Rev. Geophys.* **1981**, *19* (4), 505–539. https://doi.org/10.1029/RG019i004p00505.

(37) Jardine, K.; Yañez Serrano, A.; Arneth, A.; Abrell, L.; Jardine, A.; Artaxo, P.; Alves, E.; Kesselmeier, J.; Taylor, T.; Saleska, S.; Huxman, T. Ecosystem-Scale Compensation Points of Formic and Acetic Acid in the Central Amazon. *Biogeosciences* **2011**, *8* (12), 3709–3720. https://doi.org/10.5194/bg-8-3709-2011.

(38) Juráň, S.; Pallozzi, E.; Guidolotti, G.; Fares, S.; Šigut, L.; Calfapietra, C.; Alivernini, A.; Savi, F.; Večeřová, K.; Křůmal, K.; Večeřa, Z.; Urban, O. Fluxes of Biogenic Volatile Organic Compounds above Temperate Norway Spruce Forest of the Czech Republic. *Agric. For. Meteorol.* **2017**, *232*, 500–513. https://doi.org/10.1016/j.agrformet.2016.10.005.

(39) Kaser, L.; Karl, T.; Guenther, A.; Graus, M.; Schnitzhofer, R.; Turnipseed, A.; Fischer, L.; Harley, P.; Madronich, M.; Gochis, D.; Keutsch, F. N.; Hansel, A. Undisturbed and Disturbed above Canopy Ponderosa Pine Emissions: PTR-TOF-MS Measurements and MEGAN 2.1 Model

Results. *Atmospheric Chem. Phys.* **2013**, *13* (23), 11935–11947. https://doi.org/10.5194/acp-13-11935-2013.

(40) Nguyen, T. B.; Crounse, J. D.; Teng, A. P.; Clair, J. M. S.; Paulot, F.; Wolfe, G. M.; Wennberg, P. O. Rapid Deposition of Oxidized Biogenic Compounds to a Temperate Forest. *Proc. Natl. Acad. Sci.* **2015**, *112* (5), E392–E401. https://doi.org/10.1073/pnas.1418702112.

(41) Park, J.-H.; Goldstein, A. H.; Timkovsky, J.; Fares, S.; Weber, R.; Karlik, J.; Holzinger, R. Active Atmosphere-Ecosystem Exchange of the Vast Majority of Detected Volatile Organic Compounds. *Science* **2013**, *341* (6146), 643–647. https://doi.org/10.1126/science.1235053.

(42) Schallhart, S.; Rantala, P.; Kajos, M. K.; Aalto, J.; Mammarella, I.; Ruuskanen, T. M.; Kulmala, M. Temporal Variation of VOC Fluxes Measured with PTR-TOF above a Boreal Forest. *Atmos Chem Phys* **2018**, *18* (2), 815–832. https://doi.org/10.5194/acp-18-815-2018.

(43) Shaw, W. J.; Spicer, C. W.; Kenny, D. V. Eddy Correlation Fluxes of Trace Gases Using a Tandem Mass Spectrometer. *Atmos. Environ.* **1998**, *32* (17), 2887–2898. https://doi.org/10.1016/S1352-2310(98)00036-3.

(44) Mattila, J. M.; Brophy, P.; Kirkland, J.; Hall, S.; Ullmann, K.; Fischer, E. V.; Brown, S.; McDuffie, E.; Tevlin, A.; Farmer, D. K. Tropospheric Sources and Sinks of Gas-Phase Acids in the Colorado Front Range. *Atmospheric Chem. Phys.* **2018**, *18* (16), 12315–12327. https://doi.org/10.5194/acp-18-12315-2018.

(45) Friedman, B.; Link, M. F.; Fulgham, S. R.; Brophy, P.; Galang, A.; Brune, W. H.; Jathar, S. H.; Farmer, D. K. Primary and Secondary Sources of Gas-Phase Organic Acids from Diesel Exhaust. *Environ. Sci. Technol.* **2017**, *51* (18), 10872–10880. https://doi.org/10.1021/acs.est.7b01169.

(46) Kawamura, Kimitaka.; Ng, L. Ling.; Kaplan, I. R. Determination of Organic Acids (C1-C10) in the Atmosphere, Motor Exhausts, and Engine Oils. *Environ. Sci. Technol.* **1985**, *19* (11), 1082–1086. https://doi.org/10.1021/es00141a010.

(47) Mungall, E. L.; Abbatt, J. P. D.; Wentzell, J. J. B.; Lee, A. K. Y.; Thomas, J. L.; Blais, M.; Gosselin, M.; Miller, L. A.; Papakyriakou, T.; Willis, M. D.; Liggio, J. Microlayer Source of Oxygenated Volatile Organic Compounds in the Summertime Marine Arctic Boundary Layer. *Proc. Natl. Acad. Sci.* **2017**, *114* (24), 6203–6208. https://doi.org/10.1073/pnas.1620571114.

(48) Mungall, E. L.; Abbatt, J. P. D.; Wentzell, J. J. B.; Wentworth, G. R.; Murphy, J. G.; Kunkel, D.; Gute, E.; Tarasick, D. W.; Sharma, S.; Cox, C. J.; Uttal, T.; Liggio, J. High Gas-Phase Mixing Ratios of Formic and Acetic Acid in the High Arctic. *Atmospheric Chem. Phys.* **2018**, *18* (14), 10237–10254. https://doi.org/10.5194/acp-18-10237-2018.

(49) Veres, P. R.; Roberts, J. M.; Cochran, A. K.; Gilman, J. B.; Kuster, W. C.; Holloway, J. S.; Graus, M.; Flynn, J.; Lefer, B.; Warneke, C.; de Gouw, J. Evidence of Rapid Production of Organic Acids in an Urban Air Mass. *Geophys. Res. Lett.* **2011**, *38* (17), L17807. https://doi.org/10.1029/2011GL048420.

(50) Ortega, J.; Turnipseed, A.; Guenther, A. B.; Karl, T. G.; Day, D. A.; Gochis, D.; Huffman, J. A.; Prenni, A. J.; Levin, E. J. T.; Kreidenweis, S. M.; DeMott, P. J.; Tobo, Y.; Patton, E. G.; Hodzic, A.; Cui, Y. Y.; Harley, P. C.; Hornbrook, R. S.; Apel, E. C.; Monson, R. K.; Eller, A. S. D.; Greenberg, J. P.; Barth, M. C.; Campuzano-Jost, P.; Palm, B. B.; Jimenez, J. L.; Aiken, A. C.; Dubey, M. K.; Geron, C.; Offenberg, J.; Ryan, M. G.; Fornwalt, P. J.; Pryor, S. C.; Keutsch, F. N.; DiGangi, J. P.; Chan, A. W. H.; Goldstein, A. H.; Wolfe, G. M.; Kim, S.; Kaser, L.; Schnitzhofer, R.; Hansel, A.; Cantrell, C. A.; Mauldin, R. L.; Smith, J. N. Overview of the Manitou Experimental Forest Observatory: Site Description and Selected Science Results from 2008 to 2013. *Atmos Chem Phys* **2014**, *14* (12), 6345–6367. https://doi.org/10.5194/acp-14-6345-2014.

(51) Asherin, L. A. *Manitou Experimental Forest Hourly Meteorology Data*; 2nd edition; Forest Service Research Data Archive: Fort Collins, CO, 2016.

(52) Brophy, P.; Farmer, D. K. A Switchable Reagent Ion High Resolution Time-of-Flight Chemical Ionization Mass Spectrometer for Real-Time Measurement of Gas Phase Oxidized Species: Characterization from the 2013 Southern Oxidant and Aerosol Study. *Atmos Meas Tech* **2015**, *8* (7), 2945–2959. https://doi.org/10.5194/amt-8-2945-2015.

(53) Brophy, P.; Farmer, D. K. Clustering, Methodology, and Mechanistic Insights into Acetate Chemical Ionization Using High-Resolution Time-of-Flight Mass Spectrometry. *Atmos Meas Tech* **2016**, *9* (8), 3969–3986. https://doi.org/10.5194/amt-9-3969-2016.

(54) Roberts, J. M.; Veres, P.; Warneke, C.; Neuman, J. A.; Washenfelder, R. A.; Brown, S. S.; Baasandorj, M.; Burkholder, J. B.; Burling, I. R.; Johnson, T. J.; Yokelson, R. J.; de Gouw, J. Measurement of HONO, HNCO, and Other Inorganic Acids by Negative-Ion Proton-Transfer Chemical-Ionization Mass Spectrometry (NI-PT-CIMS): Application to Biomass Burning Emissions. *Atmospheric Meas. Tech.* **2010**, *3* (4), 981.

(55) Veres, P.; Roberts, J. M.; Warneke, C.; Welsh-Bon, D.; Zahniser, M.; Herndon, S.; Fall, R.; de Gouw, J. Development of Negative-Ion Proton-Transfer Chemical-Ionization Mass Spectrometry (NI-PT-CIMS) for the Measurement of Gas-Phase Organic Acids in the Atmosphere. *Int. J. Mass Spectrom.* **2008**, *274* (1–3), 48–55. https://doi.org/10.1016/j.ijms.2008.04.032.

(56) Pagonis, D.; Krechmer, J. E.; Gouw, J. de; Jimenez, J. L.; Ziemann, P. J. Effects of Gas–Wall Partitioning in Teflon Tubing and Instrumentation on Time-Resolved Measurements of

Gas-Phase Organic Compounds. *Atmospheric Meas. Tech.* **2017**, *10* (12), 4687–4696. https://doi.org/10.5194/amt-10-4687-2017.

(57) Gill Instruments Ltd. *Software Bug Affecting 'w' Wind Component of the WindMaster Family*; technical key note KN1509v3*; 2016.

(58) Mauder, M.; Cuntz, M.; Drüe, C.; Graf, A.; Rebmann, C.; Schmid, H. P.; Schmidt, M.; Steinbrecher, R. A Strategy for Quality and Uncertainty Assessment of Long-Term Eddy-Covariance Measurements. *Agric. For. Meteorol.* **2013**, *169*, 122–135. https://doi.org/10.1016/j.agrformet.2012.09.006.

(59) Tanner, C. B.; Thurtell, G. W. *Anemoclinometer Measurements of Reynolds Stress and Heat Transport in the Atmospheric Surface Layer*; 1969.

(60) Baldocchi, D. D. Assessing the Eddy Covariance Technique for Evaluating Carbon Dioxide Exchange Rates of Ecosystems: Past, Present and Future. *Glob. Change Biol.* **2003**, *9* (4), 479–492. https://doi.org/10.1046/j.1365-2486.2003.00629.x.

(61) Webb, E. K.; Pearman, G. I.; Leuning, R. Correction of Flux Measurements for Density Effects Due to Heat and Water Vapour Transfer. *Q. J. R. Meteorol. Soc.* **1980**, *106* (447), 85–100. https://doi.org/10.1002/qj.49710644707.

(62) Papale, D.; Reichstein, M.; Aubinet, M.; Canfora, E.; Bernhofer, C.; Kutsch, W.; Longdoz, B.; Rambal, S.; Valentini, R.; Vesala, T.; Yakir, D. Towards a Standardized Processing of Net Ecosystem Exchange Measured with Eddy Covariance Technique: Algorithms and Uncertainty Estimation. *Biogeosciences* **2006**, *3* (4), 571–583. https://doi.org/10.5194/bg-3-571-2006.

(63) Falge, E.; Baldocchi, D.; Olson, R.; Anthoni, P.; Aubinet, M.; Bernhofer, C.; Burba, G.; Ceulemans, R.; Clement, R.; Dolman, H.; Granier, A.; Gross, P.; Grünwald, T.; Hollinger, D.; Jensen, N.-O.; Katul, G.; Keronen, P.; Kowalski, A.; Lai, C. T.; Law, B. E.; Meyers, T.; Moncrieff, J.; Moors, E.; Munger, J. W.; Pilegaard, K.; Rannik, Ü.; Rebmann, C.; Suyker, A.; Tenhunen, J.; Tu, K.; Verma, S.; Vesala, T.; Wilson, K.; Wofsy, S. Gap Filling Strategies for Defensible Annual Sums of Net Ecosystem Exchange. *Agric. For. Meteorol.* **2001**, *107* (1), 43–69. https://doi.org/10.1016/S0168-1923(00)00225-2.

(64) Reichstein, M.; Falge, E.; Baldocchi, D.; Papale, D.; Aubinet, M.; Berbigier, P.; Bernhofer, C.; Buchmann, N.; Gilmanov, T.; Granier, A.; Grünwald, T.; Havránková, K.; Ilvesniemi, H.; Janous, D.; Knohl, A.; Laurila, T.; Lohila, A.; Loustau, D.; Matteucci, G.; Meyers, T.; Miglietta, F.; Ourcival, J.-M.; Pumpanen, J.; Rambal, S.; Rotenberg, E.; Sanz, M.; Tenhunen, J.; Seufert, G.; Vaccari, F.; Vesala, T.; Yakir, D.; Valentini, R. On the Separation of Net Ecosystem Exchange into Assimilation and Ecosystem Respiration: Review and Improved

Algorithm. *Glob. Change Biol.* **2005**, *11* (9), 1424–1439. https://doi.org/10.1111/j.1365-2486.2005.001002.x.

(65) Foken, Th.; Wichura, B. Tools for Quality Assessment of Surface-Based Flux Measurements. *Agric. For. Meteorol.* **1996**, *78* (1), 83–105. https://doi.org/10.1016/0168-1923(95)02248-1.

(66) Kljun, N.; Calanca, P.; Rotach, M. W.; Schmid, H. P. A Simple Two-Dimensional Parameterisation for Flux Footprint Prediction (FFP). *Geosci Model Dev* **2015**, *8* (11), 3695–3713. https://doi.org/10.5194/gmd-8-3695-2015.

(67) Spirig, C.; Neftel, A.; Ammann, C.; Dommen, J.; Grabmer, W.; Thielmann, A.; Schaub, A.; Beauchamp, J.; Wisthaler, A.; Hansel, A. Eddy Covariance Flux Measurements of Biogenic VOCs during ECHO 2003 Using Proton Transfer Reaction Mass Spectrometry. *Atmos Chem Phys* **2005**, *5* (2), 465–481. https://doi.org/10.5194/acp-5-465-2005.

(68) Wienhold, F. G.; Welling, M.; Harris, G. W. Micrometeorological Measurement and Source Region Analysis of Nitrous Oxide Fluxes from an Agricultural Soil. *Atmos. Environ.* **1995**, *29* (17), 2219–2227. https://doi.org/10.1016/1352-2310(95)00165-U.

(69) Geddes, J. A.; Murphy, J. G. Observations of Reactive Nitrogen Oxide Fluxes by Eddy Covariance above Two Midlatitude North American Mixed Hardwood Forests. *Atmospheric Chem. Phys.* **2014**, *14* (6), 2939–2957. https://doi.org/10.5194/acp-14-2939-2014.

(70) Karl, T.; Harley, P.; Guenther, A.; Rasmussen, R.; Baker, B.; Jardine, K.; Nemitz, E. The Bi-Directional Exchange of Oxygenated VOCs between a Loblolly Pine (<I>Pinus Taeda</I>) Plantation and the Atmosphere. *Atmospheric Chem. Phys.* **2005**, *5* (11), 3015–3031. https://doi.org/10.5194/acp-5-3015-2005.

(71) Wolfe, G. M.; Thornton, J. A.; Yatavelli, R. L. N.; McKay, M.; Goldstein, A. H.; LaFranchi, B.; Min, K.-E.; Cohen, R. C. Eddy Covariance Fluxes of Acyl Peroxy Nitrates (PAN, PPN and MPAN) above a Ponderosa Pine Forest. *Atmos Chem Phys* **2009**, *9* (2), 615–634. https://doi.org/10.5194/acp-9-615-2009.

(72) Hartmann, W. R.; Santana, M.; Hermoso, M.; Andreae, M. O.; Sanhueza, E. Diurnal Cycles of Formic and Acetic Acids in the Northern Part of the Guayana Shield, Venezuela. *J. Atmospheric Chem.* **1991**, *13* (1), 63–72. https://doi.org/10.1007/BF00048100.

(73) Guenther, A.; Hewitt, C. N.; Erickson, D.; Fall, R.; Geron, C.; Graedel, T.; Harley, P.; Klinger, L.; Lerdau, M.; Mckay, W. A.; Pierce, T.; Scholes, B.; Steinbrecher, R.; Tallamraju, R.; Taylor, J.; Zimmerman, P. A Global Model of Natural Volatile Organic Compound Emissions. *J. Geophys. Res. Atmospheres* **1995**, *100* (D5), 8873–8892. https://doi.org/10.1029/94JD02950.

(74) Guenther, A.; Karl, T.; Harley, P.; Wiedinmyer, C.; Palmer, P. I.; Geron, C. Estimates of Global Terrestrial Isoprene Emissions Using MEGAN (Model of Emissions of Gases and Aerosols from Nature). *Atmospheric Chem. Phys.* **2006**, *6* (11), 3181–3210. https://doi.org/10.5194/acp-6-3181-2006.

(75) Kesselmeier, J.; Staudt, M. Biogenic Volatile Organic Compounds (VOC): An Overview on Emission, Physiology and Ecology. *J. Atmospheric Chem.* **1999**, *33* (1), 23–88. https://doi.org/10.1023/A:1006127516791.

(76) Seco, R.; Peñuelas, J.; Filella, I. Short-Chain Oxygenated VOCs: Emission and Uptake by Plants and Atmospheric Sources, Sinks, and Concentrations. *Atmos. Environ.* **2007**, *41* (12), 2477–2499. https://doi.org/10.1016/j.atmosenv.2006.11.029.

(77) Villanueva-Fierro, I.; Popp, C. J.; Martin, R. S. Biogenic Emissions and Ambient Concentrations of Hydrocarbons, Carbonyl Compounds and Organic Acids from Ponderosa Pine and Cottonwood Trees at Rural and Forested Sites in Central New Mexico. *Atmos. Environ.* **2004**, *38* (2), 249–260. https://doi.org/10.1016/j.atmosenv.2003.09.051.

(78) Kesselmeier, J.; Bode, K.; Hofmann, U.; Müller, H.; Schäfer, L.; Wolf, A.; Ciccioli, P.; Brancaleoni, E.; Cecinato, A.; Frattoni, M.; Foster, P.; Ferrari, C.; Jacob, V.; Fugit, J. L.; Dutaur, L.; Simon, V.; Torres, L. Emission of Short Chained Organic Acids, Aldehydes and Monoterpenes from Quercus Ilex L. and Pinus Pinea L. in Relation to Physiological Activities, Carbon Budget and Emission Algorithms. *Atmos. Environ.* **1997**, *31* (Supplement 1), 119–133. https://doi.org/10.1016/S1352-2310(97)00079-4.

(79) Helmig, D.; Ortega, J.; Guenther, A.; Herrick, J. D.; Geron, C. Sesquiterpene Emissions from Loblolly Pine and Their Potential Contribution to Biogenic Aerosol Formation in the Southeastern US. *Atmos. Environ.* **2006**, *40* (22), 4150–4157. https://doi.org/10.1016/j.atmosenv.2006.02.035.

(80) Insam, H.; Seewald, M. S. A. Volatile Organic Compounds (VOCs) in Soils. *Biol. Fertil. Soils* **2010**, *46* (3), 199–213. https://doi.org/10.1007/s00374-010-0442-3.

(81) Leff, J. W.; Fierer, N. Volatile Organic Compound (VOC) Emissions from Soil and Litter Samples. *Soil Biol. Biochem.* **2008**, *40* (7), 1629–1636. https://doi.org/10.1016/j.soilbio.2008.01.018.

(82) Sanhueza, E.; Andreae, M. O. Emission of Formic and Acetic Acids from Tropical Savanna Soils. *Geophys. Res. Lett.* **1991**, *18* (9), 1707–1710. https://doi.org/10.1029/91GL01565.

(83) Gray, C. M.; Monson, R. K.; Fierer, N. Biotic and Abiotic Controls on Biogenic Volatile Organic Compound Fluxes from a Subalpine Forest Floor. *J. Geophys. Res. Biogeosciences* **2014**, *119* (4), 2013JG002575. https://doi.org/10.1002/2013JG002575.

(84) Mooney, K. The Disruption of an Ant–Aphid Mutualism Increases the Effect of Birds on Pine Herbivores. *Ecology* **2006**, *87*, 1805–1815. https://doi.org/10.1890/0012-9658(2006)87[1805:TDOAAM]2.0.CO;2.

(85) Conway, J. R. A Field Study of the Nesting Ecology of the Thatching Ant, Formica Obscuripes Forel, at High Altitude in Colorado. *Gt. Basin Nat.* **1996**, *56* (4), 326–332.

(86) Crist, T. O.; Wiens, J. A. The Distribution of Ant Colonies in a Semiarid Landscape: Implications for Community and Ecosystem Processes. *Oikos* **1996**, *76* (2), 301–311. https://doi.org/10.2307/3546202.

(87) Jenkin, M. E.; Saunders, S. M.; Pilling, M. J. The Tropospheric Degradation of Volatile Organic Compounds: A Protocol for Mechanism Development. *Atmos. Environ.* **1997**, *31* (1), 81–104. https://doi.org/10.1016/S1352-2310(96)00105-7.

(88) Saunders, S. M.; Jenkin, M. E.; Derwent, R. G.; Pilling, M. J. Protocol for the Development of the Master Chemical Mechanism, MCM v3 (Part A): Tropospheric Degradation of Non-Aromatic Volatile Organic Compounds. *Atmospheric Chem. Phys.* **2003**, *3* (1), 161–180. https://doi.org/10.5194/acp-3-161-2003.

(89) Farmer, D. K.; Wooldridge, P. J.; Cohen, R. C. Application of Thermal-Dissociation Laser Induced Fluorescence (TD-LIF) to Measurement of HNO3, Σalkyl Nitrates, Σperoxy Nitrates, and NO2 Fluxes Using Eddy Covariance. *Atmos Chem Phys* **2006**, *6* (11), 3471–3486. https://doi.org/10.5194/acp-6-3471-2006.

(90) Farmer, D. K.; Kimmel, J. R.; Phillips, G.; Docherty, K. S.; Worsnop, D. R.; Sueper, D.; Nemitz, E.; Jimenez, J. L. Eddy Covariance Measurements with High-Resolution Time-of-Flight Aerosol Mass Spectrometry: A New Approach to Chemically Resolved Aerosol Fluxes. *Atmos Meas Tech* **2011**, *4* (6), 1275–1289. https://doi.org/10.5194/amt-4-1275-2011.

(91) Nemitz, E.; Sutton, M. A. Gas-Particle Interactions above a Dutch Heathland: III. Modelling the Influence of the NH3-HNO3-NH4NO3 Equilibrium on Size-Segregated Particle Fluxes. *Atmos Chem Phys* **2004**, *4* (4), 1025–1045. https://doi.org/10.5194/acp-4-1025-2004.

(92) Trebs, I.; Lara, L. L.; Zeri, L. M. M.; Gatti, L. V.; Artaxo, P.; Dlugi, R.; Slanina, J.; Andreae, M. O.; Meixner, F. X. Dry and Wet Deposition of Inorganic Nitrogen Compounds to a Tropical Pasture Site (Rondônia, Brazil). *Atmospheric Chem. Phys.* **2006**, *6* (2), 447–469. https://doi.org/10.5194/acp-6-447-2006.

(93) Bouvier-Brown, N. C.; Schade, G. W.; Misson, L.; Lee, A.; McKay, M.; Goldstein, A. H. Contributions of Biogenic Volatile Organic Compounds to Net Ecosystem Carbon Flux in a Ponderosa Pine Plantation. *Atmos. Environ.* **2012**, *60*, 527–533. https://doi.org/10.1016/j.atmosenv.2012.06.070.

(94) Hunter, J. F.; Day, D. A.; Palm, B. B.; Yatavelli, R. L. N.; Chan, A. W. H.; Kaser, L.; Cappellin, L.; Hayes, P. L.; Cross, E. S.; Carrasquillo, A. J.; Campuzano-Jost, P.; Stark, H.; Zhao, Y.; Hohaus, T.; Smith, J. N.; Hansel, A.; Karl, T.; Goldstein, A. H.; Guenther, A.; Worsnop, D. R.; Thornton, J. A.; Heald, C. L.; Jimenez, J. L.; Kroll, J. H. Comprehensive Characterization of Atmospheric Organic Carbon at a Forested Site. *Nat. Geosci.* **2017**, *10* (10), 748–753. https://doi.org/10.1038/ngeo3018.

(95) Karl, T.; Kaser, L.; Turnipseed, A. Eddy Covariance Measurements of Isoprene and 232-MBO Based on NO+ Time-of-Flight Mass Spectrometry. *Int. J. Mass Spectrom.* **2014**, *365* (Supplement C), 15–19. https://doi.org/10.1016/j.ijms.2013.12.002.

(96) Fantechi, G.; Jensen, N. R.; Hjorth, J.; Peeters, J. Mechanistic Studies of the Atmospheric Oxidation of Methyl Butenol by OH Radicals, Ozone and NO3 Radicals. *Atmos. Environ.* **1998**, *32* (20), 3547–3556. https://doi.org/10.1016/S1352-2310(98)00061-2.

(97) Lee, A.; Goldstein, A. H.; Kroll, J. H.; Ng, N. L.; Varutbangkul, V.; Flagan, R. C.; Seinfeld, J. H. Gas-Phase Products and Secondary Aerosol Yields from the Photooxidation of 16 Different Terpenes. *J. Geophys. Res. Atmospheres* **2006**, *111* (D17), D17305. https://doi.org/10.1029/2006JD007050.

(98) Lee, A.; Goldstein, A. H.; Keywood, M. D.; Gao, S.; Varutbangkul, V.; Bahreini, R.; Ng, N. L.; Flagan, R. C.; Seinfeld, J. H. Gas-Phase Products and Secondary Aerosol Yields from the Ozonolysis of Ten Different Terpenes. *J. Geophys. Res. Atmospheres* **2006**, *111* (D7), D07302. https://doi.org/10.1029/2005JD006437.

(99) Martens, C. S.; Shay, T. J.; Mendlovitz, H. P.; Matross, D. M.; Saleska, S. R.; Wofsy, S. C.; Stephen Woodward, W.; Menton, M. C.; De Moura, J. M. S.; Crill, P. M.; De Moraes, O. L. L.; Lima, R. L. Radon Fluxes in Tropical Forest Ecosystems of Brazilian Amazonia: Night-Time CO2 Net Ecosystem Exchange Derived from Radon and Eddy Covariance Methods. *Glob. Change Biol.* **2004**, *10* (5), 618–629. https://doi.org/10.1111/j.1365-2486.2004.00764.x.

(100) Wolfe, G. M.; Cantrell, C.; Kim, S.; Mauldin III, R. L.; Karl, T.; Harley, P.; Turnipseed, A.; Zheng, W.; Flocke, F.; Apel, E. C.; Hornbrook, R. S.; Hall, S. R.; Ullmann, K.; Henry, S. B.; DiGangi, J. P.; Boyle, E. S.; Kaser, L.; Schnitzhofer, R.; Hansel, A.; Graus, M.; Nakashima, Y.; Kajii, Y.; Guenther, A.; Keutsch, F. N. Missing Peroxy Radical Sources within a Summertime Ponderosa Pine Forest. *Atmos Chem Phys* **2014**, *14* (9), 4715–4732. https://doi.org/10.5194/acp-14-4715-2014.

(101) Wesely, M. L. Parameterization of Surface Resistances to Gaseous Dry Deposition in Regional-Scale Numerical Models. *Atmospheric Environ. 1967* **1989**, *23* (6), 1293–1304.

(102) Goldstein, A. H.; McKay, M.; Kurpius, M. R.; Schade, G. W.; Lee, A.; Holzinger, R.; Rasmussen, R. A. Forest Thinning Experiment Confirms Ozone Deposition to Forest Canopy Is Dominated by Reaction with Biogenic VOCs. *Geophys. Res. Lett.* **2004**, *31* (22), L22106. https://doi.org/10.1029/2004GL021259.

(103) Atkinson, R.; Arey, J. Gas-Phase Tropospheric Chemistry of Biogenic Volatile Organic Compounds: A Review. *Atmos. Environ.* **2003**, *37, Supplement 2*, 197–219. https://doi.org/10.1016/S1352-2310(03)00391-1.

(104) Bouvier-Brown, N. C.; Goldstein, A. H.; Worton, D. R.; Matross, D. M.; Gilman, J. B.; Kuster, W. C.; Welsh-Bon, D.; Warneke, C.; Gouw, J. A. de; Cahill, T. M.; Holzinger, R. Methyl Chavicol: Characterization of Its Biogenic Emission Rate, Abundance, and Oxidation Products in the Atmosphere. *Atmospheric Chem. Phys.* **2009**, *9* (6), 2061–2074. https://doi.org/10.5194/acp-9-2061-2009.

(105) Travaini, R.; Martín-Juárez, J.; Lorenzo-Hernando, A.; Bolado-Rodríguez, S. Ozonolysis: An Advantageous Pretreatment for Lignocellulosic Biomass Revisited. *Bioresour. Technol.* **2016**, *199*, 2–12. https://doi.org/10.1016/j.biortech.2015.08.143.

(106) Wentworth, G. R.; Murphy, J. G.; Benedict, K. B.; Bangs, E. J.; Collett Jr., J. L. The Role of Dew as a Night-Time Reservoir and Morning Source for Atmospheric Ammonia. *Atmos Chem Phys* **2016**, *16* (11), 7435–7449. https://doi.org/10.5194/acp-16-7435-2016.

(107) Eller, A. S. D.; Harley, P.; Monson, R. K. Potential Contribution of Exposed Resin to Ecosystem Emissions of Monoterpenes. *Atmos. Environ.* **2013**, *77* (Supplement C), 440–444. https://doi.org/10.1016/j.atmosenv.2013.05.028.

(108) Wang, Z.-P.; Gu, Q.; Deng, F.-D.; Huang, J.-H.; Megonigal, J. P.; Yu, Q.; Lü, X.-T.; Li, L.-H.; Chang, S.; Zhang, Y.-H.; Feng, J.-C.; Han, X.-G. Methane Emissions from the Trunks of Living Trees on Upland Soils. *New Phytol.* **2016**, *211* (2), 429–439. https://doi.org/10.1111/nph.13909.

(109) Warner, D. L.; Villarreal, S.; McWilliams, K.; Inamdar, S.; Vargas, R. Carbon Dioxide and Methane Fluxes From Tree Stems, Coarse Woody Debris, and Soils in an Upland Temperate Forest. *Ecosystems* **2017**, *20* (6), 1205–1216. https://doi.org/10.1007/s10021-016-0106-8.

CHAPTER 3

SURFACE WETNESS AS AN UNEXPECTED CONTROL ON FOREST EXCHANGE OF VOLATILE ORGANIC ACIDS

3.1 Introduction

The exchange of reactive trace gases between ecosystems and the atmosphere drives the source of much atmospheric organic carbon. However, trace gas fluxes from the biosphere can be bidirectional,[1–4] and deposition processes from the atmosphere to ecosystems are important sinks of many air pollutants including ozone[5] and oxidized organic precursors for secondary organic aerosol.[6] Measurement challenges coupled to the complexity of interpreting flux observations when multiple sources, sinks, and in-canopy chemistry are occurring mean that the processes driving bidirectional organic gas fluxes remain poorly understood. Here, we investigate a set of volatile organic acid flux observations and the role of surface wetness in controlling biosphere-atmosphere exchange.

Leaf wetness includes both water films and larger drops of water (i.e. dew) and can either enhance or inhibit plant-atmosphere gas exchange. The diffusion of CO_2 through water is 10^4 times slower than air, and wet leaves inhibit photosynthesis.[7] The impact of leaf wetness on photosynthesis depends on plant type and leaf wettability, which depends on the hydrophobicity of leaf surfaces. For example, with increasing water coverage, photosynthesis decreased in wettable bean plants, but increased in non-wettable pea plants.[8] However, this observation is not universal: morning dew reduced net ecosystem exchange of CO_2 over a non-wettable ponderosa pine plantation compared with dry mornings.[9] Surface wetness also controls the cuticular resistance of leaves to NH_3 deposition as a function of layer or droplet thickness and acidity. Generally, wetness increases NH_3 uptake[10] although alkaline water films suppress NH_3

deposition.[11] Leaf wetness can increase, decrease, or make no significant change to ozone deposition measured over a variety of forested and agricultural canopies.[12] Overall, the role of surface wetness in controlling trace gas fluxes is inconsistent in the literature and poorly understood.

Due to their water solubility and high volatility, volatile organic acids are well-suited to probe the influence of leaf wetness on bi-directional gas exchange. Fluxes of organic acids are poorly understood, with multiple studies observing unexplained upward fluxes of formic acid from forests.[13–16] We previously reported persistent upward fluxes of formic, butyric, propionic, methacrylic, valeric, and heptanoic acids at Manitou Experimental Forest.[14] Even after considering in-canopy oxidation of monoterpenes, these data suggested a missing source – or overestimated sink – of formic acid.

Here, we use observations from multiple field sites to explore leaf wetness and bidirectional fluxes of HNCO and other volatile acids.

3.2 Materials and Methods

3.2.1 Primary site description

Manitou Experimental Forest Observatory (MEFO) is a semi-arid coniferous forest in Colorado. The ~16 m tall canopy is sparse and almost exclusively ponderosa pine (*Pinus ponderosa*). Most annual precipitation is snowfall during winter and spring, although transient afternoon summer rainstorms occur. The site is well characterized.[14,17–21] Our work was part of the Seasonal Particles in Forests Flux studY (SPiFFY), which spanned four seasonally representative campaigns in 2016: winter (1 February – 1 March), spring (15 April – 15 May), summer (15 July – 15 August), and fall (1 October – 1 November).

3.2.2 MEFO flux measurements

We quantify volatile organic acids, including formic (HCOOH), propionic ($C_3H_6O_2$), methacrylic ($C_4H_6O_2$), butyric ($C_4H_8O_2$), valeric ($C_5H_{10}O_2$), heptanoic ($C_7H_{14}O_2$), and isocyanic (HNCO) acids, with a Time-of-Flight Chemical Ionization Mass Spectrometer (CIMS; Tofwerk AG and Aerodyne Research, Inc.) using acetate reagent ions. Chapter 2 details the instrument operation and online calibrations. As the CIMS was calibrated on-line for HCOOH, we used previous measurements of the relative sensitivity of HCOOH to HNCO taken on the same instrument to quantify HNCO.[22,23] Table A2.1 summarizes calibration sensitivities.

We measured the vertical exchange of acids from the 30 m MEFO tower using the eddy covariance technique(Section A2.1).[14]

3.3 HNCO

Atmospherically-relevant HNCO concentrations (≥1 ppb_v) are likely toxic to human health.[24] Combustion is a primary source,[22,25,26] while oxidation of amides is a secondary source of HNCO.[27] Due to the low reactivity of HNCO with atmospheric oxidants, wet and dry deposition are thought to be key removal processes. Dry deposition is expected to occur at a similar rate to formic acid and formaldehyde, resulting in lifetimes of weeks over land.[28] HNCO at MEFO ranges from 1 – 50 ppt_v, comparable to summertime background concentrations elsewhere.[29] Diel trends (Figure 3.1) are consistent with organic acids at the site,[14] suggesting photochemical sources.

Surprisingly, HNCO fluxes suggest persistent upward mid-day exchange during all seasons. Net deposition occurs at night during spring and summer (Figure 3.1). Bi-directional HNCO exchange is unexpected – there are no combustion sources within the flux footprint at MEFO. We filtered data for spikes in carbon monoxide concentration to exclude periods

influenced by local biomass burning. Plants are not sources of HNCO, and HNCO emissions were not observed during summer 2016 branch enclosure studies at MEFO.

Secondary production from in-canopy amide oxidation sufficient to produce the observed upward daytime exchange would have to produce a concentration gradient with higher HNCO levels in the canopy than above the sensor height. Amines are precursors for amides and thus HNCO, but amine levels at clean continental sites are typically low, on the order of <1 – 100 ppt.[30–32] There is no evidence for an adequately strong emission source of amines or amides within the flux footprint. Amine levels are significantly lower than ammonia; Hrdina et al.[33] reported in-canopy ammonia <1.5 ppb_v at Manitou. For these low levels of amides to produce enough HNCO to account for the observed upward flux, in-canopy oxidation would have to occur rapidly (residence time for air in forest canopies is typically <10 min; lifetime for oxidation of formamide is ~2 days given 1.5×10^6 molecules OH cm^{-3}) and to a greater extent than secondary production above the canopy. Amines require multiple oxidation steps to form HNCO and are unlikely to produce the observed exchange. Thus, we find no plausible explanation in the literature for the observed upward HNCO flux.

Here, we hypothesize that water films and droplets on ecosystem surfaces can mediate equilibrium partitioning of volatile acids. Under wet conditions, these acids tend to partition to wet ecosystem surfaces inducing a downward flux, while under dry conditions, water films or droplets dry out and release acids to the atmosphere, thereby causing an upward flux. While simple solubility suggests that these volatile acids would dominantly remain in the gas phase, dew is often more alkaline than natural water, or water equilibrated with ambient CO_2 (dew pH > pKa for these acids). The subsequent acid-base equilibria will enhance partitioning from the atmosphere to the aqueous phase, as will additional hydrolysis chemistry or reactions.

3.4 Evidence for partitioning to surface wetness

3.4.1 V_{ex} depends linearly on dew point depression

Dew point depression ($T-T_d$) is the difference between the air temperature and dew point temperature at a given height and describes the amount of water vapor in the air relative to saturation. Large $T-T_d$ values indicate drier air, and air parcels with small $T-T_d$ values are closer to saturated. For example, at dew point (i.e. $T-T_d = 0$ K) an air parcel is saturated with water vapor (relative humidity (RH) = 100%), whereas a $T-T_d$ of 30 K indicates that the air would have to be cooled by 30 K for water to condense.

The V_{ex} of HNCO linearly increases as a function of dew point depression with a strong correlation ($r^2 = 0.90$ for binned data; Figure 3.2). This tight correlation is consistent with a dependence on surface wetness. Condensation of water vapor onto cool canopy surfaces and interception of rainfall both cause surface wetness.[34] Ecosystem surface temperatures are generally close to air temperature at night, but slightly cooler due to radiative release of energy, and higher than air temperature when surfaces receive direct sunlight. Since $T-T_d$ follows a diel trend with low nighttime values and high daytime values (Figure 3.2), dew point depression calculated with air temperature captures the dependence of acid exchange on $T-T_d$. High relative humidity causes water to adsorb onto canopy surfaces and form water films and droplets. Even at low RH (<20%), water can adsorb to a variety of surfaces (e.g., mica, metals, metallic oxides, and carbonates) to form submonolayer-to-multilayer films.[35–37] At lower RH, isolated water clusters on surfaces are highly ordered, but films of water molecules cluster more like bulk liquid water at higher RH.[38] Thus, we expect water to condense on canopy surfaces when environmental conditions are near dew point (i.e. low $T-T_d$) – and that these conditions cause net HNCO uptake and negative V_{ex}. During the afternoon, environmental conditions move away

from the dew point (i.e. $T\text{-}T_d$ increases) and aqueous HNCO then partitions out of evaporating wetness, causing HNCO emission and positive V_{ex}. Intriguingly, Figure 3.2 shows an x-axis crossover at high $T\text{-}T_d$ suggesting that even once surface wetness evaporates there may be an emission flux. We hypothesize that surface wetness facilitates organic acid uptake into the leaf/soil matrix, a process that provides a reservoir that enables continued emissions even after surface wetness has fully evaporated, at least for a short period of time (hours to days). For example, studies have observed that solutes diffuse into epistomatal spaces from surface wetness adjacent to leaf stomata.[39–42] If organic acids similarly diffuse from surface wetness into leaf water, we expect leaf water to continue to release organic acids from stomatal pores as part of transpiration flux even after surface wetness evaporates.

Using established metrics for ecosystem surface wetness,[43] we find seasonal variation in wetness. Spring is the wettest season, followed by summer. Despite the lack of precipitation during fall, high RH enabled some wet periods in the fall. In contrast, winter was completely dry. Figure A2.1 shows that correlations between HNCO V_{ex} and dew point depression are strongest in spring ($r^2 = 0.87$) and summer ($r^2 = 0.94$) but disappear completely during winter ($r^2 = 0.01$), consistent with negligible surface wetness as predicted from precipitation data and ambient RH.

To investigate the ubiquity of this surface phenomenon, we compare volatile organic acid fluxes from the dry pine forest of MEFO to a humid continental, mixed canopy forest in Michigan (UMBS)[13] and a Mediterranean-to-semi-arid California orange orchard.[4,44] The same linear relationship between exchange velocity and dew point depression for volatile organic acids occurs at the MEFO pine forest and the UMBS mixed forest, but not the California orange orchard (Figures A2.2-A2.4). Figure 3.3 shows propionic acid as an example of the general trends. Like the MEFO seasonal data, these observations are consistent with observed dew point

depression ranges (Figure A2.5) and predicted ecosystem surface wetness.[43] The California site was consistently dry with no wet periods based on precipitation and RH criteria versus MEFO (31% wet periods) and the UMBS forest (81% wet periods). In situ leaf wetness sensors measured no surface wetness during summer 2010 at the California orchard.

The T-T_d dependence for other acids are consistent with formic acid at the wet sites. The slopes for formic acid exchange velocity versus dew point depression agree for MEFO (0.14 ± 0.01 cm s^{-1} K^{-1}) and UMBS (0.15 ± 0.01 cm s^{-1} K^{-1}) (Table A2.2, Figures A2.2-A2.4). The intercepts do not: -0.4 ± 0.2 cm s^{-1} (MEFO) versus -0.8 ± 0.1 cm s^{-1} (UMBS)

3.4.2 Organic acids in aqueous phase

Partitioning space plots act as phase maps in which water-air equilibrium constants (K_{wa}; Henry's Law) are logarithmically plotted against octanol-air equilibrium constants (K_{oa}). Partitioning space plots have been used to predict phase partitioning for surface films, particles, and clouds,[45–48] and we employ them here to investigate the potential for organic acid uptake and loss from surface wetness. Figure 3.4 assumes three phases are in equilibrium: gas, aqueous film, and water-insoluble organic matter film. The fraction in each phase is:

$$\boldsymbol{Frac_{gas}} = \left(\mathbf{1} + \boldsymbol{K_{oa}} \times \frac{\boldsymbol{V_{org}}}{\boldsymbol{V_{gas}}} + \boldsymbol{K_{wa}} \times \frac{\boldsymbol{V_w}}{\boldsymbol{V_{gas}}}\right)^{-\mathbf{1}} \quad (1)$$

$$\boldsymbol{Frac_{water}} = \left(\mathbf{1} + \frac{\mathbf{1}}{\boldsymbol{K_{wa}} \times \frac{\boldsymbol{V_w}}{\boldsymbol{V_{gas}}}} + \frac{\boldsymbol{K_{oa}}}{\boldsymbol{K_{wa}}} \times \frac{\boldsymbol{V_{org}}}{\boldsymbol{V_w}}\right)^{-\mathbf{1}} \quad (2)$$

$$\boldsymbol{Frac_{organic}} = \left(\mathbf{1} + \frac{\mathbf{1}}{\boldsymbol{K_{oa}} \times \frac{\boldsymbol{V_{org}}}{\boldsymbol{V_{gas}}}} + \frac{\boldsymbol{K_w}}{\boldsymbol{K_{oa}}} \times \frac{\boldsymbol{V_w}}{\boldsymbol{V_{org}}}\right)^{-\mathbf{1}} \quad (3)$$

V represents the volume occupied by the gas phase (V_{gas}), water film (V_w), and organic film (V_{org}). To estimate volumetric phase ratios, we assume films are evenly distributed, and that V_{gas} is much larger than the other phases. We estimate film thicknesses of 50 nm (X_w and X_{org}) and a

surface area to volume ratio of 0.0713 m^{-1}, or the sum of the average fetch area and leaf area divided by the product of the fetch area and measurement height (Section A2.2).

Intrinsic Henry's law constants imply that organic acids are predominantly in the gas phase. However, weak acids additionally partitioning to the aqueous phase as described by effective Henry's law constants (K_{eff}):

$$\boldsymbol{K_{eff} = K_{wa} \times (1 + 10^{pH-pKa})} \quad (4)$$

The pH of dew in forests ranges between 3.2 – 8.2.[49–52] At pH 8.2, ≥20% of the alkanoic acids reside in the aqueous phase, suggesting a mechanism to enhance organic acid deposition to ecosystem wetness. Additional aqueous chemistry or biology could further enhance the K_{eff} and partitioning; for example, microbes digest organic acids in precipitation over the course of months.[53]

Aqueous partitioning depends on film thickness, with more acid uptake occurring over thicker water films. This simple analysis assumes uniform water films, but ecosystem wetness is likely inhomogeneous. Microscopic water films over ecosystem surfaces are typically <1 µm with macroscopic droplets <100 µm,[40] but droplets of 1 mm have been observed.[54] For example, given a 1 µm water film at pH 7, over 90% of formic acid is in the aqueous phase at equilibrium. This dependence of partitioning on film thickness provides a mechanism for the continuum of exchange velocity dependence on dew point depression in Figures 3.2 and 3.3. If surface wetness and the effective ecosystem water film thickness depends linearly on dew point depression ($T-T_d$), then we would predict the observed linear shift from uptake and negative V_{ex} to emission and positive V_{ex} – as long as aqueous reactions are reversible. One open question is how long an ecosystem must dry out before this relationship breaks down (i.e. how many days without surface wetness are needed for MEFO and UMBS to resemble the California orchard?).

This hypothesis of fluxes driven by equilibrium-driven partitioning to the aqueous phase suggests that the slopes (or intercepts) of Figure 3.2 should trend with solubility. However, we find no clear relationships between the observed slopes and solubility or related parameters, reflecting the complexity of additional aqueous reactions and salt formation in ambient water films. Figure 3.3 shows that slope and intercept differences can also manifest for the same compound between sites, potentially due to differences in water film pH or structure (and thickness) of surface wetness on different leaf types.

In contrast to the alkanoic acids, simple weak acid equilibria suggest that HNCO will remain dominantly in the gas phase. However, HNCO hydrolyzes through multiple pathways including reaction with aqueous ammonia[29,55,56] that are not considered by Equation 4 – thus leading to an overestimate of the gas phase fraction. However, some of these reactions are permanent sinks for HNCO and could not lead to equilibrium partitioning back out of surface wetness.

Temperature influences gas-water partitioning. The K_{wa} of HNCO is particularly temperature sensitive.[56] For example, a temperature range of -10 – 30°C implies a range of 21 – 3.0% for the aqueous HNCO fraction (pH 8). Figure A2.6 shows this effect of temperature on HNCO aqueous solubility. While dew point depression does not linearly depend on temperature, there is evidence for a role of temperature in influencing observed concentration and fluxes of organic acids.[14]

3.4.3 Solvation: wet versus dry

Observed gas-phase concentrations of all the volatile acids described herein increased exponentially with temperature at MEFO (Figure A2.7). Calculating observed enthalpies of solvation (ΔH_{obs}) and comparing them with literature values ($\Delta H_{solvation}$) (Figure A2.8) provides

further evidence for the role of gas-water partitioning in controlling biosphere-atmosphere exchange. The van't Hoff equation describes solvation equilibria:

$$\ln(r_g) = \frac{\Delta H_{obs}}{RT} + \{\ln(r_{aq}) - \frac{\Delta S}{R}\} \quad (5)$$

where r_g is volumetric mixing ratio of the acid in the gas phase, R is the universal gas constant (8.314 J mol^{-1} K^{-1}), T is the air temperature (K), r_{aq} is the volumetric mixing ratio of the acid in the aqueous phase, and ΔS is the solvation entropy (J/K). Figure A2.8 plots the natural logarithm of gas phase HNCO mixing ratio against inverse temperature, with the slope providing ΔH_{obs} in kJ mol^{-1}. Wet and dry periods at MEFO yield distinct enthalpies, which we plot against literature values for $\Delta H_{solvation}$ [56,57] in Figure A2.9.Observed enthalpies agree with literature values during dry periods but become more enthalpically favorable during wet periods. This observation is consistent with the hypothesis that under wet conditions, volatile acids may be taken up in the forest by alkaline solutions and/or undergo additional reactions that enhance the solubility of the acid, such as hydrolysis. Under dry conditions, little acid uptake will occur, and instead shrinking water films would force reversible partitioning to the gas phase. Conversely, a modified van't Hoff plot for isoprene, which exhibits temperature and light dependent emissions but is insoluble in water, shows no significant difference between the dry/wet regressions (Figure A2.10) – further supporting our hypothesized role for air-water partitioning in the case of organic acids.

3.5 Conclusions

Phase partitioning between surface wetness and the atmosphere may drive the bi-directional flux of acids between forests and the atmosphere. Water films or droplets can take up molecules, driving downward deposition fluxes, while drying out and shrinking of water films will cause emission of acids. Additional aqueous reactions or changes in pH with wetness may enhance or suppress this partitioning. We hypothesize that dew point depression is a proxy for

surface wetness, but that different plant morphologies and leaf chemistry may influence differences in the slope and intercept at different sites.

HNCO fluxes show strong and significant diel trends, but once averaged over the entire annual dataset, cumulative HNCO fluxes fall within the measurement uncertainty (cumulative flux of +6.6 ppq_v m s^{-1}, average uncertainty for all SPiFFY measurements is ±20 ppq_v m s^{-1} following Finkelstein and Sims.[58] Therefore, we expect the net impact of equilibrium partitioning to and from surface wetness to be small on time scales of one day or more. However, HNCO surface wetness partitioning is likely an important process on shorter time scales. The five alkanoic acids exhibit net annual emission at MEFO, implying a net ecosystem source – either directly to the aqueous phase from plant exudates, or through alternative processes in the gas or aerosol phases that preserve the observed continuum between exchange velocity and dew point depression.

The dependence of exchange velocity on dew point depression appears consistent across sites, so long as adequate leaf wetness is available. We investigated the potential applicability of the relationship in Figure 3.3 to describe organic acid fluxes and found that previously described observations of upward formic acid fluxes at Hyytiälä follow the UMBS relationship, which explains 56% of the variance for diel averages in formic acid flux.

Field and laboratory studies to investigate links between ecosystem wetness, dew point depression, and gas exchange over wet surfaces are essential to understanding atmospheric lifetime not just for weak acids, but also for weak bases and other water-soluble pollutants such as inorganic mercury. Reversible and/or irreversible equilibrium partitioning to surface wetness are known to impact NH_3 and O_3 biosphere-atmosphere exchange. Here, we suggest that surface wetness also impacts organic acid exchange. These observations suggest that ‘dry deposition’ is

not a simple process driven merely by ecosystem surface area. The pH of ecosystem wetness remains unclear but likely influences the exchange of weak acids and bases. Despite being weak acids, organic acids contribute an increasing fraction of precipitation acidity as atmospheric SO_2 and NO_x concentrations decrease.[59] This paper suggests an additional mechanism that mediates atmospheric acid uptake to ecosystem surfaces.

Chapter 3 Figures

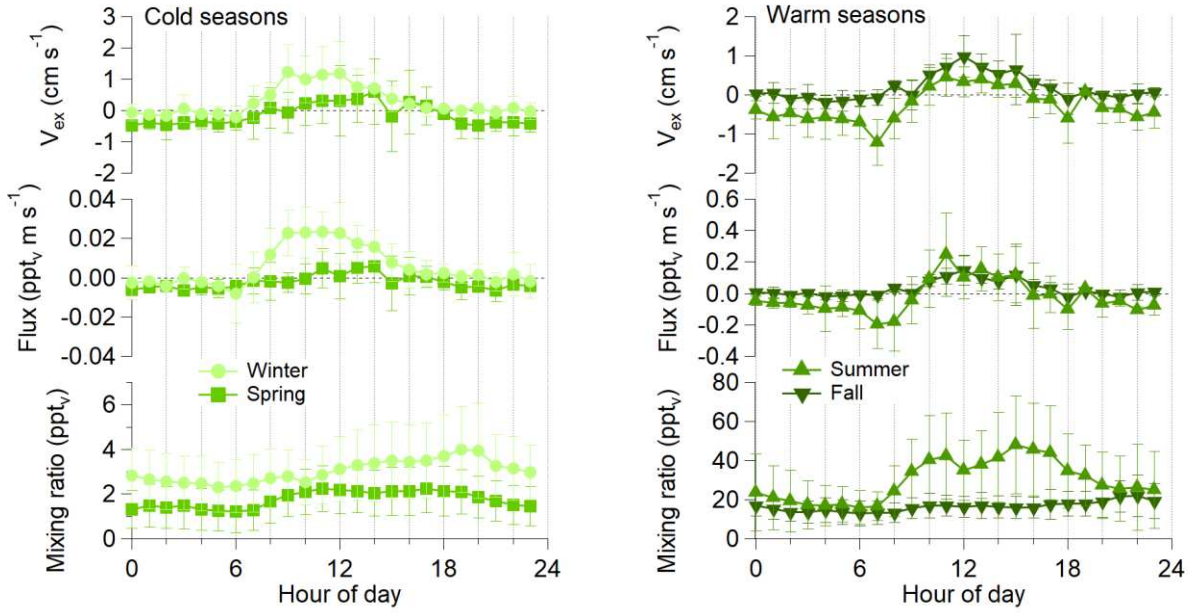

Figure 3.1. Diel time series of HNCO mixing ratio (ppt_v; lower panels), flux (ppt_v m s^{-1}; middle panels), and exchange velocity (cm s^{-1}; upper panels) for each season. Markers represent hourly averages; whiskers are standard deviations.

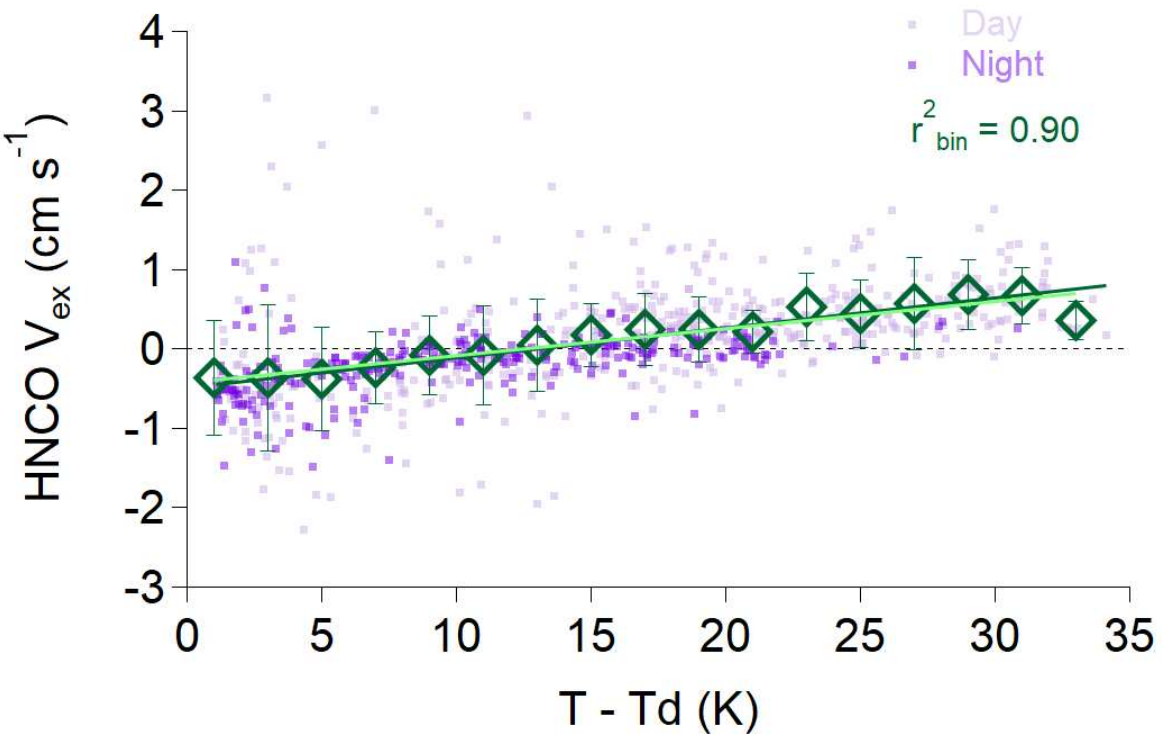

Figure 3.2. The exchange velocity (V_{ex}) of HNCO increases linearly with dew point depression ($T-T_d$). All data from MEFO that met eddy covariance filtering criteria are in dots; dark green, open diamonds show averages of 20 evenly spaced $T-T_d$ bins with corresponding standard deviation. Dots are colored according to incident solar radiation (dark dots <10 nmol photons m^{-2} s^{-1}; light dots ≥10 nmol photons m^{-2} s^{-1}). Least squares linear regression fits the data [$V_{ex}^{bin} = (-0.42 \pm 0.06) + (0.034 \pm 0.003) \times T-T_d$]. The r^2 is 0.25 for all data and 0.90 for the binned data.

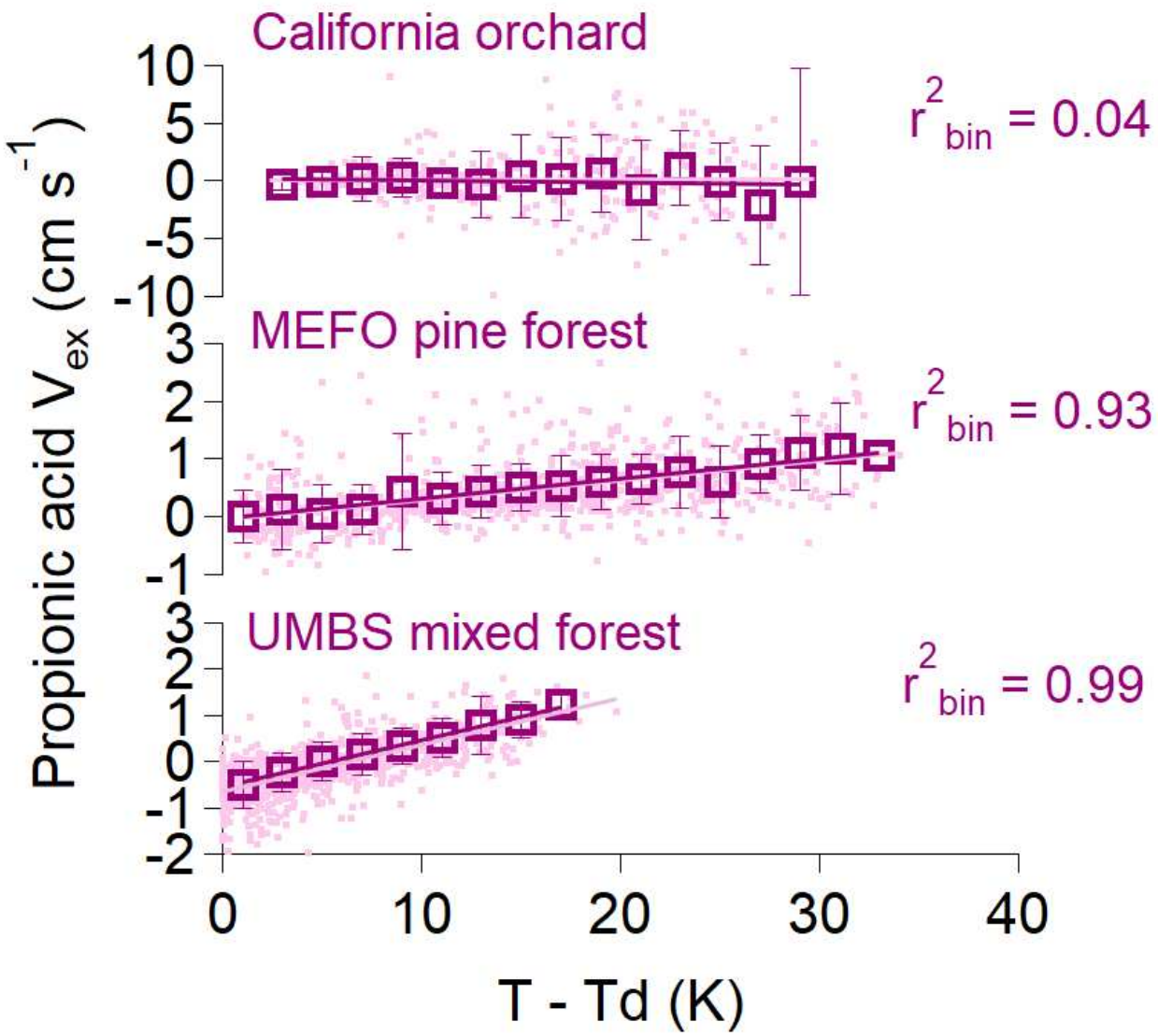

Figure 3.3. Propionic acid exchange velocity (V_{ex}) linearly correlates with dew point depression ($T-T_d$) at the MEFO pine forest and UMBS mixed forest, but not the very dry California orchard. V_{ex} are averaged into 2°C bins for all sites. Fit equations are in Table A2.2. The r^2 (all-data/binned) are 0.00/0.04 for the California orchard, 0.18/0.93 for the MEFO pine forest, and 0.47/0.99 for the UMBS mixed forest.

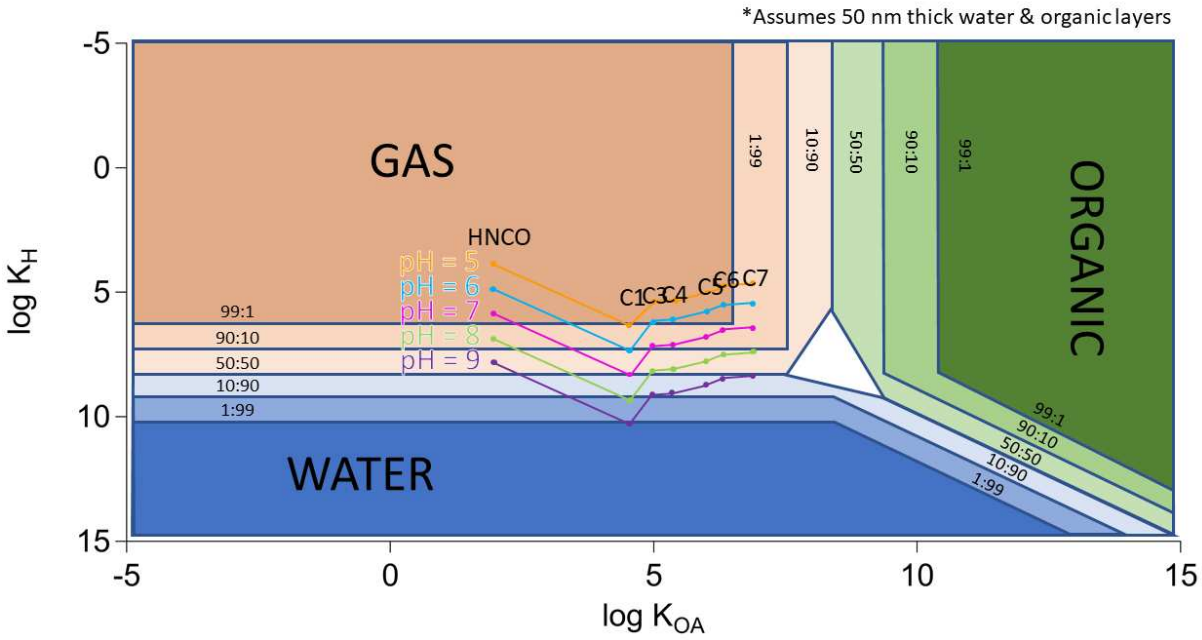

Figure 3.4. Partitioning plots estimate the volatile organic acid phase distribution at MEFO. HNCO and six short-chain alkanoic acids (C1 formic acid, C3 propionic acid, etc.) are highlighted by text markers and predicted to be primarily in the gas phase given the corresponding Henry's law constants (K_H). Accounting for weak-acid equilibria increased partitioning to the aqueous phase with higher pH. pH isopleths are connected to guide the eye. Equilibria are calculated at standard temperature and pressure.

REFERENCES

(1) Gabriel, R.; Schäfer, L.; Gerlach, C.; Rausch, T.; Kesselmeier, J. Factors Controlling the Emissions of Volatile Organic Acids from Leaves of Quercus Ilex L. (Holm Oak). *Atmos. Environ.* **1999**, *33* (9), 1347–1355. https://doi.org/10.1016/S1352-2310(98)00369-0.

(2) Millet, D. B.; Alwe, H. D.; Chen, X.; Deventer, M. J.; Griffis, T. J.; Holzinger, R.; Bertman, S. B.; Rickly, P. S.; Stevens, P. S.; Léonardis, T.; Locoge, N.; Dusanter, S.; Tyndall, G. S.; Alvarez, S. L.; Erickson, M. H.; Flynn, J. H. Bidirectional Ecosystem–Atmosphere Fluxes of Volatile Organic Compounds Across the Mass Spectrum: How Many Matter? *ACS Earth Space Chem.* **2018**, *2* (8), 764–777. https://doi.org/10.1021/acsearthspacechem.8b00061.

(3) Niinemets, Ü.; Fares, S.; Harley, P.; Jardine, K. J. Bidirectional Exchange of Biogenic Volatiles with Vegetation: Emission Sources, Reactions, Breakdown and Deposition. *Plant Cell Environ.* **2014**, *37* (8), 1790–1809. https://doi.org/10.1111/pce.12322.

(4) Park, J.-H.; Goldstein, A. H.; Timkovsky, J.; Fares, S.; Weber, R.; Karlik, J.; Holzinger, R. Active Atmosphere-Ecosystem Exchange of the Vast Majority of Detected Volatile Organic Compounds. *Science* **2013**, *341* (6146), 643–647. https://doi.org/10.1126/science.1235053.

(5) Clifton, O. E.; Fiore, A. M.; Massman, W. J.; Baublitz, C. B.; Coyle, M.; Emberson, L.; Fares, S.; Farmer, D. K.; Gentine, P.; Gerosa, G.; Guenther, A. B.; Helmig, D.; Lombardozzi, D. L.; Munger, J. W.; Patton, E. G.; Pusede, S. E.; Schwede, D. B.; Silva, S. J.; Sörgel, M.; Steiner, A. L.; Tai, A. P. K. Dry Deposition of Ozone Over Land: Processes, Measurement, and Modeling. *Rev. Geophys.* **2020**, *58* (1). https://doi.org/10.1029/2019RG000670.

(6) Knote, C.; Hodzic, A.; Jimenez, J. L. The Effect of Dry and Wet Deposition of Condensable Vapors on Secondary Organic Aerosols Concentrations over the Continental US. *Atmospheric Chem. Phys.* **2015**, *15* (1), 1–18.

(7) Ishibashi, M.; Terashima, I. Effects of Continuous Leaf Wetness on Photosynthesis: Adverse Aspects of Rainfall. *Plant Cell Environ.* **1995**, *18* (4), 431–438. https://doi.org/10.1111/j.1365-3040.1995.tb00377.x.

(8) Hanba, Y. T.; Moriya, A.; Kimura, K. Effect of Leaf Surface Wetness and Wettability on Photosynthesis in Bean and Pea. *Plant Cell Environ.* **2004**, *27* (4), 413–421. https://doi.org/10.1046/j.1365-3040.2004.01154.x.

(9) Misson, L.; Lunden, M.; McKay, M.; Goldstein, A. H. Atmospheric Aerosol Light Scattering and Surface Wetness Influence the Diurnal Pattern of Net Ecosystem Exchange in a Semi-Arid Ponderosa Pine Plantation. *Agric. For. Meteorol.* **2005**, *129* (1), 69–83. https://doi.org/10.1016/j.agrformet.2004.11.008.

(10) Massad, R.-S.; Nemitz, E.; Sutton, M. A. Review and Parameterisation of Bi-Directional Ammonia Exchange between Vegetation and the Atmosphere. *Atmospheric Chem. Phys.* **2010**, *10* (21), 10359–10386. https://doi.org/10.5194/acp-10-10359-2010.

(11) Walker, J. T.; Jones, M. R.; Bash, J. O.; Myles, L.; Meyers, T.; Schwede, D.; Herrick, J.; Nemitz, E.; Robarge, W. Processes of Ammonia Air–Surface Exchange in a Fertilized *Zea Mays* Canopy. *Biogeosciences* **2013**, *10* (2), 981–998. https://doi.org/10.5194/bg-10-981-2013.

(12) Massman, W. J. Toward an Ozone Standard to Protect Vegetation Based on Effective Dose: A Review of Deposition Resistances and a Possible Metric. *Atmos. Environ.* **2004**, *38* (15), 2323–2337. https://doi.org/10.1016/j.atmosenv.2003.09.079.

(13) Alwe, H. D.; Millet, D. B.; Chen, X.; Raff, J. D.; Payne, Z. C.; Fledderman, K. Oxidation of Volatile Organic Compounds as the Major Source of Formic Acid in a Mixed Forest Canopy. *Geophys. Res. Lett.* **2019**, *46* (5), 2940–2948. https://doi.org/10.1029/2018GL081526.

(14) Fulgham, S. R.; Brophy, P.; Link, M.; Ortega, J.; Pollack, I.; Farmer, D. K. Seasonal Flux Measurements over a Colorado Pine Forest Demonstrate a Persistent Source of Organic Acids. *ACS Earth Space Chem.* **2019**. https://doi.org/10.1021/acsearthspacechem.9b00182.

(15) Nguyen, T. B.; Crounse, J. D.; Teng, A. P.; Clair, J. M. S.; Paulot, F.; Wolfe, G. M.; Wennberg, P. O. Rapid Deposition of Oxidized Biogenic Compounds to a Temperate Forest. *Proc. Natl. Acad. Sci.* **2015**, *112* (5), E392–E401. https://doi.org/10.1073/pnas.1418702112.

(16) Schobesberger, S.; Lopez-Hilfiker, F. D.; Taipale, D.; Millet, D. B.; D'Ambro, E. L.; Rantala, P.; Mammarella, I.; Zhou, P.; Wolfe, G. M.; Lee, B. H.; Boy, M.; Thornton, J. A. High Upward Fluxes of Formic Acid from a Boreal Forest Canopy. *Geophys. Res. Lett.* **2016**, 2016GL069599. https://doi.org/10.1002/2016GL069599.

(17) Karl, T.; Kaser, L.; Turnipseed, A. Eddy Covariance Measurements of Isoprene and 232-MBO Based on NO+ Time-of-Flight Mass Spectrometry. *Int. J. Mass Spectrom.* **2014**, *365* (Supplement C), 15–19. https://doi.org/10.1016/j.ijms.2013.12.002.

(18) Kaser, L.; Karl, T.; Guenther, A.; Graus, M.; Schnitzhofer, R.; Turnipseed, A.; Fischer, L.; Harley, P.; Madronich, M.; Gochis, D.; Keutsch, F. N.; Hansel, A. Undisturbed and Disturbed above Canopy Ponderosa Pine Emissions: PTR-TOF-MS Measurements and MEGAN 2.1 Model Results. *Atmospheric Chem. Phys.* **2013**, *13* (23), 11935–11947. https://doi.org/10.5194/acp-13-11935-2013.

(19) Ortega, J.; Turnipseed, A.; Guenther, A. B.; Karl, T. G.; Day, D. A.; Gochis, D.; Huffman, J. A.; Prenni, A. J.; Levin, E. J. T.; Kreidenweis, S. M.; DeMott, P. J.; Tobo, Y.; Patton, E. G.; Hodzic, A.; Cui, Y. Y.; Harley, P. C.; Hornbrook, R. S.; Apel, E. C.; Monson, R. K.; Eller, A. S. D.; Greenberg, J. P.; Barth, M. C.; Campuzano-Jost, P.; Palm, B. B.; Jimenez, J.

L.; Aiken, A. C.; Dubey, M. K.; Geron, C.; Offenberg, J.; Ryan, M. G.; Fornwalt, P. J.; Pryor, S. C.; Keutsch, F. N.; DiGangi, J. P.; Chan, A. W. H.; Goldstein, A. H.; Wolfe, G. M.; Kim, S.; Kaser, L.; Schnitzhofer, R.; Hansel, A.; Cantrell, C. A.; Mauldin, R. L.; Smith, J. N. Overview of the Manitou Experimental Forest Observatory: Site Description and Selected Science Results from 2008 to 2013. *Atmos Chem Phys* **2014**, *14* (12), 6345–6367. https://doi.org/10.5194/acp-14-6345-2014.

(20) Pryor, S. C.; Barthelmie, R. J.; Hornsby, K. E. Size-Resolved Particle Fluxes and Vertical Gradients over and in a Sparse Pine Forest. *Aerosol Sci. Technol.* **2013**, *47* (11), 1248–1257. https://doi.org/10.1080/02786826.2013.831974.

(21) Rhew, R. C.; Deventer, M. J.; Turnipseed, A. A.; Warneke, C.; Ortega, J.; Shen, S.; Martinez, L.; Koss, A.; Lerner, B. M.; Gilman, J. B.; Smith, J. N.; Guenther, A. B.; de Gouw, J. A. Ethene, Propene, Butene and Isoprene Emissions from a Ponderosa Pine Forest Measured by Relaxed Eddy Accumulation. *Atmos Chem Phys Discuss* **2017**, *2017*, 1–35. https://doi.org/10.5194/acp-2017-363.

(22) Link, M. F.; Friedman, B.; Fulgham, R.; Brophy, P.; Galang, A.; Jathar, S. H.; Veres, P.; Roberts, J. M.; Farmer, D. K. Photochemical Processing of Diesel Fuel Emissions as a Large Secondary Source of Isocyanic Acid (HNCO). *Geophys. Res. Lett.* **2016**, *43* (8), 2016GL068207. https://doi.org/10.1002/2016GL068207.

(23) Mattila, J. M.; Brophy, P.; Kirkland, J.; Hall, S.; Ullmann, K.; Fischer, E. V.; Brown, S.; McDuffie, E.; Tevlin, A.; Farmer, D. K. Tropospheric Sources and Sinks of Gas-Phase Acids in the Colorado Front Range. *Atmospheric Chem. Phys.* **2018**, *18* (16), 12315–12327. https://doi.org/10.5194/acp-18-12315-2018.

(24) Roberts, J. M.; Veres, P. R.; Cochran, A. K.; Warneke, C.; Burling, I. R.; Yokelson, R. J.; Lerner, B.; Gilman, J. B.; Kuster, W. C.; Fall, R.; Gouw, J. de. Isocyanic Acid in the Atmosphere and Its Possible Link to Smoke-Related Health Effects. *Proc. Natl. Acad. Sci.* **2011**, *108* (22), 8966–8971. https://doi.org/10.1073/pnas.1103352108.

(25) Jathar, S. H.; Heppding, C.; Link, M. F.; Farmer, D. K.; Akherati, A.; Kleeman, M. J.; Gouw, J. A. de; Veres, P. R.; Roberts, J. M. Investigating Diesel Engines as an Atmospheric Source of Isocyanic Acid in Urban Areas. *Atmospheric Chem. Phys.* **2017**, *17* (14), 8959–8970. https://doi.org/10.5194/acp-17-8959-2017.

(26) Roberts, J. M.; Veres, P. R.; VandenBoer, T. C.; Warneke, C.; Graus, M.; Williams, E. J.; Lefer, B.; Brock, C. A.; Bahreini, R.; Öztürk, F.; Middlebrook, A. M.; Wagner, N. L.; Dubé, W. P.; de Gouw, J. A. New Insights into Atmospheric Sources and Sinks of Isocyanic Acid, HNCO, from Recent Urban and Regional Observations. *J. Geophys. Res. Atmospheres* **2014**, *119* (2), 2013JD019931. https://doi.org/10.1002/2013JD019931.

(27) Barnes, I.; Solignac, G.; Mellouki, A.; Becker, K. H. Aspects of the Atmospheric Chemistry of Amides. *ChemPhysChem* **2010**, *11* (18), 3844–3857. https://doi.org/10.1002/cphc.201000374.

(28) Young, Paul. J.; Emmons, L. K.; Roberts, J. M.; Lamarque, J.-F.; Wiedinmyer, C.; Veres, P.; VandenBoer, T. C. Isocyanic Acid in a Global Chemistry Transport Model: Tropospheric Distribution, Budget, and Identification of Regions with Potential Health Impacts. *J. Geophys. Res. Atmospheres* **2012**, *117* (D10), D10308. https://doi.org/10.1029/2011JD017393.

(29) Leslie, M. D.; Ridoli, M.; Murphy, J. G.; Borduas-Dedekind, N. Isocyanic Acid (HNCO) and Its Fate in the Atmosphere: A Review. *Environ. Sci. Process. Impacts* **2019**. https://doi.org/10.1039/C9EM00003H.

(30) Ge, X.; Wexler, A. S.; Clegg, S. L. Atmospheric Amines – Part I. A Review. *Atmos. Environ.* **2011**, *45* (3), 524–546. https://doi.org/10.1016/j.atmosenv.2010.10.012.

(31) Sipilä, M.; Sarnela, N.; Jokinen, T.; Junninen, H.; Hakala, J.; Rissanen, M. P.; Praplan, A.; Simon, M.; Kürten, A.; Bianchi, F.; Dommen, J.; Curtius, J.; Petäjä, T.; Worsnop, D. R. Bisulfate – Cluster Based Atmospheric Pressure Chemical Ionization Mass Spectrometer for High-Sensitivity (< 100 PpqV) Detection of Atmospheric Dimethyl Amine: Proof-of-Concept and First Ambient Data from Boreal Forest. *Atmospheric Meas. Tech.* **2015**, *8* (10), 4001–4011. https://doi.org/10.5194/amt-8-4001-2015.

(32) VandenBoer, T. C.; Petroff, A.; Markovic, M. Z.; Murphy, J. G. Size Distribution of Alkyl Amines in Continental Particulate Matter and Their Online Detection in the Gas and Particle Phase. *Atmospheric Chem. Phys.* **2011**, *11* (9), 4319–4332. https://doi.org/10.5194/acp-11-4319-2011.

(33) Hrdina, A.; Moravek, A.; Schwartz-Narbonne, H.; Murphy, J. Summertime Soil-Atmosphere Ammonia Exchange in the Colorado Rocky Mountain Front Range Pine Forest. *Soil Syst.* **2019**, *3* (1), 15. https://doi.org/10.3390/soilsystems3010015.

(34) Monteith, J. L. Dew. *Q. J. R. Meteorol. Soc.* **1957**, *83* (357), 322–341. https://doi.org/10.1002/qj.49708335706.

(35) Ewing, G. E. Ambient Thin Film Water on Insulator Surfaces. *Chem. Rev.* **2006**, *106* (4), 1511–1526. https://doi.org/10.1021/cr040369x.

(36) Freund, J.; Halbritter, J.; Hörber, J. K. H. How Dry Are Dried Samples? Water Adsorption Measured by STM. *Microsc. Res. Tech.* **1999**, *44* (5), 327–338. https://doi.org/10.1002/(SICI)1097-0029(19990301)44:5<327::AID-JEMT3>3.0.CO;2-E.

(37) Verdaguer, A.; Sacha, G. M.; Bluhm, H.; Salmeron, M. Molecular Structure of Water at Interfaces: Wetting at the Nanometer Scale. *Chem. Rev.* **2006**, *106* (4), 1478–1510. https://doi.org/10.1021/cr040376l.

(38) Rubasinghege, G.; Grassian, V. H. Role(s) of Adsorbed Water in the Surface Chemistry of Environmental Interfaces. *Chem. Commun.* **2013**, *49* (30), 3071–3094. https://doi.org/10.1039/C3CC38872G.

(39) Burkhardt, J.; Basi, S.; Pariyar, S.; Hunsche, M. Stomatal Penetration by Aqueous Solutions – an Update Involving Leaf Surface Particles. *New Phytol.* **2012**, *196* (3), 774–787. https://doi.org/10.1111/j.1469-8137.2012.04307.x.

(40) Burkhardt, J.; Hunsche, M. "Breath Figures" on Leaf Surfaces—Formation and Effects of Microscopic Leaf Wetness. *Front. Plant Sci.* **2013**, *4*. https://doi.org/10.3389/fpls.2013.00422.

(41) Eichert, T.; Kurtz, A.; Steiner, U.; Goldbach, H. E. Size Exclusion Limits and Lateral Heterogeneity of the Stomatal Foliar Uptake Pathway for Aqueous Solutes and Water-Suspended Nanoparticles. *Physiol. Plant.* **2008**, *134* (1), 151–160. https://doi.org/10.1111/j.1399-3054.2008.01135.x.

(42) Fernández, V.; Eichert, T. Uptake of Hydrophilic Solutes Through Plant Leaves: Current State of Knowledge and Perspectives of Foliar Fertilization. *Crit. Rev. Plant Sci.* **2009**, *28* (1–2), 36–68. https://doi.org/10.1080/07352680902743069.

(43) Altimir, N.; Kolari, P.; Tuovinen, J.-P.; Vesala, T.; Bäck, J.; Suni, T.; Kulmala, M.; Hari, P. Foliage Surface Ozone Deposition: A Role for Surface Moisture? *Biogeosciences* **2006**, *3* (2), 209–228. https://doi.org/10.5194/bg-3-209-2006.

(44) Fares, S.; Park, J.-H.; Gentner, D. R.; Weber, R.; Ormeño, E.; Karlik, J.; Goldstein, A. H. Seasonal Cycles of Biogenic Volatile Organic Compound Fluxes and Concentrations in a California Citrus Orchard. *Atmos Chem Phys* **2012**, *12* (20), 9865–9880. https://doi.org/10.5194/acp-12-9865-2012.

(45) Lei, Y. D.; Wania, F. Is Rain or Snow a More Efficient Scavenger of Organic Chemicals? *Atmos. Environ.* **2004**, *38* (22), 3557–3571. https://doi.org/10.1016/j.atmosenv.2004.03.039.

(46) Wang, C.; Goss, K.-U.; Lei, Y. D.; Abbatt, J. P. D.; Wania, F. Calculating Equilibrium Phase Distribution during the Formation of Secondary Organic Aerosol Using COSMOtherm. *Environ. Sci. Technol.* **2015**, *49* (14), 8585–8594. https://doi.org/10.1021/acs.est.5b01584.

(47) Wang, C.; Collins, D. B.; Arata, C.; Goldstein, A. H.; Mattila, J. M.; Farmer, D. K.; Ampollini, L.; DeCarlo, P. F.; Novoselac, A.; Vance, M. E.; Nazaroff, W. W.; Abbatt, J. P. D.

Surface Reservoirs Dominate Dynamic Gas-Surface Partitioning of Many Indoor Air Constituents. *Sci. Adv.* **2020**, *6* (8), eaay8973. https://doi.org/10.1126/sciadv.aay8973.

(48) Wania, F.; Lei, Y. D.; Wang, C.; Abbatt, J. P. D.; Goss, K.-U. Using the Chemical Equilibrium Partitioning Space to Explore Factors Influencing the Phase Distribution of Compounds Involved in Secondary Organic Aerosol Formation. *Atmospheric Chem. Phys.* **2015**, *15* (6), 3395–3412. https://doi.org/10.5194/acp-15-3395-2015.

(49) Okochi, H.; Kajimoto, T.; Arai, Y.; Igawa, M. Effect of Acid Deposition on Urban Dew Chemistry in Yokohama, Japan. *Bull. Chem. Soc. Jpn.* **1996**, *69* (11), 3355–3365. https://doi.org/10.1246/bcsj.69.3355.

(50) Polkowska, Ż.; Błaś, M.; Klimaszewska, K.; Sobik, M.; Małek, S.; Namieśnik, J. Chemical Characterization of Dew Water Collected in Different Geographic Regions of Poland. *Sensors* **2008**, *8* (6), 4006–4032. https://doi.org/10.3390/s8064006.

(51) Richards, K. Observation and Simulation of Dew in Rural and Urban Environments. *Prog. Phys. Geogr. Earth Environ.* **2004**, *28* (1), 76–94. https://doi.org/10.1191/0309133304pp402ra.

(52) Wentworth, G. R.; Murphy, J. G.; Benedict, K. B.; Bangs, E. J.; Collett Jr., J. L. The Role of Dew as a Night-Time Reservoir and Morning Source for Atmospheric Ammonia. *Atmospheric Chem. Phys.* **2016**, *16* (11), 7435–7449. https://doi.org/10.5194/acp-16-7435-2016.

(53) Keene, W. C.; Galloway, J. N. Organic Acidity in Precipitation of North America. *Atmospheric Environ. 1967* **1984**, *18* (11), 2491–2497. https://doi.org/10.1016/0004-6981(84)90020-9.

(54) Hughes, R. N.; Brimblecombe, P. Dew and Guttation: Formation and Environmental Significance. *Agric. For. Meteorol.* **1994**, *67* (3), 173–190. https://doi.org/10.1016/0168-1923(94)90002-7.

(55) Borduas, N.; Place, B.; Wentworth, G. R.; Abbatt, J. P. D.; Murphy, J. G. Solubility and Reactivity of HNCO in Water: Insights into HNCO's Fate in the Atmosphere. *Atmospheric Chem. Phys.* **2016**, *16* (2), 703–714. https://doi.org/10.5194/acp-16-703-2016.

(56) Roberts, J. M.; Liu, Y. Solubility and Solution-Phase Chemistry of Isocyanic Acid, Methyl Isocyanate, and Cyanogen Halides. *Atmospheric Chem. Phys.* **2019**, *19* (7), 4419–4437. https://doi.org/10.5194/acp-19-4419-2019.

(57) Sander, R. Compilation of Henry's Law Constants (Version 4.0) for Water as Solvent. *Atmospheric Chem. Phys.* **2015**, *15* (8).

(58) Finkelstein, P. L.; Sims, P. F. Sampling Error in Eddy Correlation Flux Measurements. *J. Geophys. Res. Atmospheres* **2001**, *106* (D4), 3503–3509. https://doi.org/10.1029/2000JD900731.

(59) Vet, R.; Artz, R. S.; Carou, S.; Shaw, M.; Ro, C.-U.; Aas, W.; Baker, A.; Bowersox, V. C.; Dentener, F.; Galy-Lacaux, C.; Hou, A.; Pienaar, J. J.; Gillett, R.; Forti, M. C.; Gromov, S.; Hara, H.; Khodzher, T.; Mahowald, N. M.; Nickovic, S.; Rao, P. S. P.; Reid, N. W. A Global Assessment of Precipitation Chemistry and Deposition of Sulfur, Nitrogen, Sea Salt, Base Cations, Organic Acids, Acidity and PH, and Phosphorus. *Atmos. Environ.* **2014**, *93*, 3–100. https://doi.org/10.1016/j.atmosenv.2013.10.060.

CHAPTER 4

RAPID PRODUCTION OF GASEOUS NITRATED PHENOLS FROM PRESCRIBED BURNING OF PONDEROSA PINE FOREST

4.1 Introduction

Globally, biomass burning is a major source of particles and trace gases to the atmosphere.[1,2] Many of the emitted gases are air toxics, criteria pollutants, or organic precursors that form hazardous gases and aerosols as smoke plumes age during atmospheric transport.[3] Biomass burning directly and indirectly produces greenhouse gases and particulate matter, which impact climate.[4,5] In North America, burning of temperate and boreal forests accounts for the largest fraction of fire carbon emissions.[6] Although wildfires are reducing in number overall, large wildfires in the United States occur more frequently.[7,8] Prescribed fires have become a critical forest management strategy to reduce hazardous fuel loads, particularly near populated area. Of the 668 million ha of forests and rangelands in the U.S., forest managers conducted controlled burns on 4.42 million ha in 2014.[8]

To standardize measurements of fire emissions, substantial effort has been made to build inventories of emission factors (EFs) and/or emission ratios (ERs).[9–12] EFs contextualize emissions in terms of the mass of fuel consumed. ERs employ one of a number of chemical tracers to characterize fire emissions. Tracers, such as CO, CO_2, or C_2H_3N, typically account for both rapid dilution of smoke plumes and a large fraction of the chemistry producing trace gases and particles. Both EFs and ERs are representative of direct fire emissions with minimal atmospheric aging.[1] However, few comprehensive, near-field measurements of volatile and semi-volatile organic compounds (VOCs, SVOCs) are available due to inherent challenges of deploying instrumentation near a fire. The lack of VOC and SVOC field measurements from

fresh smoke contributes to ambiguity in distinguishing between primary and secondary biomass burning chemistry.

Using environmentally representative fire emissions inventories coupled to various empirical parameterizations, model predictions are highly variable and uncertain.[13] Furthermore, VOC and SVOC fire emissions strongly depend upon type and quantity of fuel loadings as well as fire traits,[11] which are rarely incorporated into the models. Recently, positive matrix factorization analyses of VOCs, SVOCs, and reactive nitrogen compounds, measured during FIREX at the Fire Sciences Laboratory in Missoula, Montana, revealed strong dependence of product distribution upon the temperature regime of the fire.[14,15] However, many important SVOCs, such as large or functionalized acids and nitrated phenols, were not included in these analyses.

Fires pyrolyze lignin and other biopolymers and produce reactive phenolic compounds, a class of SVOCs, ubiquitously and in large quantities.[8,15] Functionalized phenols, including catechol and guaiacol, are thought to constitute a significant fraction of primary organic aerosol, formed by aqueous-phase reactions.[16] Many are directly toxic to human health.[17] Nitrated phenols became the focus of several studies following their identification as phytoxins.[18] More recently, nitrated phenols have been shown to absorb as much as 29% of UV light absorbed by particulate brown carbon from anthropogenic wood burning, a disproportionately large amount for <1% of organic aerosol mass.[19] Phenolic nitration is thought to proceed in three steps: proton abstraction by hydroxyl radical (OH), radical rearrangement, and addition of NO_2. Nitrated phenols are relatively long-lived with respect to OH ($\tau_{nitrophenol} \sim 34$ d, $\tau_{catechol} \sim 42$ h).[20] Greater oxygenation makes nitrated phenols less volatile than phenolic precursors and therefore favors partitioning to the particle phase. As a result, in situ measurements in the gas phase are

analytically challenging and seldom reported but could disambiguate primary and secondary formation processes.

In this work, we measured gaseous SVOCs, including organic acids, phenols, nitrated phenols, and other nitrogen-containing compounds, in fresh smoke from the prescribed burning of a Rocky Mountain ponderosa pine forest in central Colorado, United States. We calculated ERs (ppb ppb^{-1}CO) for comparison with literature values and to augment existing emissions inventories. We identified two fire temperature modes, with significantly different quantities of emissions, that provide new understanding of the time scale and extent of biomass burning chemistry.

4.2 Materials and Methods

4.2.1 Site and prescribed burn

Manitou Experimental Forest is a montane, 6760 ha ponderosa pine forest in central Colorado, which has been described and characterized in great detail.[21] Several wildfires, including the Hayman and Waldo Canyon Fires, have burned portions of the forest since 2002. To mitigate wildfire danger and to promote ecosystem health, the U.S. Forest Service (USFS) conducts prescribed burns, including two forest parcels (P4 and P6) totaling 136 ha on 10 October 2016 (Figure 4.1). USFS previously burned P6 in 2007. No previous burns of P4 were on record at the time of the burn. At ~11:00 MDT, ignition began at the northernmost point of P6. We observed tall flames, approximately of canopy height, as the forest ignited. A thick column of smoke replaced the flames, with a footprint approximately the area of the two burn

parcels. Small fires ignited within the burn area intermittently creating small plumes of smoke for the next 2-3 days.

The forest canopy of the burn parcels was sparse (leaf area index (LAI) = 1.14) and primarily consisted of ponderosa pine trees (*Pinus ponderosa*). USFS measured an average surface fuel loading of 4.1 tons $acre^{-1}$ in nearby Rocky Mountain ponderosa pine forest with fuel classes ranging from 0 – 21.1 tons $acre^{-1}$.[22] Surface fuels included fallen trees and branches, duff (0-1.3 cm), litter (0-10 cm), and understory herbaceous plants.[23] Previous laboratory reports of ponderosa pine combustion found elemental composition of 51.1% carbon, 6.6% hydrogen, 1.1% nitrogen, and N:C ratio of 0.022.[7,15]

4.2.2 Measurements and inlet locations

Table 4.1 lists the instrumentation used for all measurements, acquisition times, and inlet heights. Brief descriptions of the instruments are provided here. A Particle Size Distribution (PSD) instrument and Ultra High Sensitivity Aerosol Spectrometer (UHSAS) counted and sized particulate matter during the fire. The PSD is a combination of two Scanning Mobility Particle Sizers collectively spanning particle diameters 4-300 nm.[21,24] Particles in sample air were ionized by a sealed ^{210}Po ion source and size-selected by separate Differential Mobility Analyzers, which oscillated between 0-8000 V over 280 s cycles with 20 s idle time between scans. Condensation Particle Counters (TSI 3025 and 3760) detected the monodisperse particles. The UHSAS bombarded particles in a sample air stream with light from a semiconductor-diode-pumped Nd^{3+}:$YLiF_4$ solid state laser and measured the light scattered by sampled particles with a two detector system.[25] The tight correlation between incident light wavelength and particle diameter was used to determine particle size. A Thermo Scientific NO_x analyzer (Model 42i-TL), configured to NO-only mode, measured nitric oxide by NO-O_3 chemiluminescence. A 395 nm

LED array was coupled to the NO_x analyzer and converted NO_2 to NO by ultraviolet photolysis. Acetate Chemical Ionization Mass Spectrometry (acetate CIMS) ionized gaseous acids and phenolic compounds by proton transfer with acetate ions, separated ions by mass-to-charge ratio in a time-of-flight vacuum chamber, and detected ions with a multi-channel plate. Operating parameters and automated acid calibrations for the acetate CIMS were previously described.[26]

Manitou Experimental Forest Observatory (MEFO) is located 1 km south southeast of the approximate centroid of the burn area (Figure 4.1). Measurements were acquired from two sites, separated by ~15 m: a tower site (39.1013 N, -105.1035 W) and a ground site (Figure 4.2). Inlet separation is discussed in Section 4.3.3.

4.2.3 Acetate CIMS calibrations

To quantify various organics and nitrogen-containing compounds with acetate CIMS, we employed bulk calibration techniques based on each assigned molecular formula's oxidation state and number of carbon atoms.[27] The data workflow was as follows. CIMS time series were averaged to 1 s time resolution. Signals were normalized by reagent ion counts ($C_2H_3O_2^-$) to account for variability in ionization chemistry and multiplied by total ion counts. Time series were background subtracted, and calibration periods were removed. Carboxylic acid formulae were further filtered and categorized according to criteria established by Liu et al.[27]

Due to aromatic stabilization of the negative charge on the deprotonated oxygen atom, phenolic compounds behave as very weak acids. We assumed phenol ionization proceeds by the donation of a proton from a phenolic compound's hydroxyl group to acetate reagent ion. Table 4.2 lists gas phase acidities ($\Delta G°$ of gas phase deprotonation) of measured phenols where

available. We note that for acetate CIMS detection, the gas phase acidity of the analyte must be greater than that of acetate (-1427 ± 8 kJ mol^{-1}).[28]

Using oxidation state (*OSc*) and number of carbon atoms (*nC*), we calculated calibration factors (c_f) for qualifying formulae by Eq. 1, which Link[29] determined by multiple linear regression.

$$\log_{10}(c_f) = (0.205\ x\ OSc) + (0.135\ x\ nC) + 0.511 \quad (1)$$

Normalized, background subtracted, high-resolution ion signals were divided by corresponding sensitivities to calculate mixing ratios as parts per trillion by volume (ppt) and parts per billion by volume (ppb). Of these quantified compounds, we assigned names to 44, which we categorized as acids (12 compounds), phenols (6 compounds), nitrated phenols (10 compounds), and other nitrogen-containing compounds (16 compounds).

4.2.4 Lab calibrations

To ensure detection of phenolic compounds, we measured standards of 1,2-benzenediol ($C_6H_6O_2$), 4-nitro-1,2-benzenediol ($C_6H_5NO_4$), 2-methoxyphenol ($C_7H_8O_2$), 4-nitro-2-methoxyphenol ($C_7H_7NO_4$), 4-nitrophenol ($C_6H_5NO_3$), 4-methyl-1,2-benzenediol ($C_7H_8O_2$), 3-methyl-1,2-benzenediol ($C_7H_8O_2$), phenol (C_6H_6O), o-, m-, and p-cresol (C_7H_8O), and coniferyl aldehyde ($C_{10}H_{10}O_3$) using a heated injection system coupled to acetate CIMS.[30] Ten μL of dilute (44 – 94 μM) solutions in acetone were injected into a stream of ultra zero grade air heated to 250°C flowing at 1.9 L min^{-1}. A small strip of filter paper collected injected solutions to allow for volatilization in the heated air stream. Injections were repeated in triplicate. The instrument responded at the m/Z of the molecular ion significantly above background for each standard except for 2-methoxyphenol, or guaiacol. The gas phase acidity of guaiacol is -1433 ± 8 kJ mol^{-1}, less than that of acetic acid, but also within uncertainty. We attribute lack of sensitivity to

guaiacol to the relative unfavorability of its proton exchange with acetate. Unlike guaiacol, acetate CIMS shows strong response to injections of 4-methyl-1,2-benzenediol at the same nominal m/Z.

4.2.5 Calculation of Emission Ratios (ER)

ERs are often used to standardize measurements enhanced by fire emissions to an atmospheric tracer, which is both prominent in fire emissions and long-lived in the atmosphere. Carbon monoxide (CO) is a commonly used biomass burning tracer for volatile organic compounds.[11,15] CO reacts slowly with atmospheric oxidants and an end product of volatile organic compound oxidation in the gas phase. Therefore, normalization of excess mixing ratios (ΔX, X-X_{bkg}) to excess CO (ΔCO, CO-CO_{bkg}) accounts for dilution of smoke plumes and approximates the fraction of total fire output for the analyte (X) (Eq. 2).

$$NEMR = \frac{\Delta X}{\Delta CO} = \frac{X - X_{bkg}}{CO - CO_{bkg}} \quad (2)$$

We calculated ERs using a slope method. Acid or phenol mixing ratios were scattered against CO and fit with a linear orthogonal distance regression. The slope of the best-fit line is the ER (ppb ppb^{-1}CO). Because ERs are dilution-corrected and local sources are insignificant relative to fire emissions, changes in the ER over time are indicative of changes in fire chemistry.

4.3. Results and Discussion

4.3.1 Plume transport

Westerly-to-northerly winds carried smoke plumes from the prescribed burn area to MEFO at daytime-averaged rate of 3.5 m s^{-1} (Figure 4.3). Conservatively assuming a distance of ~1 km between MEFO and the centroid of the fire, we estimate the physical age of the measured

burn plumes as ~5 min. To our knowledge, measurements of gaseous nitrated phenols in very fresh smoke have not been reported.

Using the Hybrid Single Particle Langrangian Integrated Trajectory (HYSPLIT) model, we estimated 3-hour forward trajectories of burn plumes once every hour between 12:00 – 6:00 PM, 10 October 2016 (Figure 4.4). Plumes originated from 39.1086°N, 105.1069°W, near the centroid of the fire. Global Data Assimilation System (GDAS) model estimated meteorology at 0.5° spatial resolution. Plumes traveled east over the Rocky Mountain foothills before passing over the suburban communities of Palmer Lake, Monument, Woodmoor, and Gleneagle, Colorado (population >20,000).

4.3.2 Mixing ratios by category

To our knowledge, we report the first gas-phase measurements of nitrated phenols from very fresh fire emissions (<5 min in age). Near-field fire measurements reduce ambiguity between primary and secondary source apportioning of fire emissions by minimizing time for secondary reactions to occur. The most reactive phenols ($k_{OH} = 1.0\times10^{-10}$ cm^3 $molec^{-1}$ s^{-1}) are depleted within minutes of exposure to elevated OH concentrations in smoke plumes (OH = 1.5×10^7 molec cm^{-3}).[31,32]

Emissions from the prescribed burn reached MEFO at ~12:50 PM Mountain Daylight Time (Figure 4.5). Acids accounted for nearly half of acetate CIMS measurements, phenols and other nitrogen-containing compounds made up another ¼ each, and trace amounts were attributable to nitrated phenols. However, nitrated phenols reached concentrations exceeding 1 ppb, greater than concentrations measured in polluted urban sites in China and Italy and from domestic burning in an English village, but on par with bonfire emissions in Manchester, UK.[18,19,33,34] Formic acid made up the largest fraction of acids (34.6%) with significant

contributions from glycolic (11.3%), pyruvic (9.9%), lactic (9.3%), and acrylic acids (5.4%). The fire emission-enhanced acid distribution changed dramatically since >80% of background acid measurements were attributable to formic acid. Observed mixing ratios for glycolic, pyruvic, and lactic acids (>20 ppb each) are significantly large, particularly for pyruvic acid, which predominates in the particle phase. Greater than half of the phenols were attributable to coniferyl aldehyde (58.2%) followed by benzenediol (28.6%) and methylbenzendiol (8.9%). Nitrated phenol mixing ratios were more evenly distributed than other categories. Nitrophenol (36.7%) accounted for the largest fraction with dimethylnitrophenol (9.3%), nitrobenzenediol (10.6%), nitromethylphenol (17.2%), and nitromethylbenzenediol (20.2%) making up the rest. Other nitrogen-containing compounds primarily consisted of isocyanic acid (HNCO).

4.3.3 Inlet separation

Cross-sections of smoke plumes sampled by different inlets at the tower and ground sites must be well-mixed for measurement comparisons to be representative of the same combustion and aging processes. To test plume homogeneity at different inlets, we compare particle measurements from the tower and ground sites. The UHSAS and PSD inlets were horizontally separated by ~15 m and vertically by 20 m. Measurement averaging times were 1 s and 300 s, respectively. Mass concentration time series trend strongly between instruments and peak at >100 $\mu g\ m^{-3}$ (Figure 4.6). Particle number concentrations 60-300 nm showed excellent agreement below 3000 particles cm^{-3}. Above this threshold, the UHSAS detectors saturated and underestimated number concentrations substantially (Figure 4.6 inset). UHSAS detector saturation at high number concentrations has been previously reported.[35] Mixing ratios from other measurements, including NO_x and acetate CIMS, exhibited strong linear dependence upon CO despite different inlet locations and instrument averaging times (Figure 4.7). These

measurement comparisons coupled with the close proximity of MEFO to the fire support sufficient homogeneity of smoke plumes across spatially separated inlets.

4.3.4 Temporal variations in fire emissions

The largest increases in mixing ratios for all quantified compounds occurred within the first three minutes of the burn, consistent with the fire flaring up to a flaming stage. As the flames die down and the fire begins to smolder, mixing ratios remained enhanced above background, but to a lesser extent, throughout the day. We find these two time periods of fire emissions, initial and remaining, to be distinct. ERs (slopes) from scatter plots between NO_x and CO support the existence of two separate modes of combustion (Figure 4.7). During the first few minutes of the burn, NO_x was enhanced by a factor of 45 over the remainder of the fire. Similarly, enhancement of nitrated phenols was greater during the initial period than the remainder. The initial burn period is distinct from the remainder of the prescribed burn because of physicochemical differences in fire characteristics.

Reaction pathways that produce NO_x from fuel nitrogen become important at high combustion temperatures (> 800°C).[36] Combustion of N_2 by dissociated O atoms (Zeldovich mechanism or thermal NO) or by reaction with hydrocarbon radicals (prompt NO) only becomes important at temperatures >1600°C. Distillation or pyrolysis of fuel nitrogen can be important at much lower temperatures.[14,37] Wild fire temperatures can reach as high as 1200°C; however prescribed fires are designed to burn at lower temperatures due to abated fire intensity.[8] The initial period of greater NO_x enhancement is consistent with the very high temperature (800-1200°C) "combustion factor" from a positive matrix factor analysis of reactive nitrogen.[14]

Similar to the prescribed burn, at FIREX, flames were initially observed at high burn temperatures before cooling off when the fire began to smolder.

Particule size distributions shifted significantly from smaller to larger particles over the course of the fire at MEFO (Figure 4.8). Count median diameters dropped from background levels to ~60 nm at the start of the fire. As the fire progressed, median particle diameters increased linearly until late in the afternoon when a peak of ~100 nm was reached. Particle size distributions measured as part of the FLAME-4 campaign at the Missoula Fire Sciences Laboratory in 2012 exhibited similar shifts from smaller to larger particles as fires transitioned from flaming to smoldering combustion modes.[7] In experiments burning ponderosa pine, volume median diameters of ~50 nm and ~100 nm were measured during flaming and smoldering combustion respectively.

We therefore distinguish between the two modes of combustion at MEFO as higher temperature (initial) and lower temperature (remainder).

4.3.5 ERs

All categories of analytes were emitted in significantly greater quantities during higher temperature combustion than lower temperature combustion (Figure 4.9). Acids exhibit the lowest ERs of any category in spite of being the most concentrated species due to background mixing ratios much larger than the other categories. HNCO accounts for nearly 40% of other nitrogen-containing compounds and is enhanced >130 times more than the next most emitted nitrogenated compound. Though phenols are ~100 times more concentrated than nitrated

phenols, ERs for both categories are nearly identical during both fire modes. Figures A3.1-A3.4 show nitrated phenols scattered against CO on log-log scales.

Nitrated phenols are significantly more enhanced at higher combustion temperatures. Gas phase production of nitrated phenols proceeds by deprotonation of phenolic hydroxyl group by OH, radical rearrangement, and addition by NO_2. Though the sum of phenolic precursors is similarly more enhanced, ER increases for nitrobenzenediol, nitromethylbenzenediol, nitrocresol, dinitrocresol, nitrophenol, and dinitrophenol are 1.1-2.6 times higher than those of precursors at higher combustion temperatures (Table A3.1). Coinciding enhancement of nitrated phenols with NO_x during higher temperature combustion supports that NO_x is the limiting reagent in the production of these nitrated phenols. Once NO_x becomes abundant, nitrated phenols are rapidly produced.

ERs for 12 measured compounds are generally within an order of magnitude of ERs reported previously.[9,11,34,38–40] Exceptions include pyruvic and methacrylic acids as well as cresol. We note that none of the referenced ERs were measured from prescribed burning of ponderosa pine forest and the majority come from the Missoula Fire Lab. ERs for hydrogen cyanide (HCN) and formic acid (HCOOH) were measured during a prescribed fire in a California chaparral forest, for which similar emission profiles with ponderosa pine have been reported.[15,38] Priestley et al.,[34] observed normalized excess mixing ratios downwind from human-made bonfires in a UK city. Large variability is evident in functionalized acids, such as glycolic, acrylic, pyruvic, and methacrylic acids as well as HCN.

4.4 Conclusions

We presented near-field ERs for a number of SVOCs, including gaseous acids, phenols, and nitrated phenols. The prescribed burn at MEFO exhibited two distinct temperature modes.

NO_x production was favored at higher combustion temperatures. Production of nitrated phenols under these conditions outpaced enhancement of phenolic precursors by 1.1-2.6 times, suggesting that nitration of phenolic compounds is limited by the availability of NO_x. These reactions must occur rapidly (<5 min) for near-field detection in the gas phase. In forest fires, combustion temperature modes can change on a time scale of minutes. Subsequent changes in the chemistry of the fire shifts the distribution of gaseous products. As a result, ERs can change quickly and significantly over the course of a fire. These time-varying changes must be accounted for to accurately predict air quality hazards downwind of the fire and to manage the fire in a way that minimizing negative health impacts. HYSPLIT forward trajectories predicted that smoke plumes traversed the northern suburbs of Colorado Springs, a major metropolitan area, after ~3 hours of aging. Aged smoke plumes contain many known pollutants including toxic combustion products; such as isocyanic acid, phenols, and nitrated phenols; ozone; and particulate matter. Shifts in the combustion mode alter chemical pathways and could influence pollutant abundance in aged smoke. Further research is needed to understand these effects.

Chapter 4 Figures

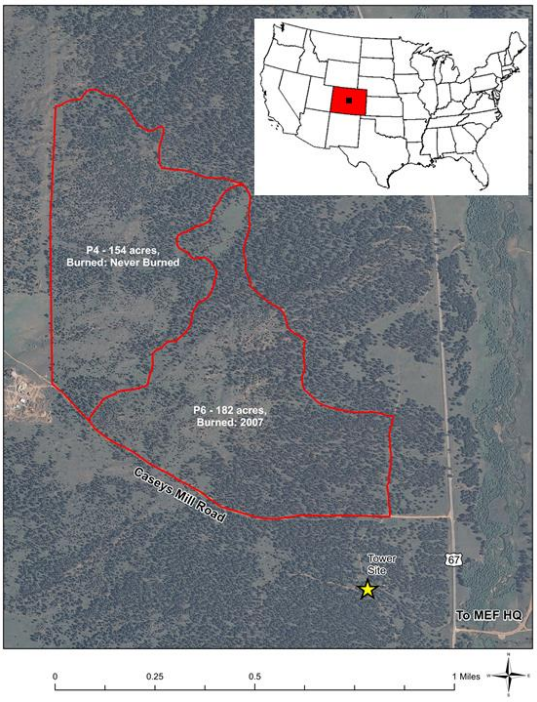

Figure 4.1. Map of two burned parcels (P4 and P6) shows close proximity of the fire (area within red lines) to the tower measurement site (yellow star). Inset shows general location of the study area (black dot) within the state of Colorado (red) in the contiguous United States.

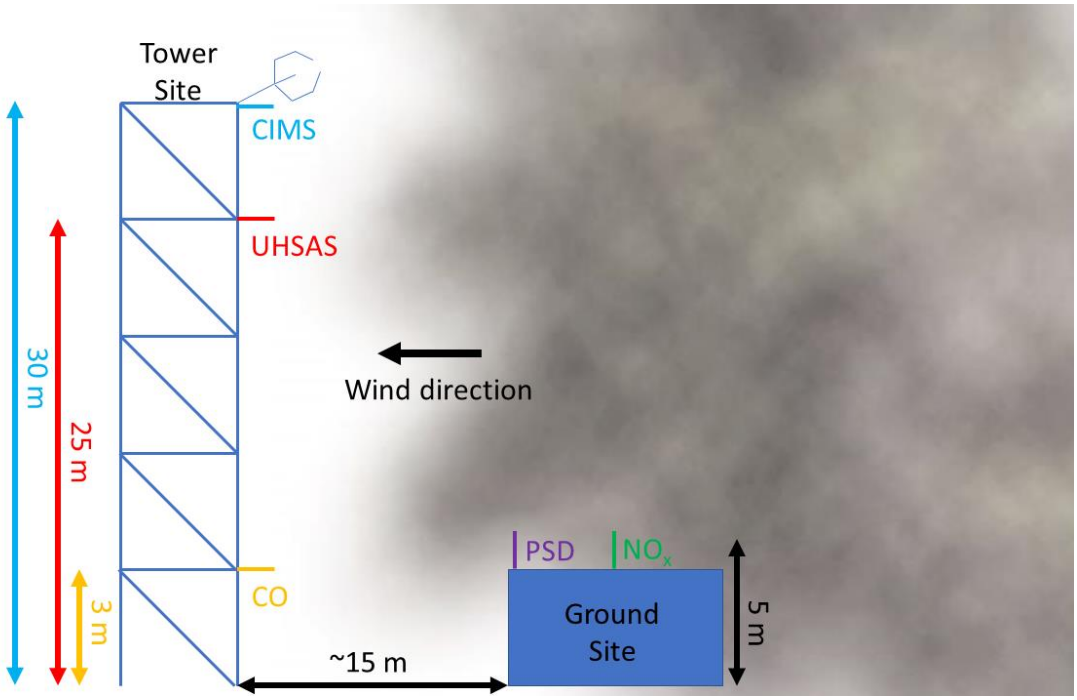

Figure 4.2. Measurements sampled through 5 inlets at the tower and ground sites were horizontally separated by ~15 m. Horizontal separation of Particle Size Distribution instrument (PSD) and NO_x inlets was negligible. Inlets were vertically separated by 2-27 m.

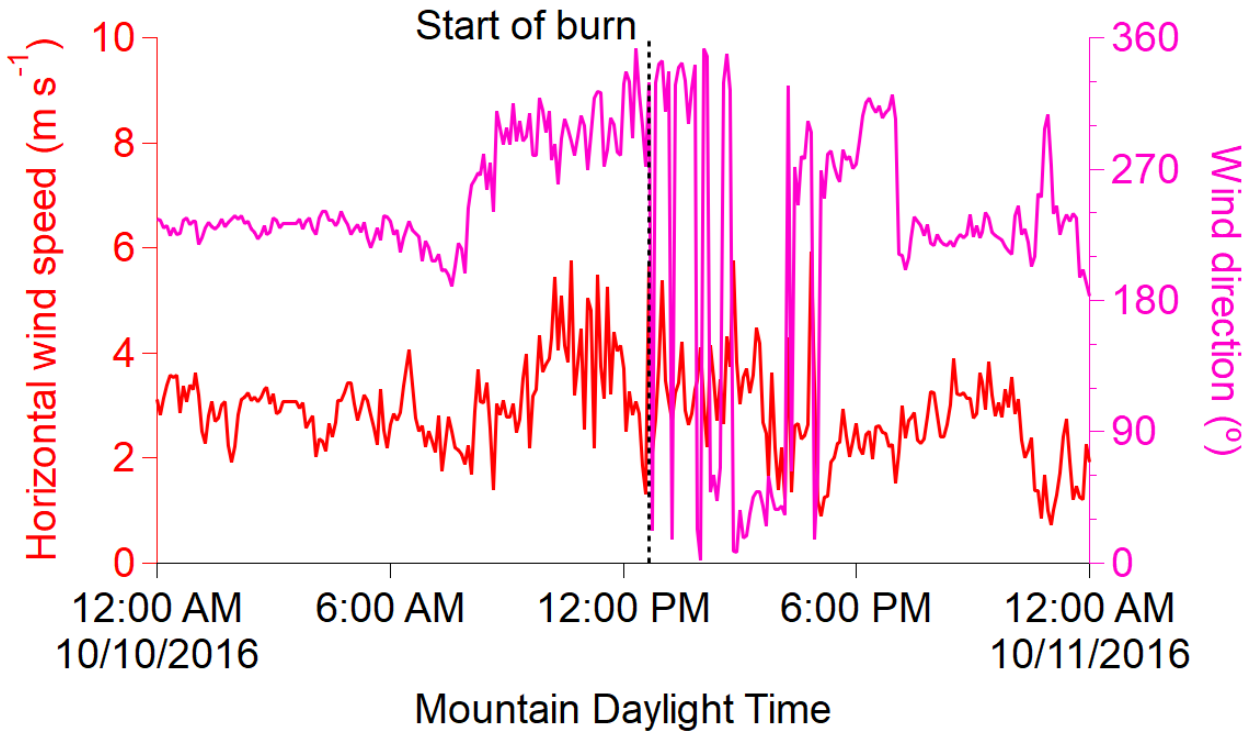

Figure 4.3. Westerly-to-northerly winds predominate during daytime on 10 October 2016. Average daytime horizontal wind speed was 3.5 m s^{-1}.

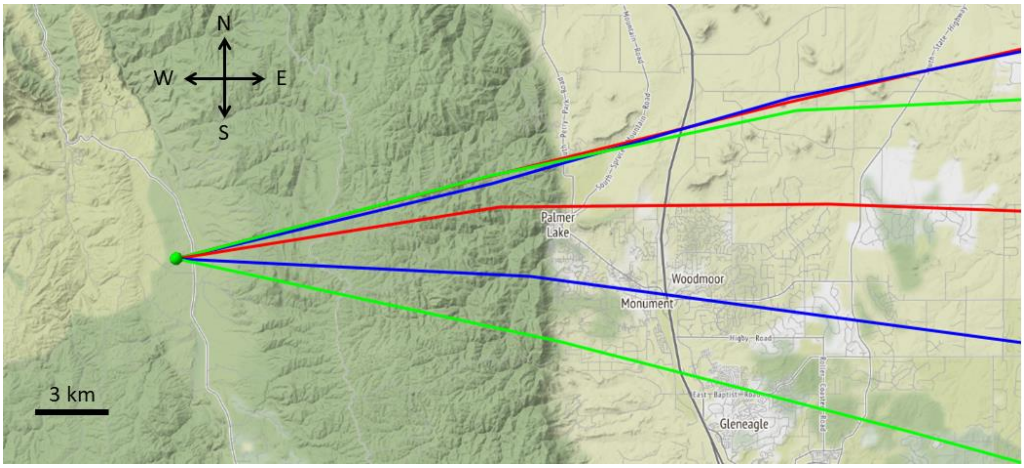

Figure 4.4. Six, 3-hour-long HYSPLIT model forward trajectories from the centroid of the prescribed burn travel east from Manitou Experimental Forest to northern suburbs of Colorado Springs, Colorado.

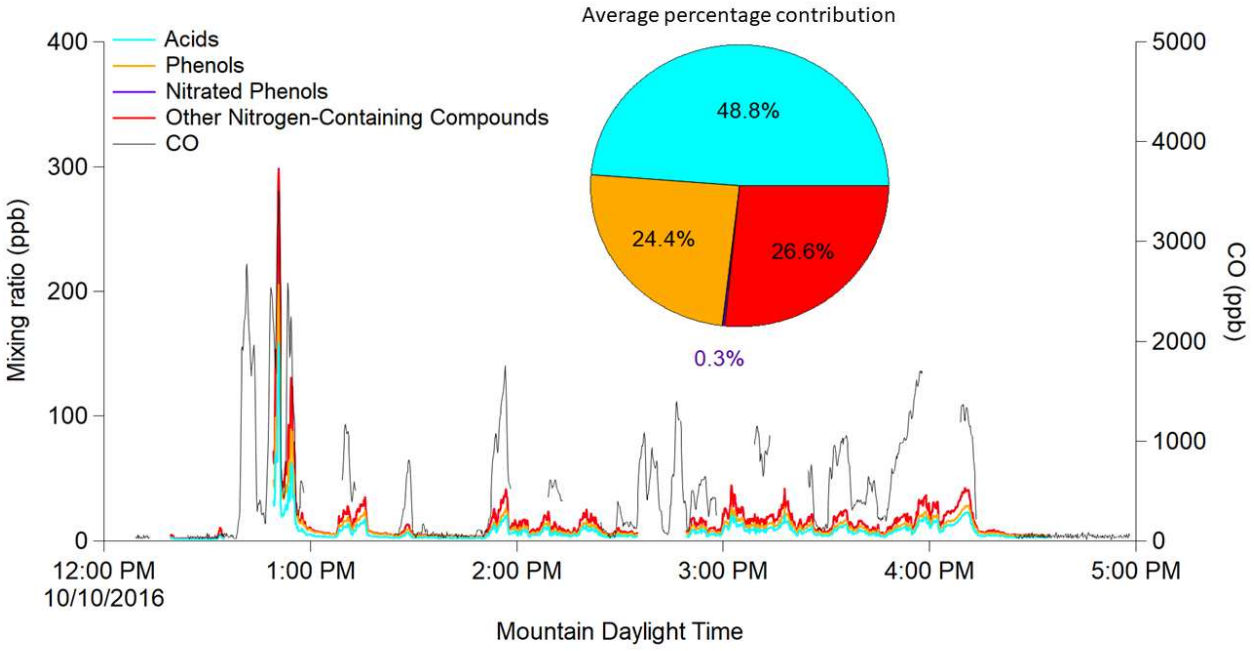

Figure 4.5. Several categories of compounds were enhanced during the prescribed burn, beginning at ~12:50 PM Mountain Daylight Time. On average, acids, phenols, and other account for >99% of quantified signal. Traces are stacked to show fractional contribution to total mixing ratio in time. Gaps in data signify calibration periods.

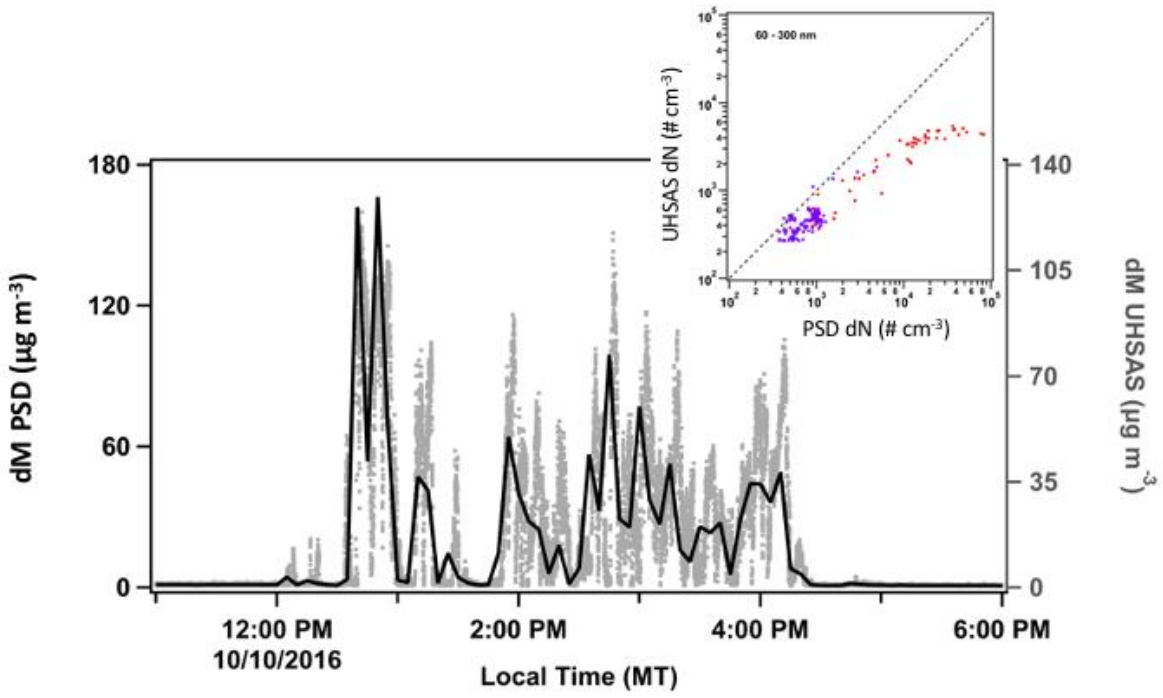

Figure 4.6. Despite spatially separated sensors and different acquisition times, particle mass concentrations, measured by PSD (black) and UHSAS (gray), trend strongly together in time. UHSAS detectors became saturated at particle number concentrations >3000 but agreed with PSD number concentrations <3000. In the inset, blue dots represent background periods and red dots periods enhanced by fire emissions.

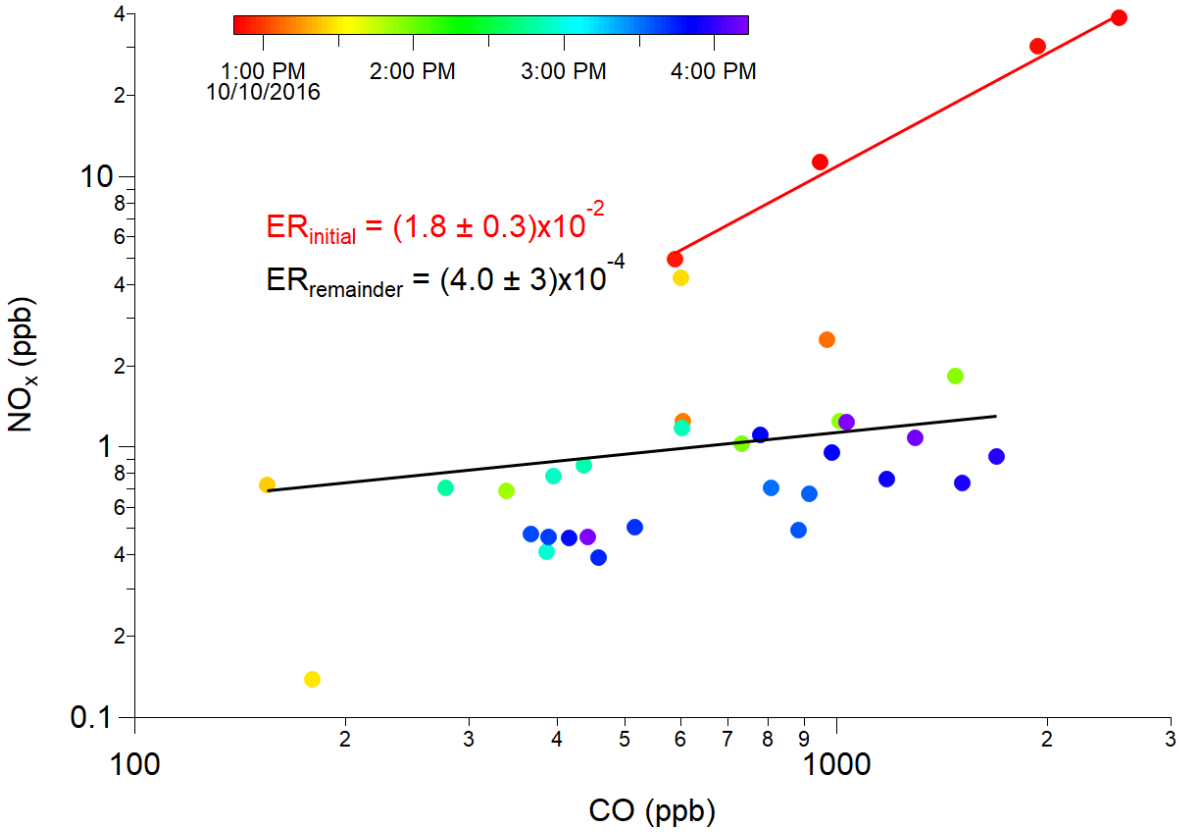

Figure 4.7. Initial ER, or slope of the red regression line, is significantly greater than the ER during the rest of the fire, slope of the black regression line. Circles are colored by Mountain Daylight Time on 10 October 2016. ER uncertainties are at the 95% confidence interval.

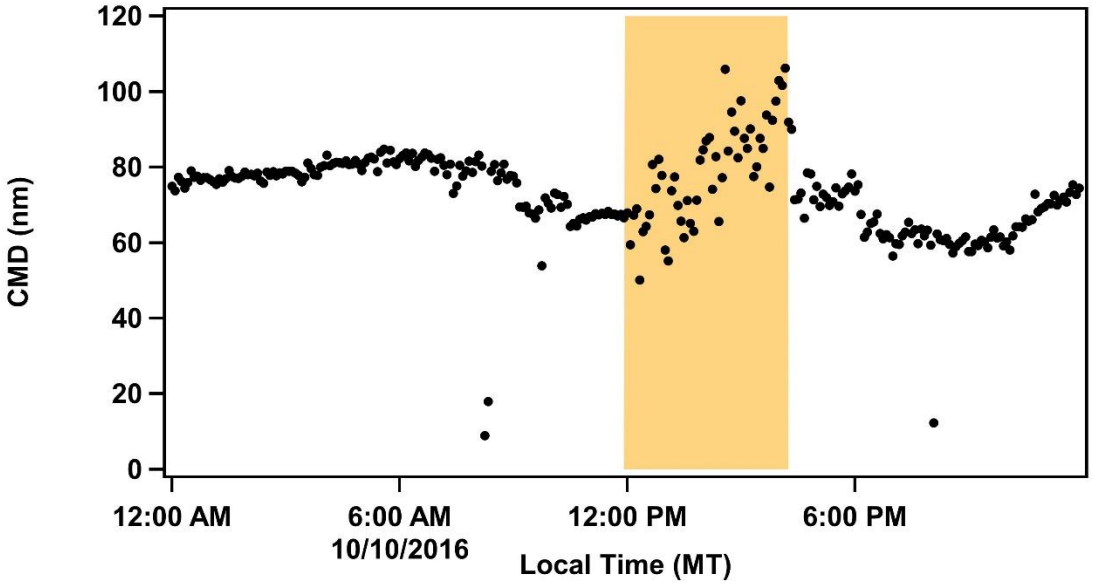

Figure 4.8. Aerosol count median diameters (CMD) increase substantially over the course of the fire (yellow highlighted region).

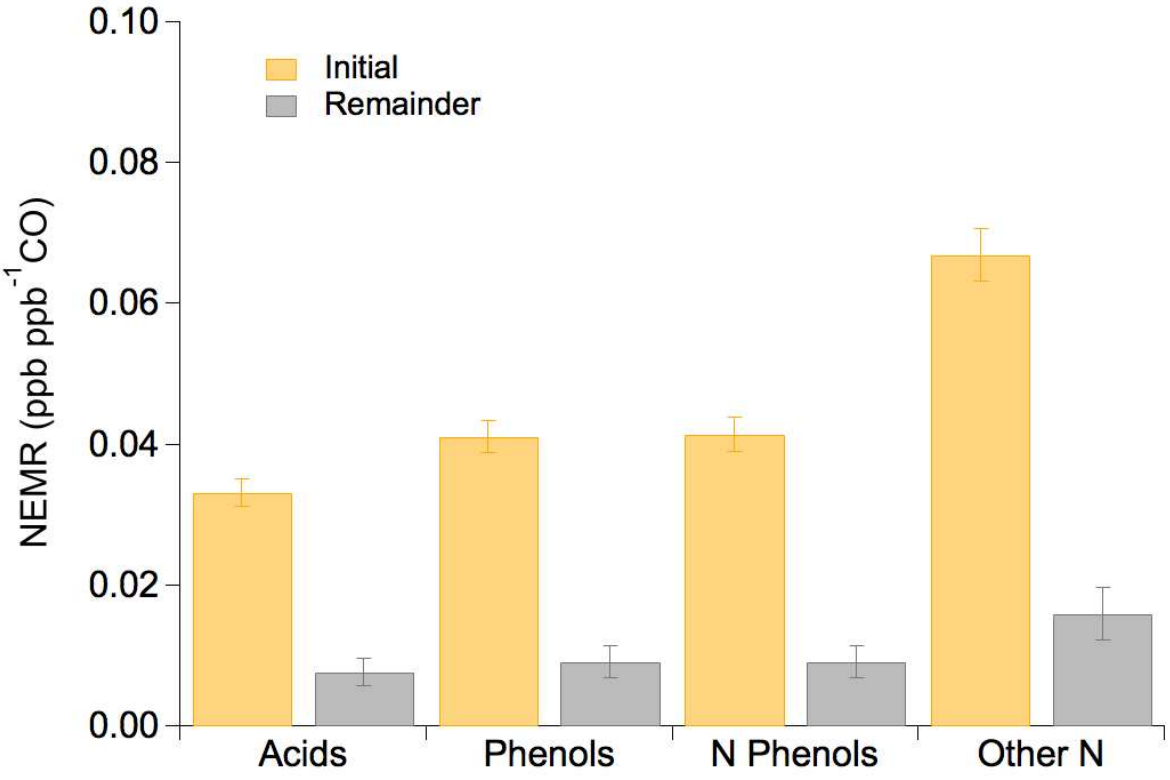

Figure 4.9. Sum of emission ratios (ERs) for all categorized are more enhanced during initial period of the burn than the remainder.

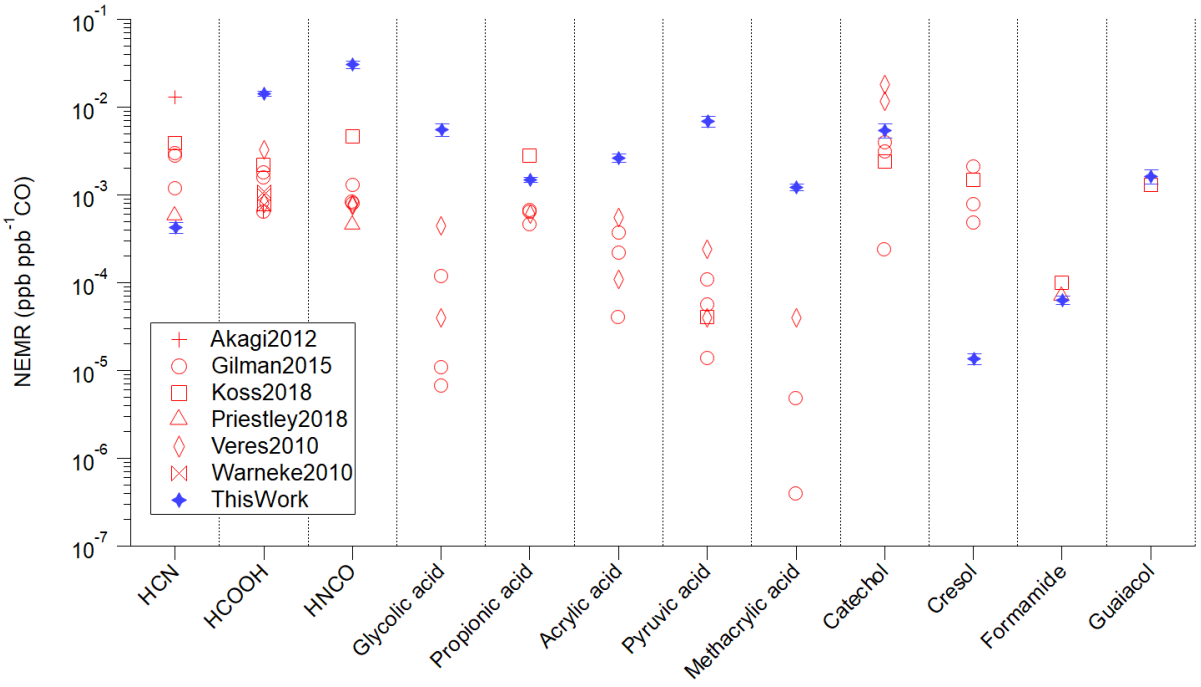

Figure 4.10. Comparison of normalized excess mixing ratios (NEMRs) from this work (solid blue diamonds) with those reported in previous works (open red shapes).

Chapter 4 Tables

Table 4.1. Ambient measurements of various analytes were made at different heights and acquisition times.

Instrument	Analyte(s)	Height (m)	Acquisition time (s)	Site
Acetate Time-of-Flight Chemical Ionization Mass Spectrometer (acetate CIMS)	Gaseous organic acids and phenolic compounds	30	0.2	tower
Ultra High Sensitivity Aerosol Spectrometer (UHSAS)	Size-resolved particles (60 – 1000 nm)	25	0.1	
Thermo Enviromental Model 48i CO	CO	3	10	
Rotary vane anemometer	Wind speed and direction	1.8, 7.0, 14, 28	300	
Thermo Scientific Model 42i-TL	NO_x	5	120	ground
National Center for Atmospheric Research Particle Size Distribution (PSD)	Size-resolved particles (4 – 300 nm)	5	300	

Table 4.2. List of phenolic compounds detected by acetate CIMS and corresponding gas phase acidities. The gas phase acidity of acetic acid is -1427 ± 8 kJ mol^{-1}.

Phenolic compound name	Formula	Gas phase acidity (kJ mol^{-1})
Phenol	C_6H_6O	-1432 ± 8
Nitrophenol	$C_6H_5NO_3$	-1379 ± 8
Dinitrophenol	$C_6H_4N_2O_5$	-1291 ± 8
Benzendiol	$C_6H_6O_2$	-1392 ± 8
Nitrobenzenediol	$C_6H_5NO_4$	n/a
Methylbenzenediol	$C_7H_8O_2$	n/a
Nitromethylbenzenediol	$C_7H_7NO_4$	n/a
Cresol	C_7H_8O	-1431 ± 8
Nitrocresol	$C_7H_7NO_3$	-1350 ± 8
Dinitrocresol	$C_7H_6N_2O_5$	n/a
Dimethylnitrophenol	$C_8H_9NO_3$	n/a
Salicylic acid	$C_7H_6O_3$	-1330 ± 8
Nitrosalicylic acid	$C_7H_5NO_5$	n/a
Coniferyl aldehyde	$C_{10}H_{10}O_3$	n/a

REFERENCES

(1) Akagi, S. K.; Yokelson, R. J.; Wiedinmyer, C.; Alvarado, M. J.; Reid, J. S.; Karl, T.; Crounse, J. D.; Wennberg, P. O. Emission Factors for Open and Domestic Biomass Burning for Use in Atmospheric Models. *Atmospheric Chem. Phys.* **2011**, *11* (9), 4039–4072. https://doi.org/10.5194/acp-11-4039-2011.

(2) Bond, T. C.; Streets, D. G.; Yarber, K. F.; Nelson, S. M.; Woo, J.-H.; Klimont, Z. A Technology-Based Global Inventory of Black and Organic Carbon Emissions from Combustion. *J. Geophys. Res. Atmospheres* **2004**, *109* (D14). https://doi.org/10.1029/2003JD003697.

(3) Wiedinmyer, C.; Quayle, B.; Geron, C.; Belote, A.; McKenzie, D.; Zhang, X.; O'Neill, S.; Wynne, K. K. Estimating Emissions from Fires in North America for Air Quality Modeling. *Atmos. Environ.* **2006**, *40* (19), 3419–3432. https://doi.org/10.1016/j.atmosenv.2006.02.010.

(4) Jaffe, D. A.; Wigder, N. L. Ozone Production from Wildfires: A Critical Review. *Atmos. Environ.* **2012**, *51*, 1–10. https://doi.org/10.1016/j.atmosenv.2011.11.063.

(5) Zauscher, M. D.; Wang, Y.; Moore, M. J. K.; Gaston, C. J.; Prather, K. A. Air Quality Impact and Physicochemical Aging of Biomass Burning Aerosols during the 2007 San Diego Wildfires. *Environ. Sci. Technol.* **2013**, *47* (14), 7633–7643. https://doi.org/10.1021/es4004137.

(6) Werf, G. R. van der; Randerson, J. T.; Giglio, L.; Leeuwen, T. T. van; Chen, Y.; Rogers, B. M.; Mu, M.; Marle, M. J. E. van; Morton, D. C.; Collatz, G. J.; Yokelson, R. J.; Kasibhatla, P. S. Global Fire Emissions Estimates during 1997–2016. *Earth Syst. Sci. Data* **2017**, *9* (2), 697–720. https://doi.org/10.5194/essd-9-697-2017.

(7) Carrico, C. M.; Prenni, A. J.; Kreidenweis, S. M.; Levin, E. J. T.; McCluskey, C. S.; DeMott, P. J.; McMeeking, G. R.; Nakao, S.; Stockwell, C.; Yokelson, R. J. Rapidly Evolving Ultrafine and Fine Mode Biomass Smoke Physical Properties: Comparing Laboratory and Field Results. *J. Geophys. Res. Atmospheres* **2016**, *121* (10), 5750–5768. https://doi.org/10.1002/2015JD024389.

(8) Jaffe, D. A.; O'Neill, S. M.; Larkin, N. K.; Holder, A. L.; Peterson, D. L.; Halofsky, J. E.; Rappold, A. G. Wildfire and Prescribed Burning Impacts on Air Quality in the United States. *J. Air Waste Manag. Assoc.* **2020**, *70* (6), 583–615. https://doi.org/10.1080/10962247.2020.1749731.

(9) Gilman, J. B.; Lerner, B. M.; Kuster, W. C.; Goldan, P. D.; Warneke, C.; Veres, P. R.; Roberts, J. M.; Gouw, J. A. de; Burling, I. R.; Yokelson, R. J. Biomass Burning Emissions and Potential Air Quality Impacts of Volatile Organic Compounds and Other Trace Gases from Fuels Common in the US. *Atmospheric Chem. Phys.* **2015**, *15* (24), 13915–13938. https://doi.org/10.5194/acp-15-13915-2015.

(10) Hays, M. D.; Geron, C. D.; Linna, K. J.; Smith, N. D.; Schauer, J. J. Speciation of Gas-Phase and Fine Particle Emissions from Burning of Foliar Fuels. *Environ. Sci. Technol.* **2002**, *36* (11), 2281–2295. https://doi.org/10.1021/es0111683.

(11) Koss, A. R.; Sekimoto, K.; Gilman, J. B.; Selimovic, V.; Coggon, M. M.; Zarzana, K. J.; Yuan, B.; Lerner, B. M.; Brown, S. S.; Jimenez, J. L.; Krechmer, J.; Roberts, J. M.; Warneke, C.; Yokelson, R. J.; Gouw, J. de. Non-Methane Organic Gas Emissions from Biomass Burning: Identification, Quantification, and Emission Factors from PTR-ToF during the FIREX 2016 Laboratory Experiment. *Atmospheric Chem. Phys.* **2018**, *18* (5), 3299–3319. https://doi.org/10.5194/acp-18-3299-2018.

(12) Yokelson, R. J.; Burling, I. R.; Gilman, J. B.; Warneke, C.; Stockwell, C. E.; Gouw, J. de; Akagi, S. K.; Urbanski, S. P.; Veres, P.; Roberts, J. M.; Kuster, W. C.; Reardon, J.; Griffith, D. W. T.; Johnson, T. J.; Hosseini, S.; Miller, J. W.; Cocker III, D. R.; Jung, H.; Weise, D. R. Coupling Field and Laboratory Measurements to Estimate the Emission Factors of Identified and Unidentified Trace Gases for Prescribed Fires. *Atmospheric Chem. Phys.* **2013**, *13* (1), 89–116. https://doi.org/10.5194/acp-13-89-2013.

(13) Carter, T. S.; Heald, C. L.; Jimenez, J. L.; Campuzano-Jost, P.; Kondo, Y.; Moteki, N.; Schwarz, J. P.; Wiedinmyer, C.; Darmenov, A. S.; Silva, A. M. da; Kaiser, J. W. How Emissions Uncertainty Influences the Distribution and Radiative Impacts of Smoke from Fires in North America. *Atmospheric Chem. Phys.* **2020**, *20* (4), 2073–2097. https://doi.org/10.5194/acp-20-2073-2020.

(14) Roberts, J. M.; Stockwell, C. E.; Yokelson, R. J.; Gouw, J. de; Liu, Y.; Selimovic, V.; Koss, A. R.; Sekimoto, K.; Coggon, M. M.; Yuan, B.; Zarzana, K. J.; Brown, S. S.; Santin, C.; Doerr, S. H.; Warneke, C. The Nitrogen Budget of Laboratory-Simulated Western U.S. Wildfires during the FIREX 2016 FireLab Study. *Atmospheric Chem. Phys. Discuss.* **2020**, 1–34. https://doi.org/10.5194/acp-2020-66.

(15) Sekimoto, K.; Koss, A. R.; Gilman, J. B.; Selimovic, V.; Coggon, M. M.; Zarzana, K. J.; Yuan, B.; Lerner, B. M.; Brown, S. S.; Warneke, C.; Yokelson, R. J.; Roberts, J. M.; Gouw, J. de. High- and Low-Temperature Pyrolysis Profiles Describe Volatile Organic Compound Emissions from Western US Wildfire Fuels. *Atmospheric Chem. Phys.* **2018**, *18* (13), 9263–9281. https://doi.org/10.5194/acp-18-9263-2018.

(16) Sun, Y. L.; Zhang, Q.; Anastasio, C.; Sun, J. Insights into Secondary Organic Aerosol Formed via Aqueous-Phase Reactions of Phenolic Compounds Based on High Resolution Mass Spectrometry. *Atmospheric Chem. Phys.* **2010**, *10* (10), 4809–4822. https://doi.org/10.5194/acp-10-4809-2010.

(17) Saha, S.; Mistri, R.; Ray, B. C. A Rapid and Selective Method for Simultaneous Determination of Six Toxic Phenolic Compounds in Mainstream Cigarette Smoke Using Single-Drop Microextraction Followed by Liquid Chromatography–Tandem Mass Spectrometry. *Anal. Bioanal. Chem.* **2013**, *405* (28), 9265–9272. https://doi.org/10.1007/s00216-013-7351-x.

(18) Harrison, M. A. J.; Barra, S.; Borghesi, D.; Vione, D.; Arsene, C.; Iulian Olariu, R. Nitrated Phenols in the Atmosphere: A Review. *Atmos. Environ.* **2005**, *39* (2), 231–248. https://doi.org/10.1016/j.atmosenv.2004.09.044.

(19) Mohr, C.; Lopez-Hilfiker, F. D.; Zotter, P.; Prévôt, A. S. H.; Xu, L.; Ng, N. L.; Herndon, S. C.; Williams, L. R.; Franklin, J. P.; Zahniser, M. S.; Worsnop, D. R.; Knighton, W. B.; Aiken, A. C.; Gorkowski, K. J.; Dubey, M. K.; Allan, J. D.; Thornton, J. A. Contribution of Nitrated Phenols to Wood Burning Brown Carbon Light Absorption in Detling, United Kingdom during Winter Time. *Environ. Sci. Technol.* **2013**, *47* (12), 6316–6324. https://doi.org/10.1021/es400683v.

(20) Finewax, Z.; de Gouw, J. A.; Ziemann, P. J. Identification and Quantification of 4-Nitrocatechol Formed from OH and NO3 Radical-Initiated Reactions of Catechol in Air in the Presence of NOx: Implications for Secondary Organic Aerosol Formation from Biomass Burning. *Environ. Sci. Technol.* **2018**, *52* (4), 1981–1989. https://doi.org/10.1021/acs.est.7b05864.

(21) Ortega, J.; Turnipseed, A.; Guenther, A. B.; Karl, T. G.; Day, D. A.; Gochis, D.; Huffman, J. A.; Prenni, A. J.; Levin, E. J. T.; Kreidenweis, S. M.; DeMott, P. J.; Tobo, Y.; Patton, E. G.; Hodzic, A.; Cui, Y. Y.; Harley, P. C.; Hornbrook, R. S.; Apel, E. C.; Monson, R. K.; Eller, A. S. D.; Greenberg, J. P.; Barth, M. C.; Campuzano-Jost, P.; Palm, B. B.; Jimenez, J. L.; Aiken, A. C.; Dubey, M. K.; Geron, C.; Offenberg, J.; Ryan, M. G.; Fornwalt, P. J.; Pryor, S. C.; Keutsch, F. N.; DiGangi, J. P.; Chan, A. W. H.; Goldstein, A. H.; Wolfe, G. M.; Kim, S.; Kaser, L.; Schnitzhofer, R.; Hansel, A.; Cantrell, C. A.; Mauldin, R. L.; Smith, J. N. Overview of the Manitou Experimental Forest Observatory: Site Description and Selected Science Results from 2008 to 2013. *Atmos Chem Phys* **2014**, *14* (12), 6345–6367. https://doi.org/10.5194/acp-14-6345-2014.

(22) Battaglia, M. A. Colorado Front Range Fuel Photo Series. **2005**.

(23) Battaglia, M. A.; Dodson, J. M.; Shepperd, W. D.; Platten, M. J.; Tallmadge, O. M. Colorado Front Range Fuel Photo Series. *Gen Tech Rep RMRS-GTR-155 Fort Collins CO US Dep. Agric. For. Serv. Rocky Mt. Res. Stn. 39 P* **2005**, *155*.

(24) Stolzenburg, M. R.; McMurry, P. H. Equations Governing Single and Tandem DMA Configurations and a New Lognormal Approximation to the Transfer Function. *Aerosol Sci. Technol.* **2008**, *42* (6), 421–432. https://doi.org/10.1080/02786820802157823.

(25) Cai, Y.; Montague, D. C.; Mooiweer-Bryan, W.; Deshler, T. Performance Characteristics of the Ultra High Sensitivity Aerosol Spectrometer for Particles between 55 and 800nm: Laboratory and Field Studies. *J. Aerosol Sci.* **2008**, *39* (9), 759–769. https://doi.org/10.1016/j.jaerosci.2008.04.007.

(26) Fulgham, S. R.; Brophy, P.; Link, M.; Ortega, J.; Pollack, I.; Farmer, D. K. Seasonal Flux Measurements over a Colorado Pine Forest Demonstrate a Persistent Source of Organic Acids. *ACS Earth Space Chem.* **2019**. https://doi.org/10.1021/acsearthspacechem.9b00182.

(27) Liu, S.; Thompson, S. L.; Stark, H.; Ziemann, P. J.; Jimenez, J. L. Gas-Phase Carboxylic Acids in a University Classroom: Abundance, Variability, and Sources. *Environ. Sci. Technol.* **2017**, *51* (10), 5454–5463. https://doi.org/10.1021/acs.est.7b01358.

(28) Veres, P.; Roberts, J. M.; Warneke, C.; Welsh-Bon, D.; Zahniser, M.; Herndon, S.; Fall, R.; de Gouw, J. Development of Negative-Ion Proton-Transfer Chemical-Ionization Mass Spectrometry (NI-PT-CIMS) for the Measurement of Gas-Phase Organic Acids in the Atmosphere. *Int. J. Mass Spectrom.* **2008**, *274* (1–3), 48–55. https://doi.org/10.1016/j.ijms.2008.04.032.

(29) Link, M. F. Air Quality Implications from Oxidation of Anthropogenic and Biogenic Precursors in the Troposphere. **2020**.

(30) Murschell, T.; Fulgham, S. R.; Farmer, D. K. Gas-Phase Pesticide Measurement Using Iodide Ionization Time-of-Flight Mass Spectrometry. *Atmospheric Meas. Tech.* **2017**, *10* (6), 2117–2127. https://doi.org/10.5194/amt-10-2117-2017.

(31) Yokelson, R. J.; Crounse, J. D.; DeCarlo, P. F.; Karl, T.; Urbanski, S.; Atlas, E.; Campos, T.; Shinozuka, Y.; Kapustin, V.; Clarke, A. D.; Weinheimer, A.; Knapp, D. J.; Montzka, D. D.; Holloway, J.; Weibring, P.; Flocke, F.; Zheng, W.; Toohey, D.; Wennberg, P. O.; Wiedinmyer, C.; Mauldin, L.; Fried, A.; Richter, D.; Walega, J.; Jimenez, J. L.; Adachi, K.; Buseck, P. R.; Hall, S. R.; Shetter, R. Emissions from Biomass Burning in the Yucatan. *Atmospheric Chem. Phys.* **2009**, *9* (15), 5785–5812. https://doi.org/10.5194/acp-9-5785-2009.

(32) Peng, Q.; Palm, B. B.; Melander, K. E.; Lee, B. H.; Hall, S. R.; Ullmann, K.; Campos, T.; Weinheimer, A. J.; Apel, E. C.; Hornbrook, R. S.; Hills, A. J.; Montzka, D. D.; Flocke, F.; Hu, L.; Permar, W.; Wielgasz, C.; Lindaas, J.; Pollack, I. B.; Fischer, E. V.; Bertram, T. H.; Thornton, J. A. HONO Emissions from Western U.S. Wildfires Provide Dominant Radical Source in Fresh Wildfire Smoke. *Environ. Sci. Technol.* **2020**, *54* (10), 5954–5963. https://doi.org/10.1021/acs.est.0c00126.

(33) Li, M.; Wang, X.; Lu, C.; Li, R.; Zhang, J.; Dong, S.; Yang, L.; Xue, L.; Chen, J.; Wang, W. Nitrated Phenols and the Phenolic Precursors in the Atmosphere in Urban Jinan, China. *Sci. Total Environ.* **2020**, *714*, 136760. https://doi.org/10.1016/j.scitotenv.2020.136760.

(34) Priestley, M.; Breton, M. L.; Bannan, T. J.; Leather, K. E.; Bacak, A.; Reyes-Villegas, E.; Vocht, F. D.; Shallcross, B. M. A.; Brazier, T.; Khan, M. A.; Allan, J.; Shallcross, D. E.; Coe, H.; Percival, C. J. Observations of Isocyanate, Amide, Nitrate, and Nitro Compounds From an Anthropogenic Biomass Burning Event Using a ToF-CIMS. *J. Geophys. Res. Atmospheres* **2018**, *123* (14), 7687–7704. https://doi.org/10.1002/2017JD027316.

(35) Kupc, A.; Williamson, C.; Wagner, N. L.; Richardson, M.; Brock, C. A. Modification, Calibration, and Performance of the Ultra-High Sensitivity Aerosol Spectrometer for Particle Size Distribution and Volatility Measurements during the Atmospheric Tomography Mission (ATom) Airborne Campaign. *Atmospheric Meas. Tech.* **2018**, *11* (1), 369–383. https://doi.org/10.5194/amt-11-369-2018.

(36) Glarborg, P.; Miller, J. A.; Ruscic, B.; Klippenstein, S. J. Modeling Nitrogen Chemistry in Combustion. *Prog. Energy Combust. Sci.* **2018**, *67*, 31–68. https://doi.org/10.1016/j.pecs.2018.01.002.

(37) Greenberg, J. P.; Friedli, H.; Guenther, A. B.; Hanson, D.; Harley, P.; Karl, T. Volatile Organic Emissions from the Distillation and Pyrolysis of Vegetation. *Atmospheric Chem. Phys.* **2006**, *6* (1), 81–91. https://doi.org/10.5194/acp-6-81-2006.

(38) Akagi, S. K.; Craven, J. S.; Taylor, J. W.; McMeeking, G. R.; Yokelson, R. J.; Burling, I. R.; Urbanski, S. P.; Wold, C. E.; Seinfeld, J. H.; Coe, H.; Alvarado, M. J.; Weise, D. R. Evolution of Trace Gases and Particles Emitted by a Chaparral Fire in California. *Atmospheric Chem. Phys.* **2012**, *12* (3), 1397–1421. https://doi.org/10.5194/acp-12-1397-2012.

(39) Veres, P.; Roberts, J. M.; Burling, I. R.; Warneke, C.; Gouw, J. de; Yokelson, R. J. Measurements of Gas-Phase Inorganic and Organic Acids from Biomass Fires by Negative-Ion Proton-Transfer Chemical-Ionization Mass Spectrometry. *J. Geophys. Res. Atmospheres* **2010**, *115* (D23). https://doi.org/10.1029/2010JD014033.

(40) Warneke, C.; Roberts, J. M.; Veres, P.; Gilman, J.; Kuster, W. C.; Burling, I.; Yokelson, R.; de Gouw, J. A. VOC Identification and Inter-Comparison from Laboratory Biomass Burning Using PTR-MS and PIT-MS. *Int. J. Mass Spectrom.* **2011**, *303* (1), 6–14. https://doi.org/10.1016/j.ijms.2010.12.002.

CHAPTER 5

CONCLUSIONS

5.1 Scientific outcomes and implications

This dissertation used seasonal measurements of a suite of organic gases over a Rocky Mountain ponderosa pine forest to probe atmospheric budgets, to explore additional sources and sinks of water-soluble gases, and to report hazardous fire emissions of semi-volatile compounds from very near field.

In Chapter 2 we observed that the forest is a persistent source of organic acids through all seasons. Net acid fluxes away from forest surfaces could not be explained by the sum of measured soil emissions, measured ponderosa pine emissions, modeled Formicine ant emissions, modeled chemical production, and modeled dry deposition. Chemical formation accounted for the largest fraction of acid production in the budgets. Disagreement between measurements and ground-up flux budgets implied a missing forest source, overestimated dry deposition model, or missing sink above measurement height. Acid fluxes increased with temperature, ozone, and vapor pressure deficit, but parameterizations only explained approximately half of the flux variance at best.

Much research has found a missing source of formic acid, both by observation of concentration and flux. Our study is no different in that regard. Here, we limit missing formic acid to secondary production by constraining direct emissions from trees and soil. Additional research of biogenic volatile organic compound oxidation pathways is needed to capture ambient formic acid concentrations and fluxes. The sequentially oxidation of monoterpenes and

sesquiterpenes will likely be important chemical pathways to explore for coniferous forests like MEFO.

In Chapter 3 we explored the hypothesis that water films or droplets on forest surfaces act as both a source and sink of water-soluble organic acids, which can produce spurious bi-directional fluxes for species without significant local sources, such as isocyanic acid. Distillation of or interception of neutral-to-alkaline wetness on forest surfaces can take up small acids and contribute to deposition fluxes. Evaporation of surface wetness can force equilibrium partitioning of small acids into the gas phase and contribute to emission fluxes. We showed that linear correlation of exchange velocity with dew point depression indicates that partitioning processes may be occurring, but correlations break down in dry environments or perhaps in different types of forested environments.

This research points to a need for targeted laboratory experiments that measure concentrations of water-soluble air pollutants in both the gas and aqueous phase of macroscopic droplets and microscopic water films. Surface wetness may act as an air pollutant reservoir or a mediator for uptake of pollutants to plants or soils. Knowledge of equilibrium or non-equilibrium processes are likely needed to reduce uncertainty in atmospheric budgets of water-soluble species.

In Chapter 4 we found that a prescribed burning of the forest adjacent to MEFO (<1 km) was a large source of semi-volatile organic compounds, including acids, phenols, and nitrated phenols. As evinced by variable NO_x enhancement and changing particle size distributions, the burn exhibited two different temperature regimes: higher initial temperature and lower remainder. While all fire emissions were greater at higher temperatures than lower temperatures, chemical precursors of nitrated phenols were enhanced variably. NO_x was enhanced drastically

more than phenolic precursors during the initial higher temperature period. Enhancement of nitrated phenols also outpaced that of phenols, suggesting that NO_2 was the limiting reagent to produce nitrated phenols at MEFO.

More near-field measurements of toxic nitrated phenolic compounds are needed to augment emission inventories with minimal atmospheric aging. Emission ratios should be representative of different forest types and environmental conditions. Lab studies of nitrated phenol production by fire are also needed to verify that production is enhanced at high temperatures and not attributable to separate, rapid-burning, nitrogen-rich fuels.

APPENDIX 1 - CHAPTER 2 SUPPORTING INFORMATION

A1.1 CIMS calibrations

UZA overflows the system inlet at the top of the tower for both blanks and formic acid external standard calibrations. The overflow is controlled by a high pressure (100 psi) normally-closed, two-way polychlorotrifluoroethylene (PCTFE) solenoid valve (NResearch Inc., model HP648T012). Permeation devices produce gas standards for calibration. Permeation tubes (VICI Metronics, Inc.) of formic, propionic, methacrylic, butyric, valeric, and heptanoic acids are housed in three 1" outer diameter (o.d.) glass containers with a constant flow of ultra-high purity nitrogen (UHP N_2). Critical orifices control flows over permeation devices. During winter and spring, methacrylic and butyric acid permeation tubes are stored in a single glass container. During summer and fall, propionic, methacrylic, butyric, and valeric acid permeation tubes are stored in a single glass container.

Each calibration period includes a system blank (e.g., an overflow of ultra-zero air (UZA)) introduced near the inlet tip on the tower) and a standard addition calibration (e.g., standard gases introduced at the CIMS inlet inside the trailer). Formic acid external standard calibrations were performed by overflowing UZA at the inlet tip on the tower and then adding gas standards for calibration at the CIMS inlet inside the trailer. These calibrations were conducted during winter and spring. Four organic acid permeation standards, formic, propionic, methacrylic, and butyric acid, were used during winter and spring. Valeric and heptanoic acids were added for summer and fall. Calibration periods followed one of two sequences. The first sequence includes standard additions for four acids as well as formic acid external standards: 1) system blank (60 – 95 s), 2) formic acid external standard step, 3) formic acid standard addition step, 4) propionic acid step, 5) methacrylic and butyric acids step, and 6) repeat steps 2 – 5 at

different dilution flows resulting in a range of organic acid concentrations. The second sequence includes standard additions for six acids without any external standards: 1) system blank (60 – 95 s), 2) formic acid step, 3) propionic, methacrylic, butyric, and valeric acids step, 4) heptanoic acid step, 5) repeat steps 2 – 4 at different mixing ratios. External standard mixing ratios range from 9.1 – 150 ppt_v formic acid. Standard additions mixing ratios range from 9.1 – 1200 ppt_v for formic acid, 5.4 – 1300 ppt_v for propionic acid, 14 - 1300 ppt_v for methacrylic acid, 13 – 1000 ppt_v for butyric acid, 260 - 1200 ppt_v for valeric acid, and 490 - 2500 ppt_v for heptanoic acid. Each concentration step was held for 120 s and each system blank for 60 – 95 s. Only the stable (flat) portion of signal at the end of each calibration step was used to derive instrument sensitivities. A sample calibration period is shown in Figure A1.6.

Outside of calibration periods, calibration gases were constantly vented through three-way, PCTFE solenoid valves (NResearch Inc., model 648K032) on each line. During calibration periods, calibration gas flows were diluted into a flow of UZA using a mass flow controller (MKS Instruments, model 1179). Diluted flow was allowed through a normally-closed, two-way PCTFE solenoid valve (NResearch Inc., model HP648T012) to reach a 3-way tee that connects the sample tubing, CIMS, and calibration gases. All six acids (summer and fall) are calibrated on-line by standard addition, without the UZA overflow to the inlet at the top of the tower (Figure A1.1). Average uncertainties in organic acid mixing ratios for all seasons range from 0.075 – 92 ppt_v.

A1.2 Supporting measurements

Ozone (O_3), carbon monoxide (CO), sulfur dioxide (SO_2), nitrogen oxides (NO_x=NO+NO_2), and meteorological parameters were measured at MEFO during all seasons in support of the organic acid flux measurements. Wind speed, wind direction, relative humidity,

ambient pressure, and ambient temperature were recorded at tower heights of 1.8, 7.0, 14.1, and 27.8 m above ground level (a.g.l.), photosynthetic photon flux density (PPFD) was measured at 3 m a.g.l., and precipitation was measured at ground level. Soil temperature was logged at 5, 20, and 50 cm a.g.l. Trace gas analyzers were housed inside an instrument trailer located at the base of the MEFO tower. O_3 (LOD 1.2 ppb_v; ±5% uncertainty) was measured using an analyzer employing ultraviolet (UV) absorption (2B Technologies Model 202). The inlet tip for the O_3 instrument was positioned at 5 m a.g.l. above the instrument trailer. CO was measured via non-dispersive infrared absorption (Thermo Environmental Model 48C), and its inlet tip was positioned at 5 m a.g.l. The CO and O_3 analyzers were calibrated before and after the field deployment in May 2015 and February 2016. A second O_3 analyzer (also by 2B Technologies, Model 202) was deployed at MEFO during summer and fall seasons. This instrument was calibrated three times during the summer and fall deployments using a similar NIST-traceable ozone calibration source (2B Technologies, Inc. Model 306); calibrations were performed over the 0 – 500 ppb_v range. SO_2 (LOD 0.05 ppb_v; ±5% uncertainty) was measured during summer and fall using a UV absorption-based analyzer (Teledyne, model T100U). The SO_2 analyzer was calibrated three times per season by standard addition of a NIST traceable 9.2 ppm_v mixture of SO_2 in air (Matheson) diluted into a flow of UZA resulting in calibration mixing ratios ranging from 0 to 100 ppb_v. The SO_2 analyzer was calibrated by overflowing the calibration mixture at the inlet to the detector inside the trailer. NO and NO_2 (LOD 2.3 ppb_v; ±5% uncertainty) were measured using a chemiluminescence-based analyzer with an inlet positioned roughly 5 m a.g.l. The use of molybdenum converters for atmospheric measurements of NO_2 are known to have interferences from PAN and other nitrogen oxides.[1] Therefore, in this work, we acknowledge that NO_2 measured during winter and spring using this instrument system likely represents the

sum of NO_2 plus some volatile organic nitrates and peroxy nitrates. As a result of this interference, NO and NO_2 measurements collected during summer and fall were performed using a Thermo Scientific NO analyzer (Model 42i-TL) employing the classic NO-O_3 chemiluminescence detection technique and configured to detect NO only. The analyzer was combined with a home-built converter that uses 395 nm LEDs for UV photolysis of NO_2 to NO. The UV-LED converter is positioned at the inlet tip and housed in a fan-cooled, weather-proof box located 5 m a.g.l. on top of the instrument trailer. PFA tubing is used wherever possible for the NO_x inlet and instrument system. A 3-way switching solenoid valve inside the inlet box switches between sampling from the UV-LED converter (e.g., measuring NO+NO_2) and a darkened sample line (e.g., measuring NO only). Calibration of the NO analyzer to NO was performed over the full range of the analyzer (0-100 ppb_v); calibration of the UV-LED converter and NO analyzer to NO_2 was performed for mixing ratios between 0 and 25 ppb_v. Known mixing ratios of NO were generated by dilution of a known flow of a 22 ppm NO in N_2 NIST calibrated standard into a known flow of UZA. Flows were measured to within ±1% uncertainty using a flow calibration device (Mesa Labs, Definer model DryCal unit). Known mixing ratios of NO_2 were generated by gas-phase titration of the same NO standard with O_3, which was generated from a source of UZA using a 285 nm lamp, before performing standard dilution into UZA. Calibration mixtures were generated at large enough flows that were sufficient to overflow the inlet tip. This NO_x instrument was calibrated in the laboratory before summer and after fall, and periodically throughout the field deployment. The efficiency of the LED-based converter for photolysis of NO_2 determined from these calibrations was consistently >95%.

A1.2.1 Soil and leaf chambers

During summer a 100 L Teflon branch enclosure was connected to the CIMS to measure ponderosa pine needle emissions. A dynamic flow (Q_{bag}) of 4.5 L min^{-1} through bag was directed to the CIMS. A concentration gradient (ΔC) was calculated between ambient organic acid concentration outside of the bag and measurements from inside the bag. Pine needle emissions (F_{needle}) of organic acids were calculated according to Eq. (A1).

$$F_{needle} = \frac{LAI \times \Delta C \times Q_{bag}}{LA_{bag}} \quad \text{(A1)}$$

Where LAI is leaf area index of 1.14 in units of m_{needle}^2 m_{ground}^{-2} and LA_{bag} is the leaf area in the bag estimated to be 0.125 m_{needle}^2. We note substantial uncertainty in the value of F_{needle} due to limited branch replication and potential wall losses in the inlet lines.

In fall we coupled soil chambers with the CIMS to measure soil and leaf litter emissions following the methods of Gray et al.[2] Briefly, three 10 L, stainless-steel chambers were installed near the flux tower for close proximity to the CIMS. Each chamber had a collar and a lid. Each chamber collar was gently inserted 2 - 5 cm into the soil surface 3 weeks before measurements (10 October – 31 October 2016) to allow them to come to steady state. All chambers included needle litter (approximately ~3 cm thick) and an average afternoon soil temperature of 12 °C at a depth of 5 cm. We measured soil emissions on 31 October and 1 November 2016 by attaching lids to the collars over Mylar gaskets to achieve an airtight seal and pumping 0.50 – 0.60 L min^{-1} of ambient air through each enclosed chamber. We sub-sampled 0.12 L min^{-1} of air through ~10 m of FEP tubing (1/8" inner diameter), which was mixed with a stream of UZA for a total flow of 4.5 L min^{-1} into the CIMS. We calculate soil organic acid emissions by Eq. (A2).

$$F = \frac{\Delta C \times Q \times P}{R \times A \times T} \quad \text{(A2)}$$

where ΔC is the concentration difference between the chamber and ambient air outside of the chamber accounting for inlet line dilution (ppt_v), Q is the flow into the chamber (L s^{-1}), P is

ambient pressure (bar), R is the gas constant (8.314 x 10^{-2} L bar mol^{-1} K^{-1}), A is chamber area in m^2, and T is ambient temperature in K.

A1.3 Resistance model

To estimate dry deposition of organic acids to forest surfaces at MEFO, we used a resistance model with modifications to the canopy resistance in accordance with Nguyen et al.[3,4] The resistance model calculates the resistance of the environment (r_{total}) to depositing gaseous organic acids as the sum of aerodynamic resistance (r_a) from the atmosphere, resistance from quasi-laminar boundary layers near surfaces (r_b), and resistance to uptake by canopy surfaces (r_c) as in Eq. (A3):

$$r_{total} = r_a + r_b + r_c = v_{dep}{}^{-1} \quad \text{(A3)}$$

The reciprocal of the estimated deposition velocity (v_{dep}) is equivalent to the total resistance (r_{total}), which has units of s m^{-1}. The aerodynamic resistance term (r_a) primarily depends upon the stability of the forest atmosphere and is calculated following Seinfeld and Pandis:[5]

$$r_a = \int_{z_0}^{z_r} \frac{\phi(\zeta)}{\kappa\, u_* \, z}\, dz \quad \text{(S4)}$$

Where the integration limits shown in Eq. (A4) are defined by the roughness length (z_0) and the measurement height (z_r), $\varphi(\zeta)$ represents the stability-dependent temperature vertical profile function, κ is the dimensionless von Karmann constant with a value of 0.41, u_* is the friction velocity with units of m s^{-1}, and z represents height above ground level. The resistance to molecular diffusion through quasi-laminar surface layers (r_b) is calculated according to Nguyen et al.[4]

$$r_b = \frac{v}{D\, u_*} \times \sqrt[3]{\frac{100\, l\, u_*}{LAI^2\, v}} \quad \text{(A5)}$$

Where ν is the kinematic viscosity of air with an average value of 1.25 x 10^{-5} m^2 s^{-1} at MEFO, D is the diffusivity constant (m^2 s^{-1}) of an organic acid molecule in air (calculated according to Graham's law and reported in Table A1.1), u_* represents the friction velocity with units of m s^{-1}, l is the average needle thickness at MEFO with a value of 0.001 m, and LAI is the dimensionless, single-sided leaf area index with a value of 1.14. The resistance of canopy surfaces (r_c) is the sum of the stomatal (r_s), mesophyll (r_m), and cuticular (r_{cut}) resistances:

$$r_c = r_s + r_m + r_{cut} \quad \text{(A6)}$$

The stomatal resistance is a function of an organic acid's ability to compete with water at diffusing into a stoma and is calculated according to Eq. (A7).

$$r_s = \frac{D_{water}}{D_{acid}} \times \frac{C_{water}}{g_s} \quad \text{(A7)}$$

Where D_{water} is the diffusivity constant of water, D_{acid} is the diffusivity constant of the organic acid, C_{water} is the mixing ratio of water vapor in units of mmol m^{-3}, and g_s is the stomatal conductance of water with units of mmol m^{-2} s^{-1}.[6] The mesophyll resistance depends upon an acid's ability to partition into the interior of a plant cell and is calculated by Eq. (A8).

$$r_m = \left(\frac{H_{acid}}{50\,R\,T} + 100 f_0\right)^{-1} \quad \text{(A8)}$$

Where H_{acid} is the Henry's law constant of a given organic acid in units of M atm^{-1}, R is the universal gas constant with a value of 0.08206 L atm mol^{-1} K^{-1}, T represents air temperature in units of K, and f_0 is a reactivity factor set to zero for all organic acids in this study. The cuticular resistance describes the ability of a needle's waxy cuticle to uptake organic acids and is calculated according to Eq. (A9).

$$r_{cut} = \left(\frac{10^{-4}\,H_{acid}}{R\,T} + f_0\right)^{-1} \quad \text{(A9)}$$

Where all variables are defined as in Eq. (A8).

LAI, *l*, and g_s values all originate from past work conducted in 2010-2011.[6] We note that single-sided *LAI* may be an underestimate of the surface area of a coniferous canopy capable of taking up gaseous organic acids. This is because ponderosa pine needles have stomata on all sides. To determine the sensitivity of our resistance model to changes in these parameters, we increase and decrease *LAI* and *l* values independently by a factor of 2. g_s values varied by >4x between months in summer 2011. Therefore, we test the sensitivity of our resistance model using the lowest measured stomatal conductance from that study. Findings of this sensitivity analysis are listed in Table A1.2. Sizeable variations in the magnitude of g_s change resistance model output very little. Double or halving needle thickness (*l*) results in modest (±10%) inverse enhancements to the model output. However, there is little evidence to indicate that needle thickness would drastically change between 2010-2011 to 2016. Increasing or decreasing the *LAI* by a factor of 2 alters the model output by only ±20%. However, there is little evidence to suggest that the canopy density at MEFO changed by such a large amount. In fact, an LAI of 1.14 at MEFO is consistent with leaf area indices measured at other ponderosa pine forests such as the Metolius Basin in Oregon (LAI = 1.3 – 1.7).[7]

Appendix A1 Figures

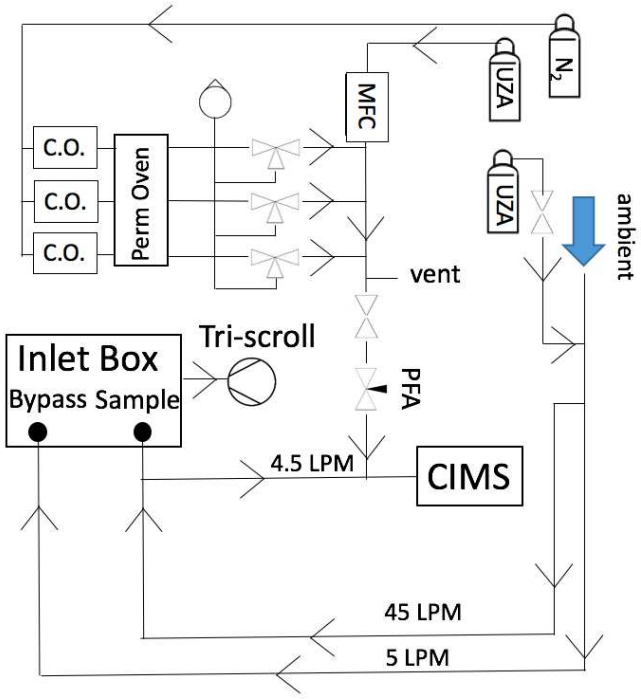

Figure A1.1. Schematic diagram of the inlet flow path to the CIMS instrument indicating flow rates and locations for calibration addition. Abbreviations include C.O. for critical orifice, MFC for mass flow controller, UZA for ultra-zero air, LPM for liters per minute, and PFA for perfluoroalkoxy polymer.

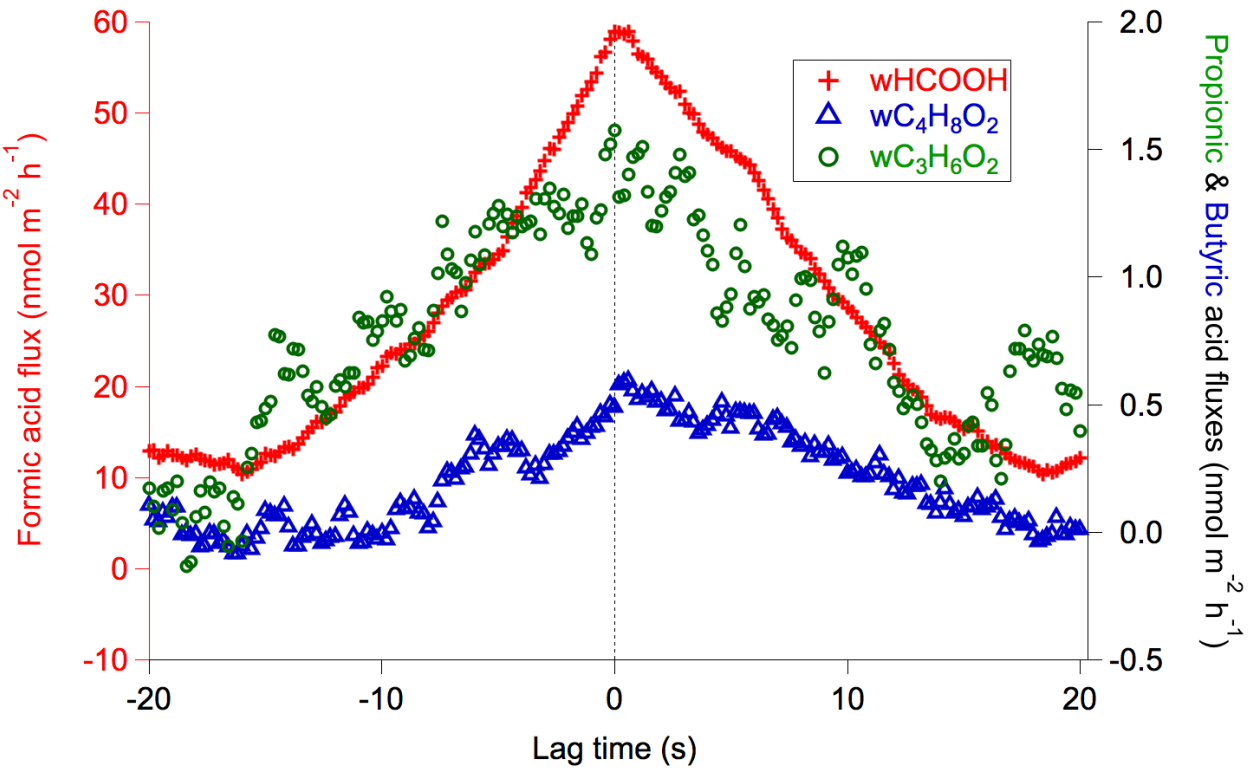

Figure A1.2. Fluxes of formic, propionic, and butyric acids are lagged ±20 s to observe the accuracy of a 4 s averaged lag applied to all measured fluxes.

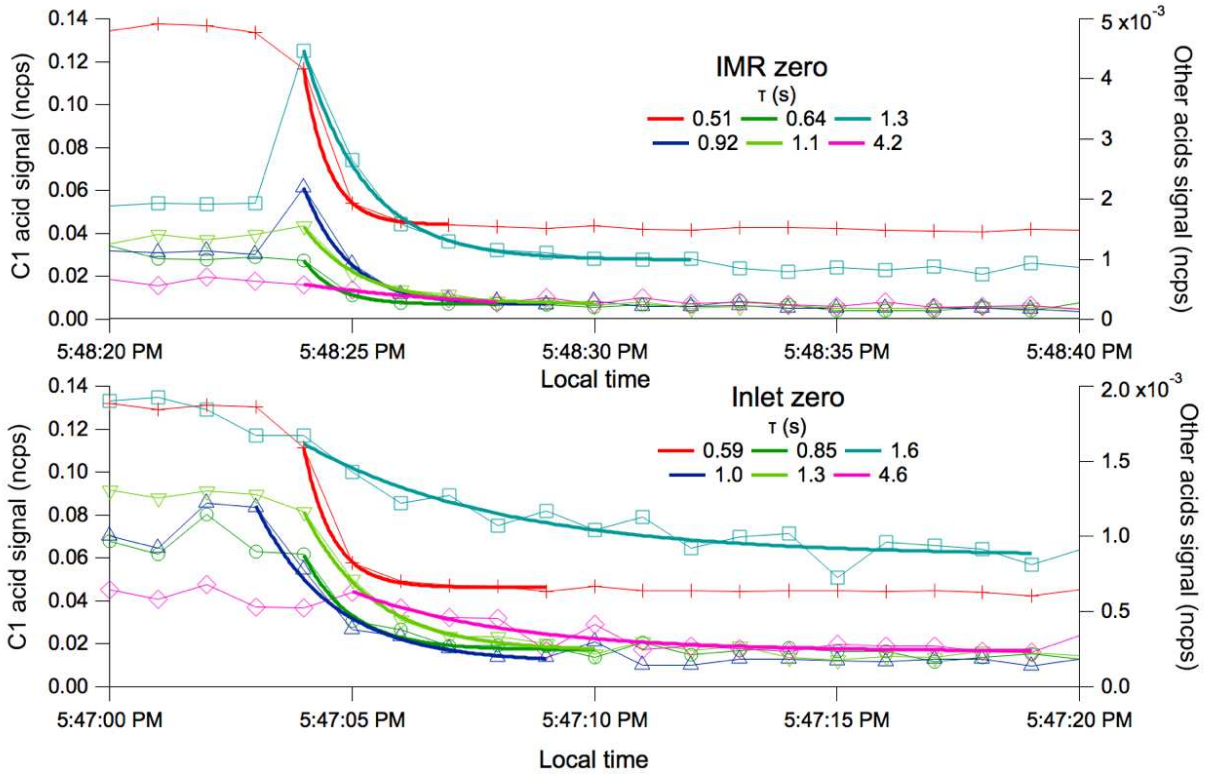

Figure A1.3. Time responses of the sampling and detection system for six organic acids were estimated with by overflowing ultra-pure zero air at the inlet tip and the CIMS entrance (IMR). Exponential offset curves ($y = y_0 + Ae^{\frac{-(x-x_0)}{\tau}}$) are fitted to each organic acid time series from the beginning of signal decrease to signal stabilization at background levels. Signal units on the y-axes are normalized counts per second (ncps).

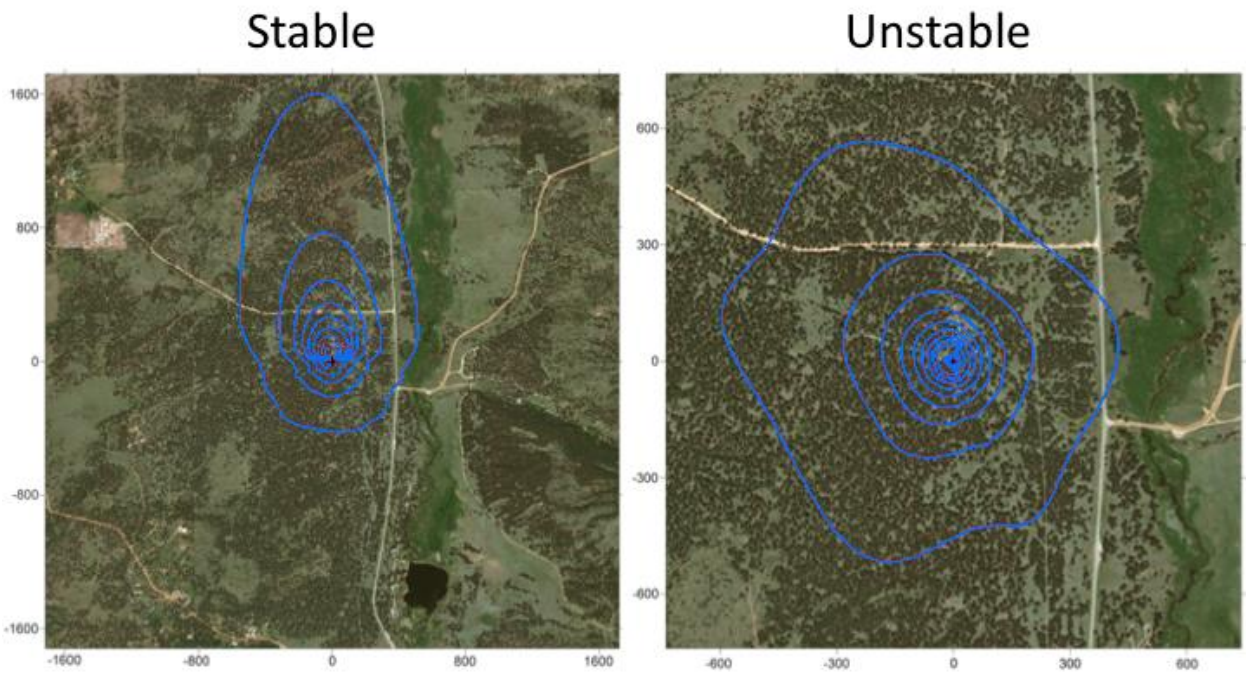

Figure A1.4. Flux footprints from SPiFFY summer campaign are typical of MEFO. Axes are both in units of m distance from the chemistry tower designated by a black plus sign in the center of each panel. Under stable atmospheric conditions, footprints are long (north and south) and narrow (east and west). Under unstable conditions, footprints are more evenly distributed. Contour lines account for percentage contribution to the flux – from 10 – 90%.

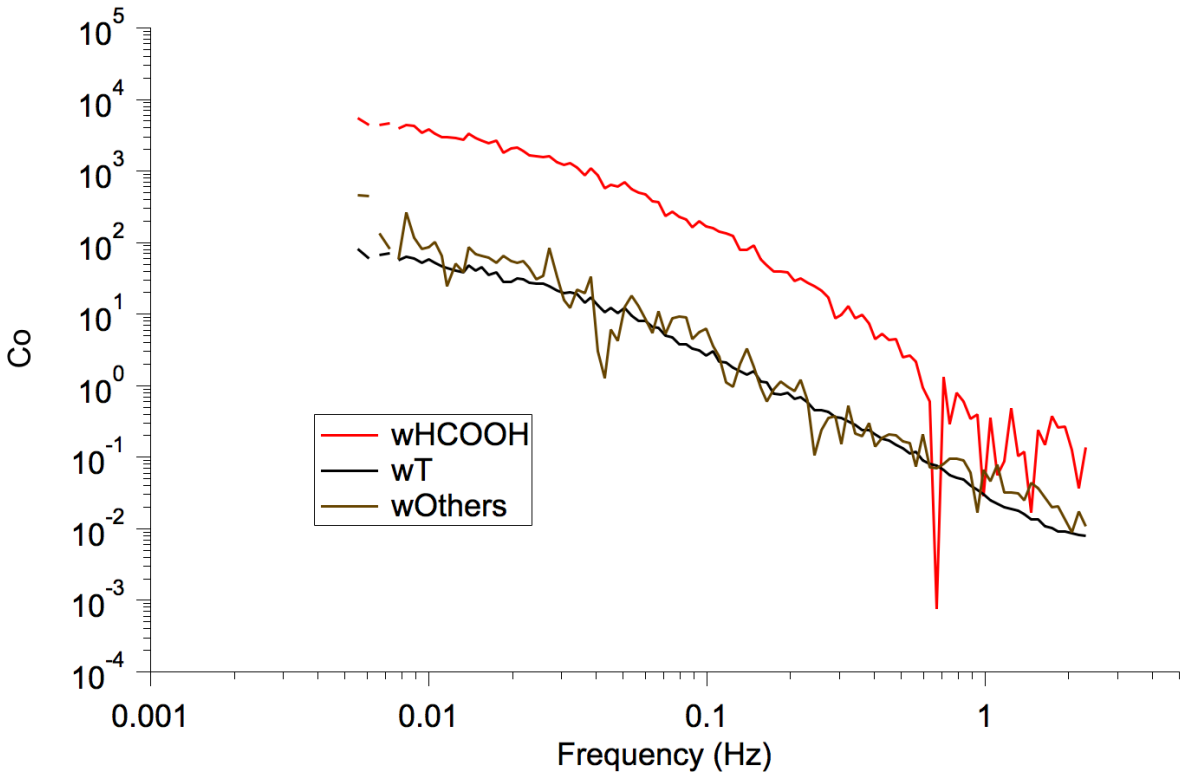

Figure A1.5. Summer seasonal average formic acid, the average of five acids, and sonic temperature cospectra with vertical wind speed. Organic acid cospectra (red and brown) trace favorably with wT cospectra (black). Although some high-frequency spectral attenuation is evident in formic acid cospectra (red), the area under the curve between 0.6 – 2.5 Hz accounts for < 1% of the average formic acid flux, or the area under the entire cospectral curve.

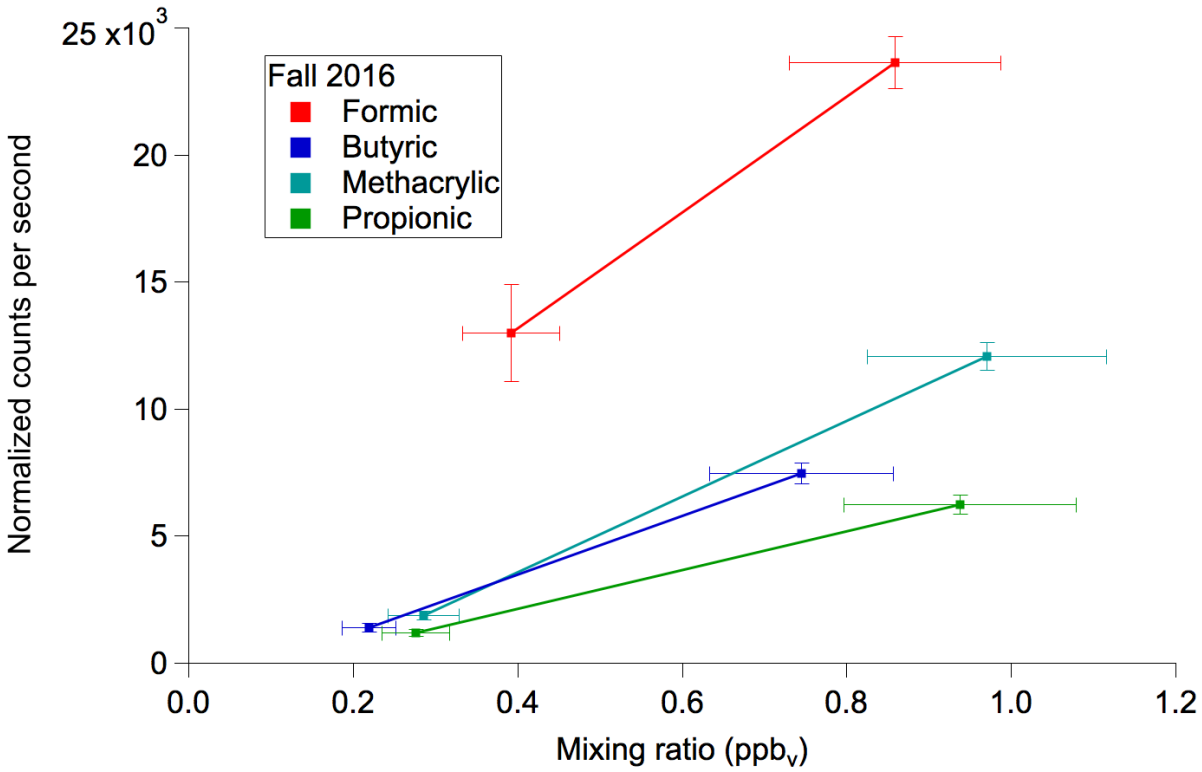

Figure A1.6. Sample automated, two-point CIMS calibration curve used at MEFO as bi-hourly checks of instrument sensitivity and background.

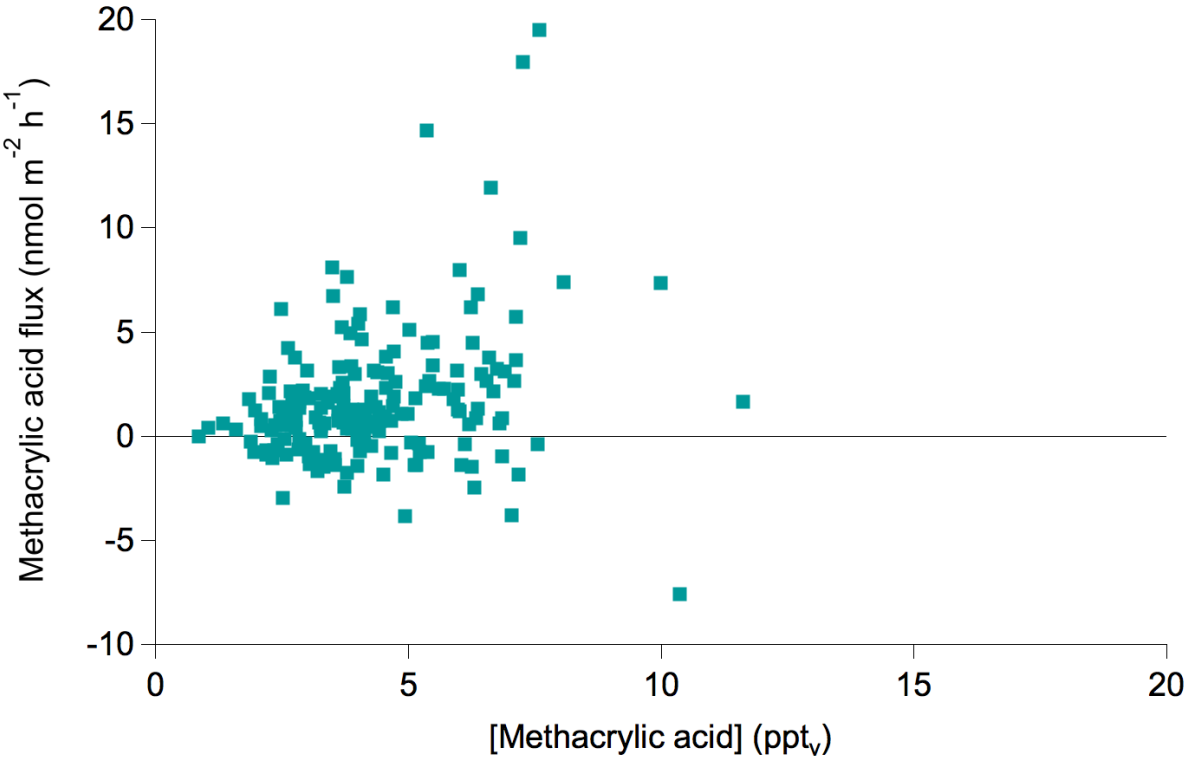

Figure A1.7. A representative organic acid scatter plot (in this case methacrylic acid) depicting flux (nmol m^{-2} h^{-1}) as a function of average concentration per flux period (ppt_v) during the fall campaign. No compensation point, or concentration at which flux direction changes from emission to deposition, is evident.

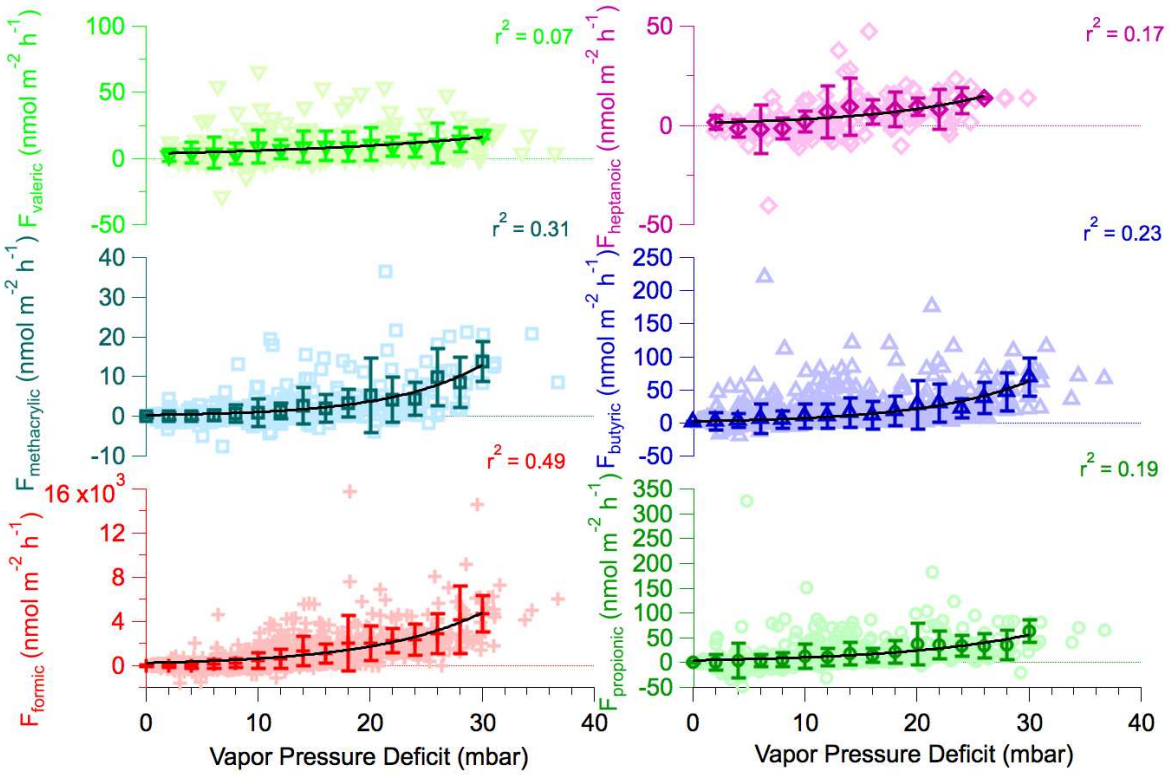

Figure A1.8. Organic acid fluxes increase with vapor pressure deficit, an environmental parameter that combines air temperature and relative humidity. Fluxes are averaged into 2 mbar vapor pressure deficit bins. We fit each scatter with an exponential equation. Correlation coefficients are calculated from linear regressions of exponentially modeled fluxes versus measured fluxes for all seasons.

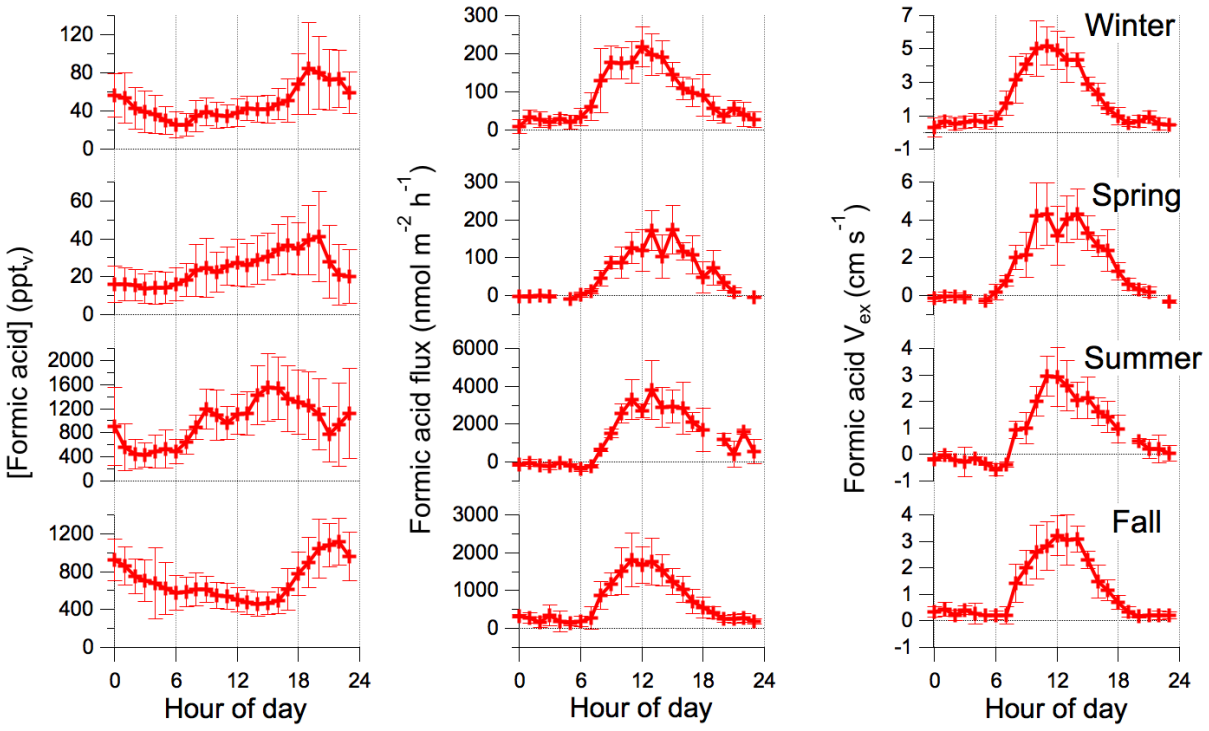

Figure A1.9. Seasonal diel mixing ratios (ppt$_v$, left), fluxes (nmol m^{-2} h^{-1}, center), and exchange velocities (cm s^{-1}, right) for formic acid. Data points represent seasonal, hourly medians. Error bars represent median absolute deviations (MAD). Fluxes and exchange velocities are filtered according to Sect. 2.4. From top to bottom, seasons are winter, spring, summer and fall.

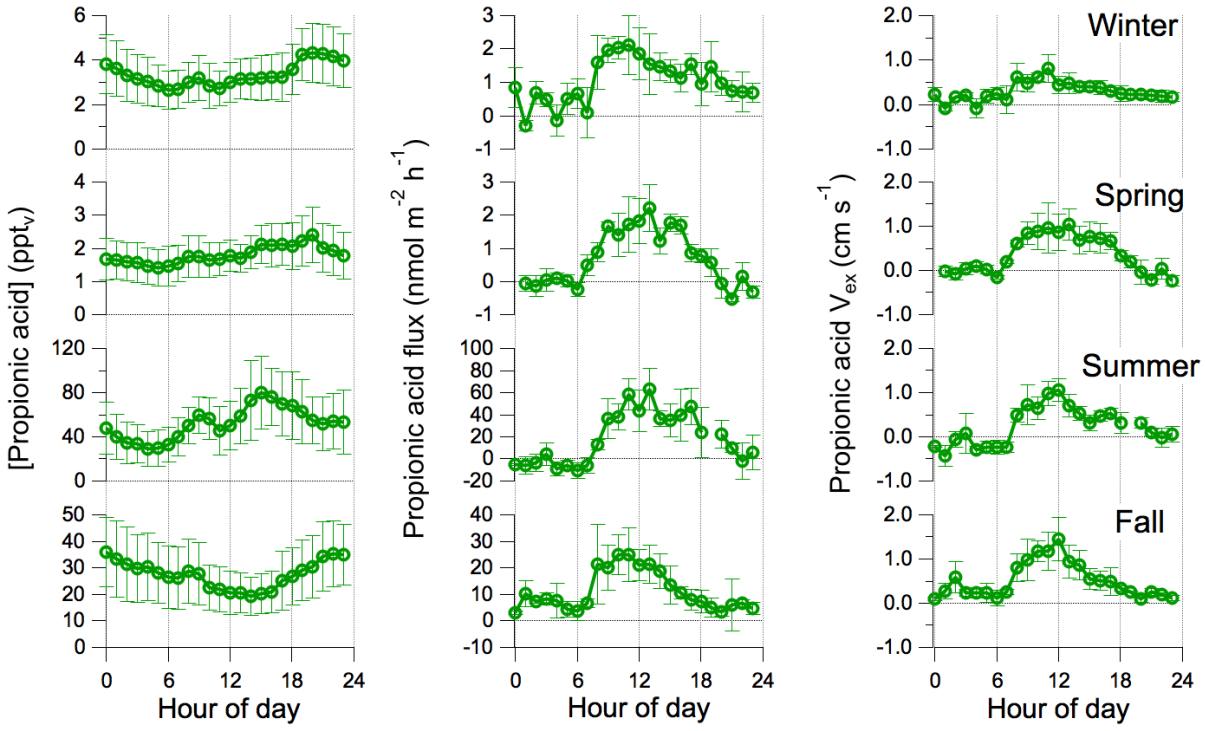

Figure A1.10. Seasonal diel mixing ratios (ppt$_v$, left), fluxes (nmol m^{-2} h^{-1}, center), and exchange velocities (cm s^{-1}, right) for propionic acid. Data points represent seasonal, hourly medians. Error bars represent median absolute deviations (MAD). Fluxes and exchange velocities are filtered according to Sect. 2.4. From top to bottom, seasons are winter, spring, summer and fall.

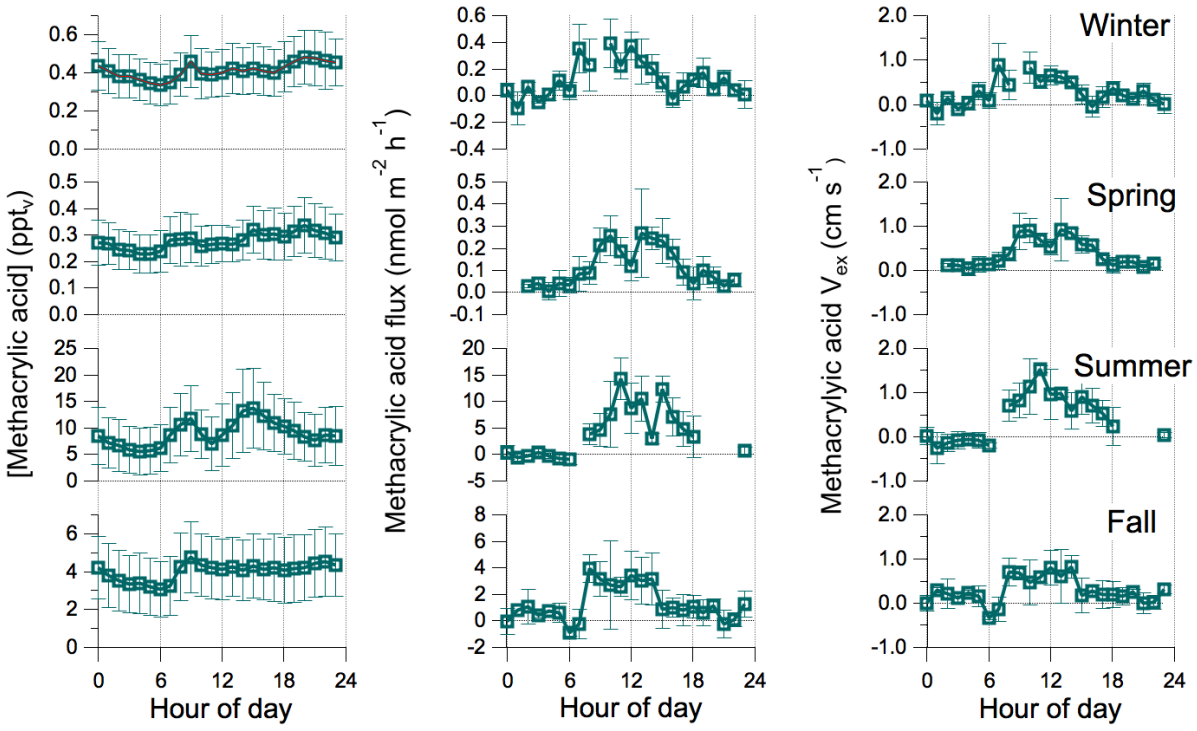

Figure A1.11. Seasonal diel mixing ratios (ppt$_v$, left), fluxes (nmol m^{-2} h^{-1}, center), and exchange velocities (cm s^{-1}, right) for methacrylic acid. Data points represent seasonal, hourly medians. Error bars represent median absolute deviations (MAD). Fluxes and exchange velocities are filtered according to Sect. 2.4. From top to bottom, seasons are winter, spring, summer and fall.

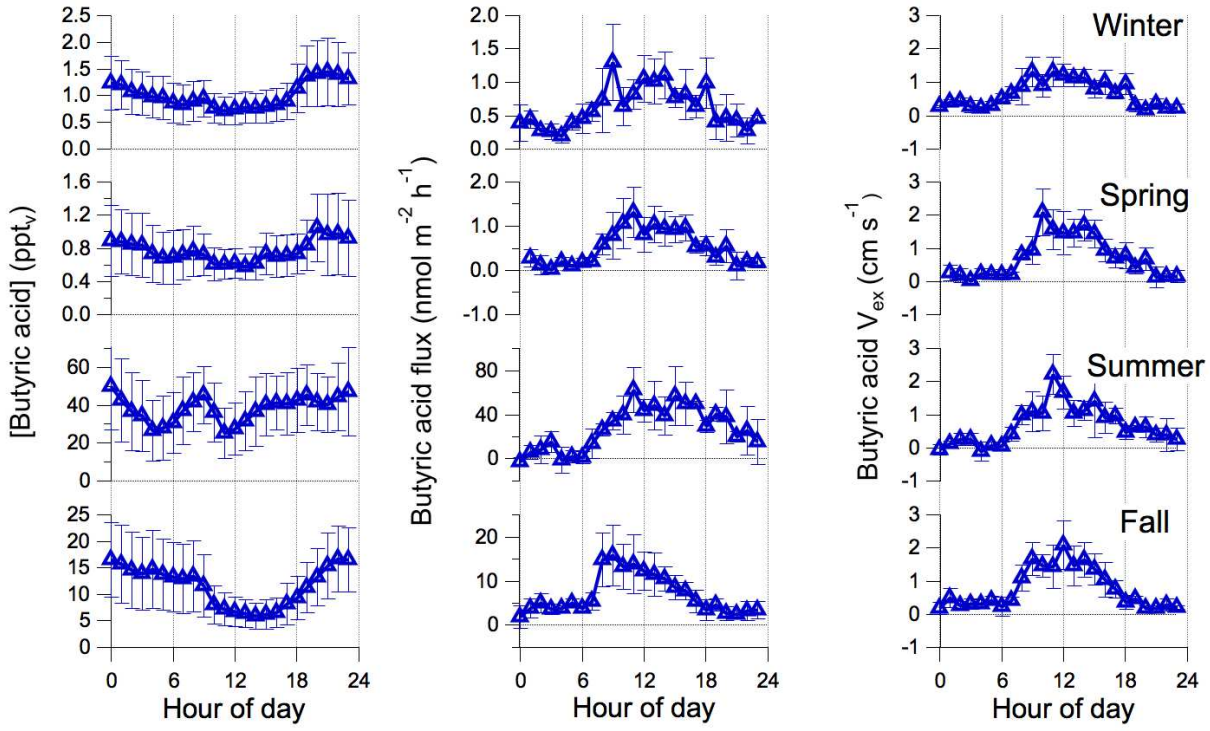

Figure A1.12. Seasonal diel mixing ratios (ppt$_v$, left), fluxes (nmol m^{-2} h^{-1}, center), and exchange velocities (cm s^{-1}, right) for butyric acid. Data points represent seasonal, hourly medians. Error bars represent median absolute deviations (MAD). Fluxes and exchange velocities are filtered according to Sect. 2.4. From top to bottom, seasons are winter, spring, summer and fall.

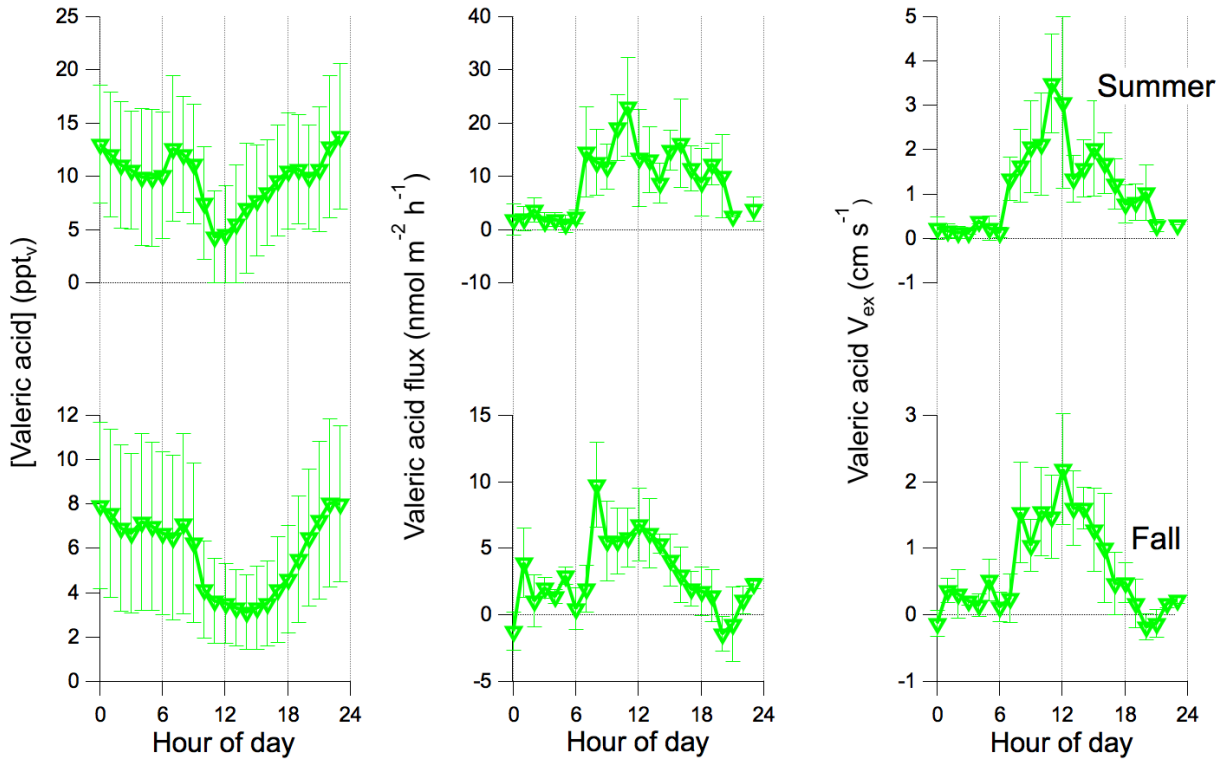

Figure A1.13. Seasonal diel mixing ratios (ppt$_v$, left), fluxes (nmol m^{-2} h^{-1}, center), and exchange velocities (cm s^{-1}, right) for valeric acid. Data points represent seasonal, hourly medians. Error bars represent median absolute deviations (MAD). Fluxes and exchange velocities are filtered according to Sect. 2.4. From top to bottom, seasons are summer and fall. Winter and spring measurements of valeric acid are unavailable due to a lack of calibrations during these seasons.

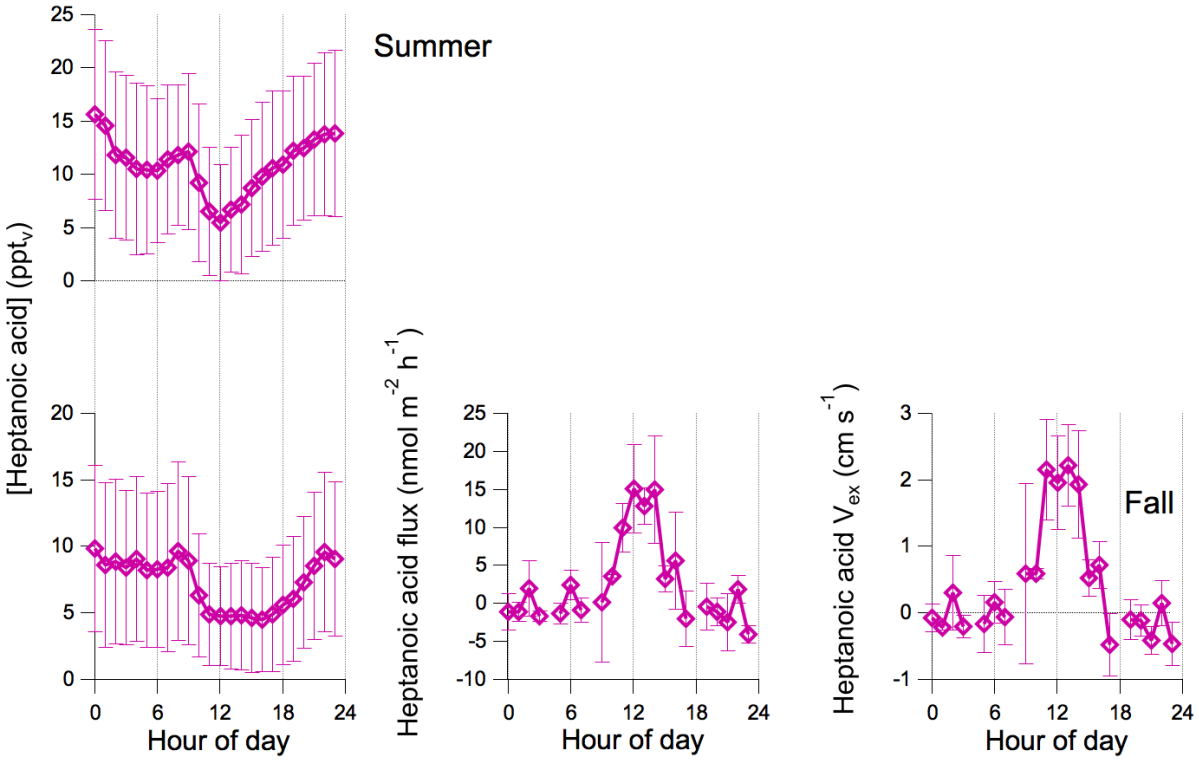

Figure A1.14. Seasonal diel mixing ratios (ppt$_v$, left), fluxes (nmol m^{-2} h^{-1}, center), and exchange velocities (cm s^{-1}, right) for heptanoic acid. Data points represent seasonal, hourly medians. Error bars represent median absolute deviations (MAD). Fluxes and exchange velocities are filtered according to Sect. 2.4. From top to bottom, seasons are summer and fall. Winter and spring measurements of heptanoic acid are unavailable due to a lack of calibrations during these seasons. Summer fluxes and exchange velocities for heptanoic acid do not meet filtering criteria.

Figure A1.15. Flow chart lists the data processing steps taken to transform chemical ionization mass spectrometer (CIMS) data (red) for organic acids and three-dimensional sonic anemometer data (blue) for vertical wind speed (w) into vertical flux data (purple) by the eddy covariance technique ($\overline{w'C'}$).

Appendix A1 Tables

Table A1.1. Diffusivity constants of six organic acids x10^5 as used by resistance model terms r_b and r_c. Constants were calculated based on the molecular weights (MW) of each acid and a diffusivity of 1.34 x 10^{-5} m^2 s^{-1} for formic acid [4] using Graham's law, or $D_{acid} = D_{formic} \times \sqrt{\frac{MW_{formic}}{MW_{acid}}}$.

Organic acid	Diffusivity x10^5 (m^2 s^{-1})
Formic	1.34
Propionic	1.06
Methacrylic	0.98
Butyric	0.97
Valeric	0.90
Heptanoic	0.80

Table A1.2. Sensitivity analysis of resistance model to *LAI*, *l*, and g_s. The adjusted value is the value used for the listed parameter in the sensitivity test.

Resistance parameter	Adjusted value	Change in resistance
LAI	0.57	-20%
LAI	2.28	+20%
l	0.0005 m	+10%
l	0.002 m	-10%
g_s	7 mmol m^{-2} s^{-1}	-0.02%

REFERENCES

(1) Dunlea, E. J.; Herndon, S. C.; Nelson, D. D.; Volkamer, R. M.; San Martini, F.; Sheehy, P. M.; Zahniser, M. S.; Shorter, J. H.; Wormhoudt, J. C.; Lamb, B. K.; Allwine, E. J.; Gaffney, J. S.; Marley, N. A.; Grutter, M.; Marquez, C.; Blanco, S.; Cardenas, B.; Retama, A.; Ramos Villegas, C. R.; Kolb, C. E.; Molina, L. T.; Molina, M. J. Evaluation of Nitrogen Dioxide Chemiluminescence Monitors in a Polluted Urban Environment. *Atmospheric Chem. Phys.* **2007**, *7* (10), 2691–2704. https://doi.org/10.5194/acp-7-2691-2007.

(2) Gray, C. M.; Monson, R. K.; Fierer, N. Biotic and Abiotic Controls on Biogenic Volatile Organic Compound Fluxes from a Subalpine Forest Floor. *J. Geophys. Res. Biogeosciences* **2014**, *119* (4), 2013JG002575. https://doi.org/10.1002/2013JG002575.

(3) Wesely, M. L. Parameterization of Surface Resistances to Gaseous Dry Deposition in Regional-Scale Numerical Models. *Atmospheric Environ. 1967* **1989**, *23* (6), 1293–1304.

(4) Nguyen, T. B.; Crounse, J. D.; Teng, A. P.; Clair, J. M. S.; Paulot, F.; Wolfe, G. M.; Wennberg, P. O. Rapid Deposition of Oxidized Biogenic Compounds to a Temperate Forest. *Proc. Natl. Acad. Sci.* **2015**, *112* (5), E392–E401. https://doi.org/10.1073/pnas.1418702112.

(5) Seinfeld, John H.; Pandis, Spyros N. *Atmospheric Chemistry and Physics: From Air Pollution to Climate Change*; Wiley, 1998.

(6) Ortega, J.; Turnipseed, A.; Guenther, A. B.; Karl, T. G.; Day, D. A.; Gochis, D.; Huffman, J. A.; Prenni, A. J.; Levin, E. J. T.; Kreidenweis, S. M.; DeMott, P. J.; Tobo, Y.; Patton, E. G.; Hodzic, A.; Cui, Y. Y.; Harley, P. C.; Hornbrook, R. S.; Apel, E. C.; Monson, R. K.; Eller, A. S. D.; Greenberg, J. P.; Barth, M. C.; Campuzano-Jost, P.; Palm, B. B.; Jimenez, J. L.; Aiken, A. C.; Dubey, M. K.; Geron, C.; Offenberg, J.; Ryan, M. G.; Fornwalt, P. J.; Pryor, S. C.; Keutsch, F. N.; DiGangi, J. P.; Chan, A. W. H.; Goldstein, A. H.; Wolfe, G. M.; Kim, S.; Kaser, L.; Schnitzhofer, R.; Hansel, A.; Cantrell, C. A.; Mauldin, R. L.; Smith, J. N. Overview of the Manitou Experimental Forest Observatory: Site Description and Selected Science Results from 2008 to 2013. *Atmos Chem Phys* **2014**, *14* (12), 6345–6367. https://doi.org/10.5194/acp-14-6345-2014.

(7) Law, B.; van tuyl, S.; Cescatti, A.; Baldocchi, D. Estimation of Leaf Area Index in Open-Canopy Ponderosa Pine Forests at Different Successional Stages and Management Regimes in Oregon. *Agric. For. Meteorol.* **2001**, *108*, 1–14. https://doi.org/10.1016/S0168-1923(01)00226-X.

APPENDIX 2 - CHAPTER 3 SUPPORTING INFORMATION

A2.1 Introduction

This supporting information presents brief discussions of eddy covariance flux measurements and filtering used at Manitou Experimental Forest Observatory (MEFO) (Section A2.2) and the calculation of volumetric phase ratios for phase distribution analysis (Section A2.3). Supporting figures include seasonal isocyanic acid (HNCO) exchange velocity (V_{ex}) plotted as a function of dew point depression ($T-T_d$) at MEFO in Figure A2.1, an intercomparison of V_{ex} versus $T-T_d$ for several volatile organic acids at three different measurement sites in Figures A2.2-A2.4, dew point depression histograms from three different flux measurement sites in Figure A2.5, HNCO temperature-dependent partitioning space plot in Figure A2.6, exponential temperature dependence of HNCO mixing ratio in Figure A2.7, modified van't Hoff plots for HNCO sorted by wet and dry conditions at MEFO in Figure A2.8, ΔH_{obs} derived from slopes of modified van't Hoff plots displayed as a function of $\Delta H_{solvation}$ from the literature for five acids under wet and dry conditions in Figure A2.9, modified van't Hoff plots for isoprene sorted by wet and dry conditions at University of Michigan Biological Station (UMBS) in Figure A2.10, and formic acid dependence upon latent heat flux at SMEAR 2 in Hyytiälä, Finland, in Figure A2.11. Average acetate CIMS organic acid sensitivities are listed in Table A2.1, and linear best fits and correlation coefficients for Figure 3.3 are listed in Table A2.2.

A2.2 Eddy flux

We calculate the quasi-continuous flux (F) as the averaged product of the instantaneous deviations of the vertical wind speed (w') and the acid mixing ratio (C') from their 30-minute means.

$$\boldsymbol{F = \overline{w'C'}} \quad \text{(S1)}$$

The exchange velocity (V_{ex}) is the flux normalized by the mean mixing ratio ($\boldsymbol{\overline{C}}$) and represents the rate at which trace gases move between the biosphere and atmosphere:

$$\boldsymbol{V_{ex} = \frac{F}{\overline{C}}} \quad \text{(S2)}$$

V_{ex} enables us to compare fluxes across different measurement sites where ambient mixing ratios vary and accounts for the bidirectionality of organic acid fluxes. Positive exchanges (+F and +V_{ex}) are upwards, away from ecosystem surfaces. Negative exchanges (-F and -V_{ex}) represent downward fluxes from the atmosphere towards ecosystem surfaces.

We filter the data to ensure that the vertical exchange is limited to local sources and sinks within the forest (~0.8 – 1.6 km^2 fetch) and that assumptions of the eddy covariance technique are met (Fulgham et al., 2019).

We distinguish flux periods that are "wet" versus "dry" following Altimir et al. (2006). A flux period is considered "wet" if: (1) precipitation exceeds 0 cm hr^{-1}, (2) relative humidity (RH) exceeds 70%, or (3) either condition 1 or 2 was met within the previous 12 hours. All other flux periods are "dry". We exclude flux periods with temperatures at or below 10°C, in which condensed water could occur as ice or snow. We account for differences in air temperature and leaf surface temperature by choosing a freezing temperature threshold higher than 0°C. Of 1073 flux periods above freezing temperatures during SPiFFY, 329 (31%) were wet and 744 (69%) were dry.

A2.3 Volumetric phase ratios

Volumetric phase ratios are calculated assuming evenly distributed, 50 nm thick organic (X_{org}) and water (X_w) films on canopy surfaces. We assume a surface to volume ratio ($\frac{S}{V}$) of 0.0713 m^{-1}. Fractional phase ratios of 99:1, 90:10, 50:50, 10:90, and 1:99 are calculated for the interface of each phase on the plot using the appropriate ratios of equations 1 – 3 in the main text.

$$\frac{V_{org}}{V_{gas}} = X_{org} \times \frac{S}{V} \quad \text{(A3)}$$

$$\frac{V_w}{V_{gas}} = X_w \times \frac{S}{V} \quad \text{(A4)}$$

$$\frac{V_{org}}{V_w} = \frac{X_{org}}{X_w} \quad \text{(A5)}$$

Appendix A2 Figures

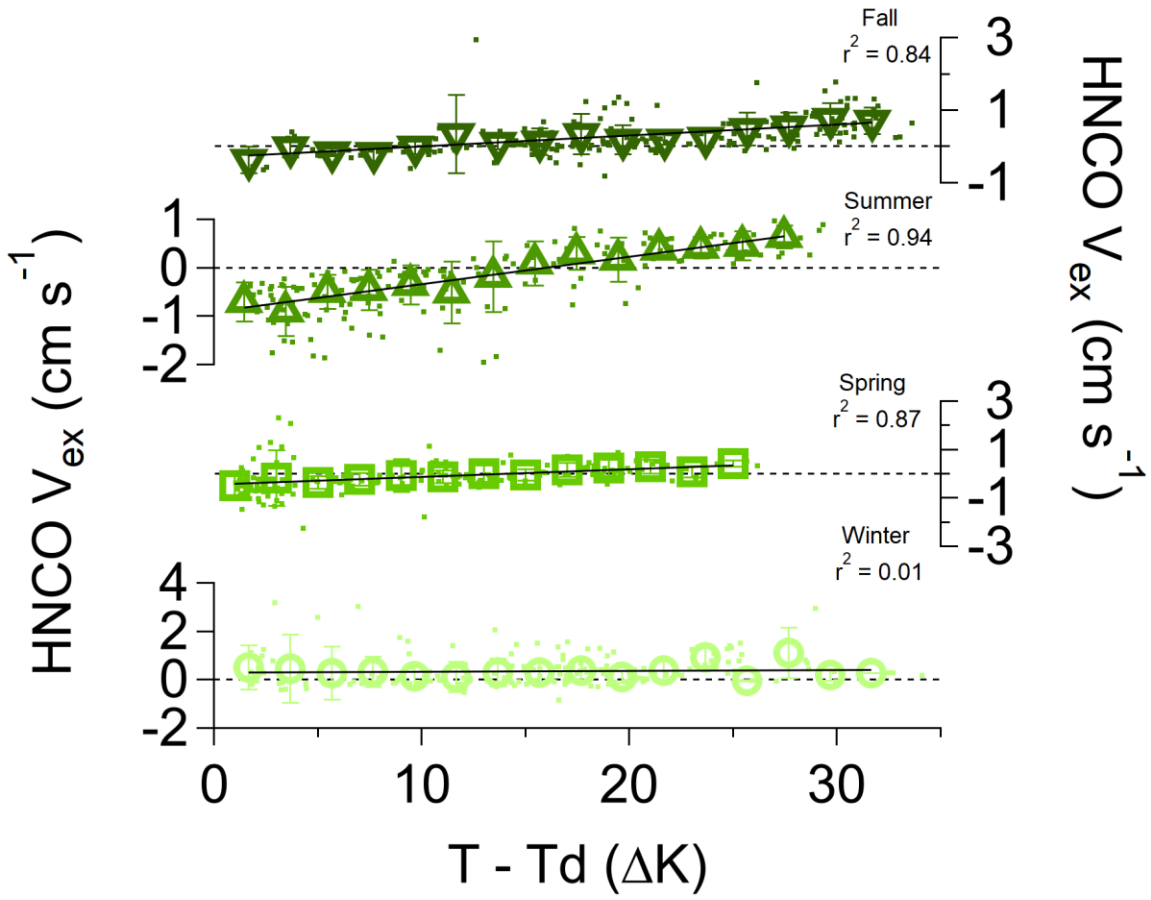

Figure A2.1. HNCO V_{ex} exhibit strong linear correlations with T-T_d at MEFO during all seasons except for winter. Data (small squares) are averaged into 20 evenly spaced T-T_d bins (large hollow shapes) based on the range of T-T_d values. Whiskers represent standard deviations.

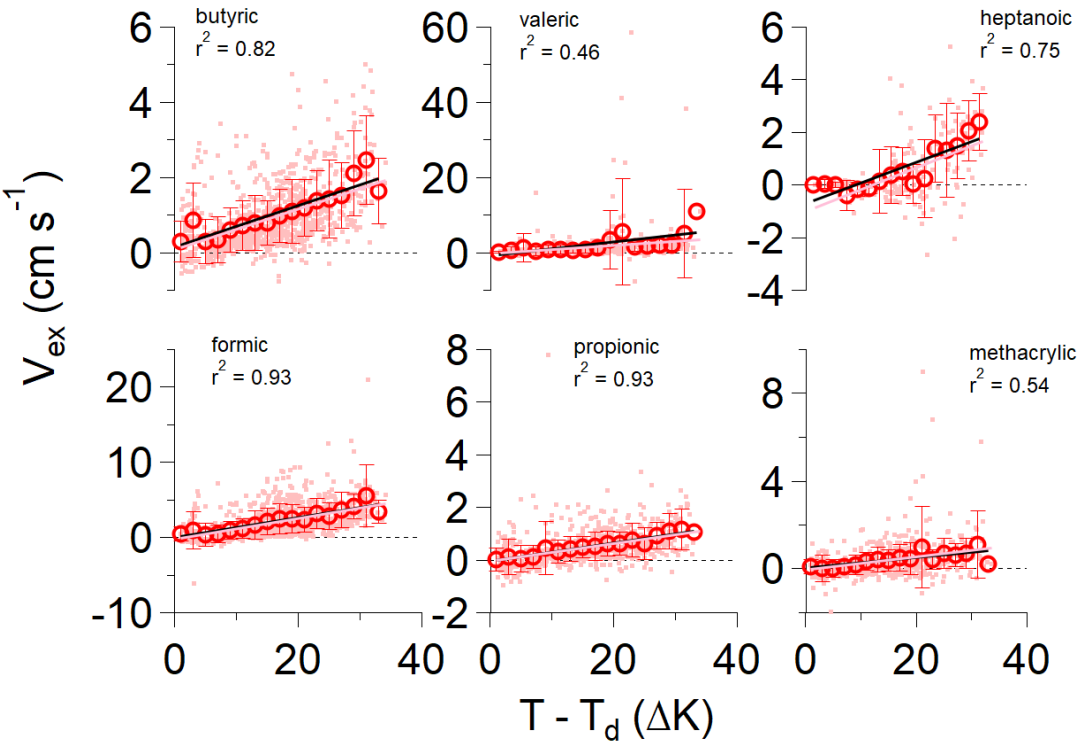

Figure A2.2. Exchange velocities (V_{ex}) of six volatile organic acids increase linearly with dew point depression ($T-T_d$) at the Manitou Experimental Forest Observatory (MEFO) pine forest site. Dots represent all data, and open circles are the averages of 20 evenly spaced $T-T_d$ bins with corresponding standard deviations. All the data (pink lines) and binned data (black lines) are each fit with linear least squares regressions. Correlation coefficients are shown for binned data.

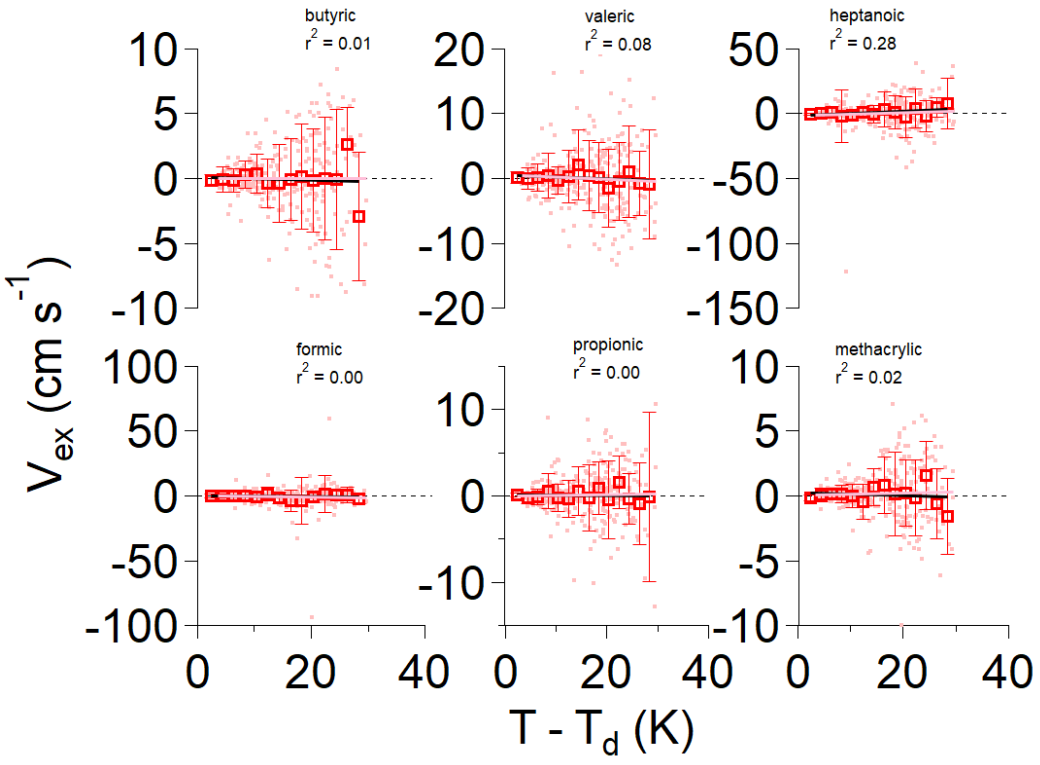

Figure A2.3. Exchange velocities (V_{ex}) of six volatile organic acids increase linearly with dew point depression ($T-T_d$) at the California orange orchard site. Dots represent all data, and open circles are the averages of 20 evenly spaced $T-T_d$ bins with corresponding standard deviations. All the data (pink lines) and binned data (black lines) are each fit with linear least squares regressions. Correlation coefficients are shown for binned data.

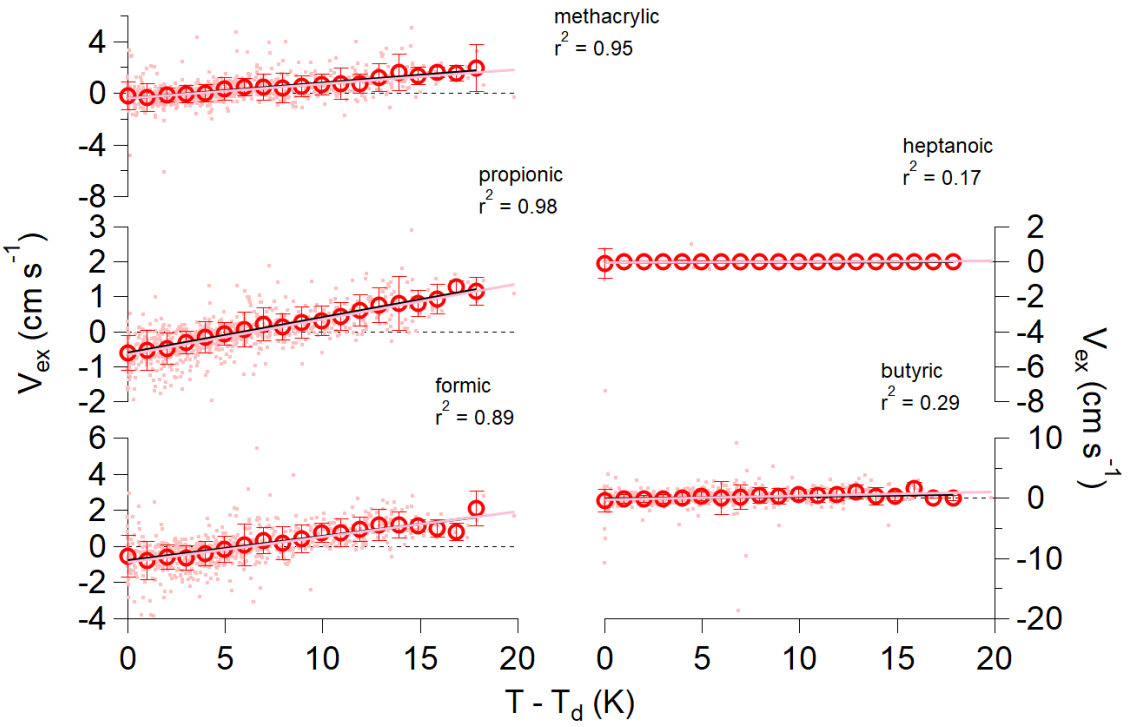

Figure A2.4. Exchange velocities (V_{ex}) of six volatile organic acids increase linearly with dew point depression ($T-T_d$) at the University of Michigan Biological Station (UMBS) mixed forest site. Dots represent all data, and open circles are the averages of 20 evenly spaced $T-T_d$ bins with corresponding standard deviations. All the data (pink lines) and binned data (black lines) are each fit with linear least squares regressions. Correlation coefficients are shown for binned data.

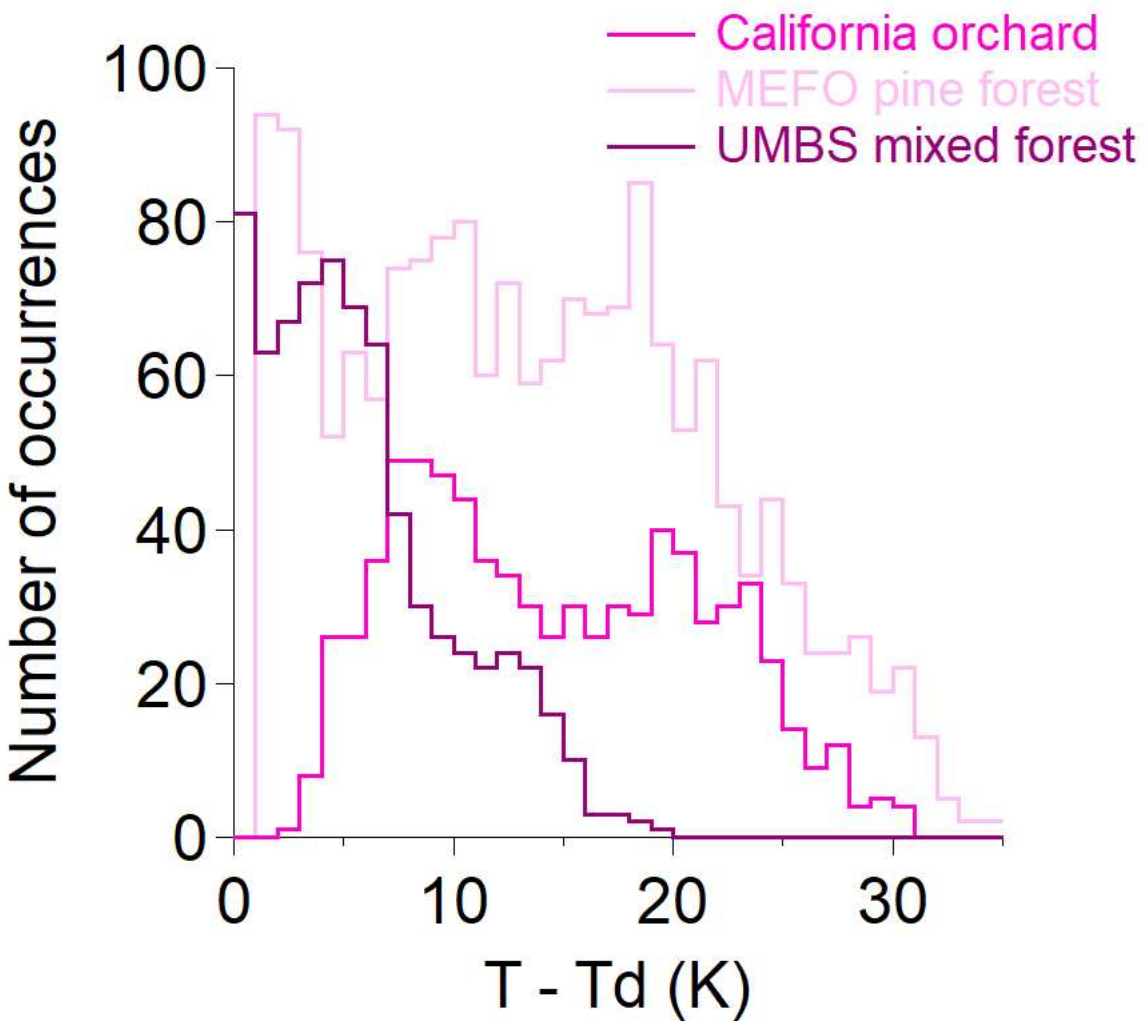

Figure A2.5. Pine forest at MEFO and mixed canopy forest at UMBS sites exhibit low T-T_d (< 5 ΔK) frequently, while California orange orchard flux periods rarely experience the wettest T-T_d values. Histograms are averaged to 35 evenly spaced bins.

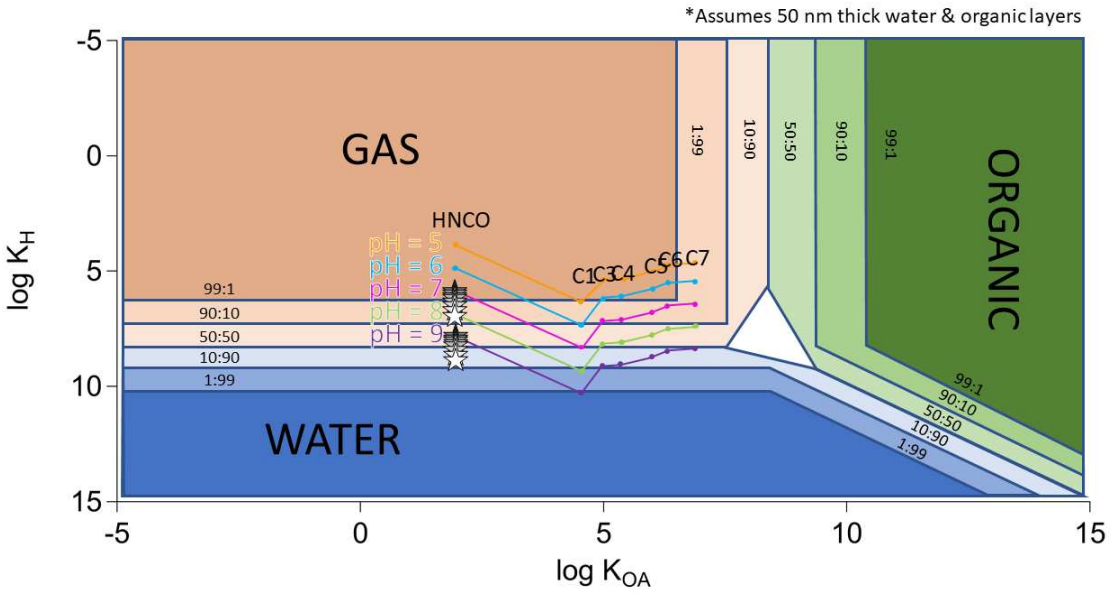

Figure A2.6. Partitioning space plot represents the volatility distribution of isocyanic acid (HNCO) and different alkanoic organic acids (C1 for formic acid, C3 for propionic acid, etc.) at MEFO. Stars represent the aqueous solubility enhancement of HNCO at lower temperatures. Shown here are temperatures -10°C (white) to 30°C (dark gray) in 5°C increments. Temperature-dependent changes in organic phase solubility are not included. pH isopleths are connected to guide the eye. All data shown are at standard pressure.

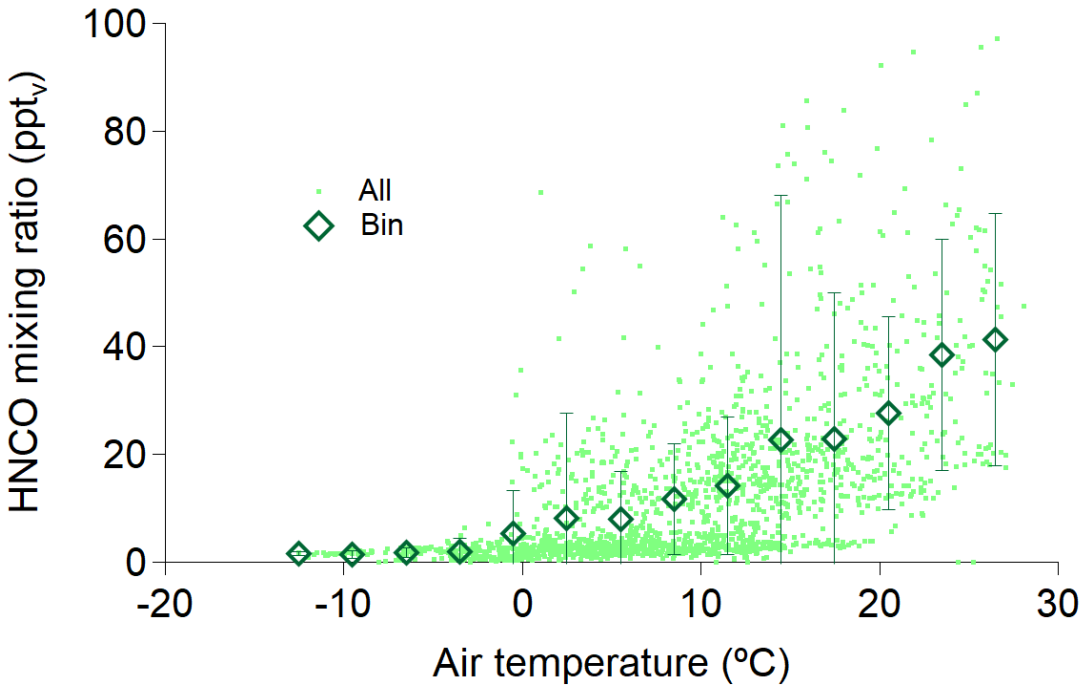

Figure A2.7. Ambient HNCO mixing ratios increase with increasing air temperature. Diamonds represent HNCO averages over 20-evenly-spaced temperature bins, and whiskers are standard deviation.

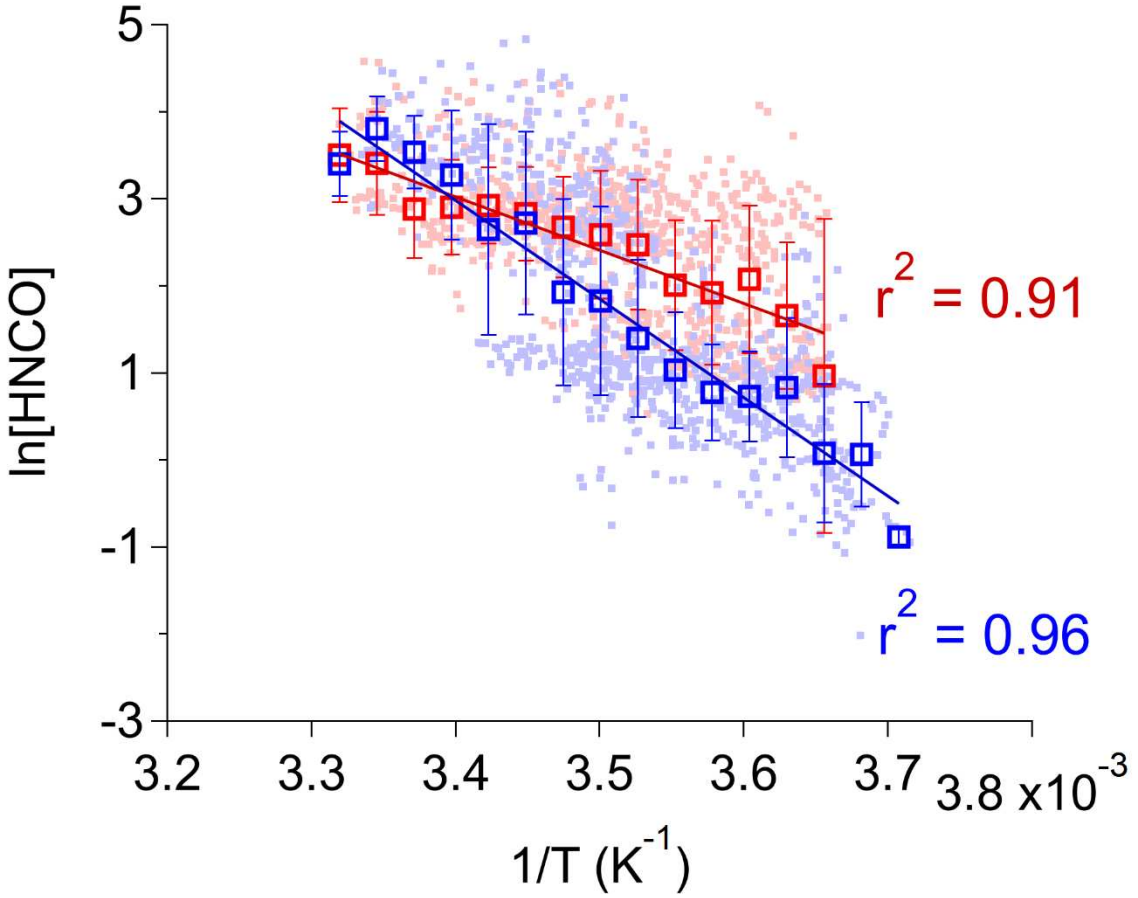

Figure A2.8. Binned natural logarithms of HNCO mixing ratios linearly depend upon inverse temperatures measured at MEFO during both wet (blue) and dry (red) periods. Data (small squares) are averaged into 20 evenly spaced 1/T bins. Whiskers represent standard deviations associated with the bin averages. Wet and dry sorting follows the algorithm description in section 3.2.3.

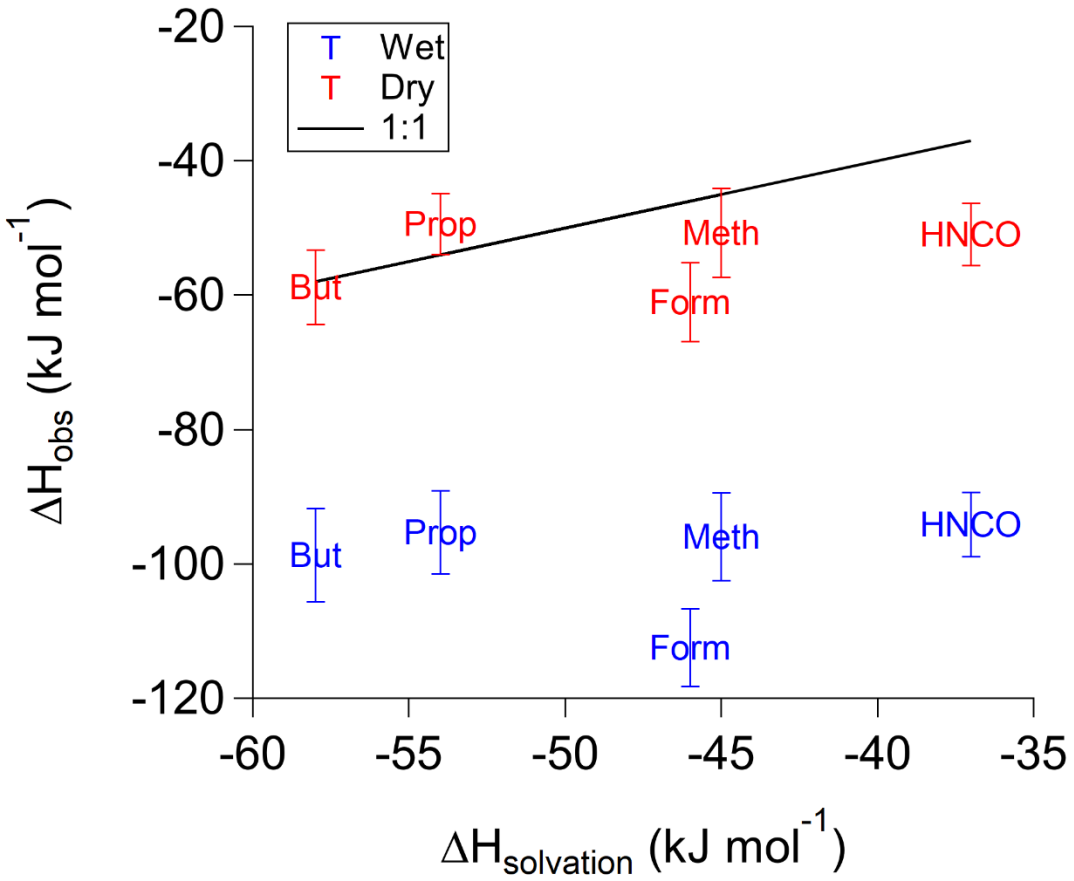

Figure A2.9. Observed enthalpies of solvation (ΔH_{obs}) for five acids (HNCO, formic, propionic, butyric, and methacrylic acids) are similar to intrinsic literature values ($\Delta H_{solvation}$) when the forest is dry (red), but not when wet (blue). Under wet conditions, ΔH_{obs} is more exothermic and favors aqueous partitioning.

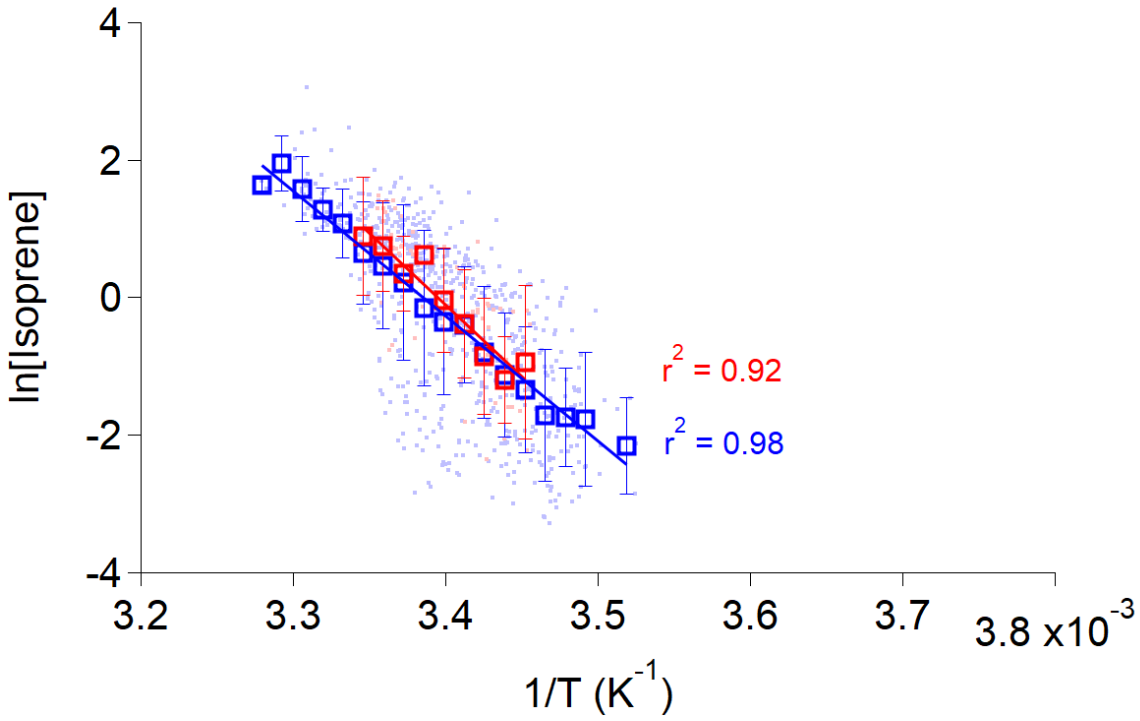

Figure A2.10. Modified van't Hoff plot for isoprene measured at University of Michigan Biological Station (Alwe et al., 2019). Data are sorted into periods with (blue) and without (red) surface wetness according to Altimir et al. (2006). Linear regressions of evenly spaced binned data agree within uncertainty: $\ln[Isoprene]_{wet} = (-18200 \pm 600) \times \frac{1}{T} + (61.5 \pm 2)$; $\ln [Isoprene]_{dry} = (-20800 \pm 2000) \times \frac{1}{T} + (70.7 \pm 8)$.

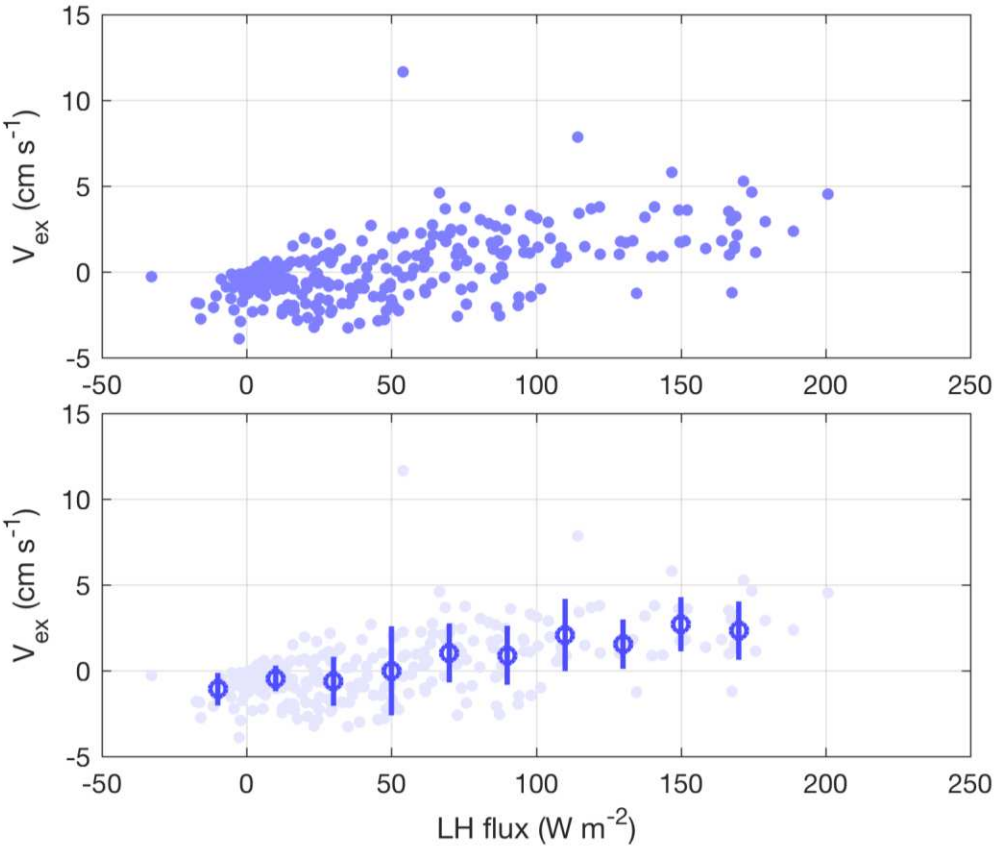

Figure A2.11. Formic acid exchange velocity (V_{ex}) increases with latent heat flux (LH) at SMEAR 2 in Hyytiälä, Finland. Data are flux-quality filtered according to Schobesberger et al. (2016). Open circles in bottom panel represent 20 W m^{-2} binned averages with whiskers as standard deviations.

Appendix A2 Tables

Table A2.1. The average sensitivity across all flux periods is listed for measured VOAs at 5 Hz data acquisition frequency. Calculation of HNCO sensitivities is described in section 3.2.2.

Volatile organic acid	0.2 s Campaign Average Sensitivity (ncps ppt^{-1})
$C_4H_8O_2$	230
HCOOH	460
$C_3H_6O_2$	150
$C_4H_6O_2$	450
$C_5H_{10}O_2$	46
$C_7H_{14}O_2$	9.9
HNCO	1700

Table A2.2. Equations for best-fit curves for 6 volatile organic acid exchange velocities (V_{ex}) as a function of dew point depression ($T-T_d$). See Fig. 3 for visual representation of propionic acid, which represent the general trends.

Acid name	Best-fit line	Slope (cm s^{-1} K^{-1})	Intercept (cm s^{-1})	r^2
Propionic	California orchard (all)	0.0061 ± 0.02	0.034 ± 0.4	0.00
	California orchard (bin)	-0.19 ± 0.03	0.22 ± 0.5	0.04
	UMBS mixed forest (all)	0.10 ± 0.004	-0.66 ± 0.03	0.47
	UMBS mixed forest (bin)	0.10 ± 0.003	-0.56 ± 0.03	0.99
	MEFO pine forest (all)	0.034 ± 0.002	-0.054 ± 0.05	0.18
	MEFO pine forest (bin)	0.035 ± 0.002	-0.036 ± 0.05	0.93
Formic	California orchard (all)	-0.037 ± 0.08	-0.10 ± 1	0.00
	California orchard (bin)	-0.014 ± 0.06	-0.30 ± 1	0.00
	UMBS mixed forest (all)	0.14 ± 0.008	-0.89 ± 0.06	0.32
	UMBS mixed forest (bin)	0.13 ± 0.01	-0.77 ± 0.1	0.89
	MEFO pine forest (all)	0.14 ± 0.008	-0.24 ± 0.1	0.25
	MEFO pine forest (bin)	0.13 ± 0.01	-0.029 ± 0.3	0.87
Butyric	California orchard (all)	0.00022 ± 0.03	-0.0029 ± 0.4	0.00

	California orchard (bin)	-0.0095 ± 0.04	0.072 ± 0.7	0.01
	UMBS mixed forest (all)	0.068 ± 0.01	-0.26 ± 0.09	0.04
	UMBS mixed forest (bin)	0.044 ± 0.02	-0.088 ± 0.2	0.29
	MEFO pine forest (all)	0.054 ± 0.003	0.078 ± 0.06	0.24
	MEFO pine forest (bin)	0.055 ± 0.007	0.15 ± 0.1	0.82
Valeric	California orchard (all)	-0.036 ± 0.04	0.60 ± 0.6	0.00
	California orchard (bin)	-0.030 ± 0.03	0.53 ± 0.5	0.08
	UMBS mixed forest (all)	n/a	n/a	n/a
	UMBS mixed forest (bin)	n/a	n/a	n/a
	MEFO pine forest (all)	0.083 ± 0.01	-1.0 ± 0.3	0.03
	MEFO pine forest (bin)	0.18 ± 0.05	-0.87 ± 1	0.46
Methacrylic	California orchard (all)	0.0091 ± 0.02	0.022 ± 0.3	0.00
	California orchard (bin)	-0.012 ± 0.02	0.27 ± 0.4	0.02
	UMBS mixed forest (all)	0.11 ± 0.008	-0.37 ± 0.06	0.21
	UMBS mixed forest (bin)	0.12 ± 0.007	-0.38 ± 0.07	0.95

	MEFO pine forest (all)	0.000026 ± 0.00005	0.37 ± 0.06	0.00
	MEFO pine forest (bin)	0.024 ± 0.006	0.034 ± 0.1	0.54
Heptanoic	California orchard (all)	0.12 ± 0.1	-1.4 ± 2	0.00
	California orchard (bin)	0.19 ± 0.09	-1.83 ± 2	0.28
	UMBS mixed forest (all)	0.0033 ± 0.003	-0.030 ± 0.02	0.00
	UMBS mixed forest (bin)	0.0017 ± 0.0009	-0.019 ± 0.009	0.17
	MEFO pine forest (all)	0.083 ± 0.01	-1.02 ± 0.3	0.23
	MEFO pine forest (bin)	0.078 ± 0.01	-0.71 ± 0.2	0.75

Appendix A3 Figures

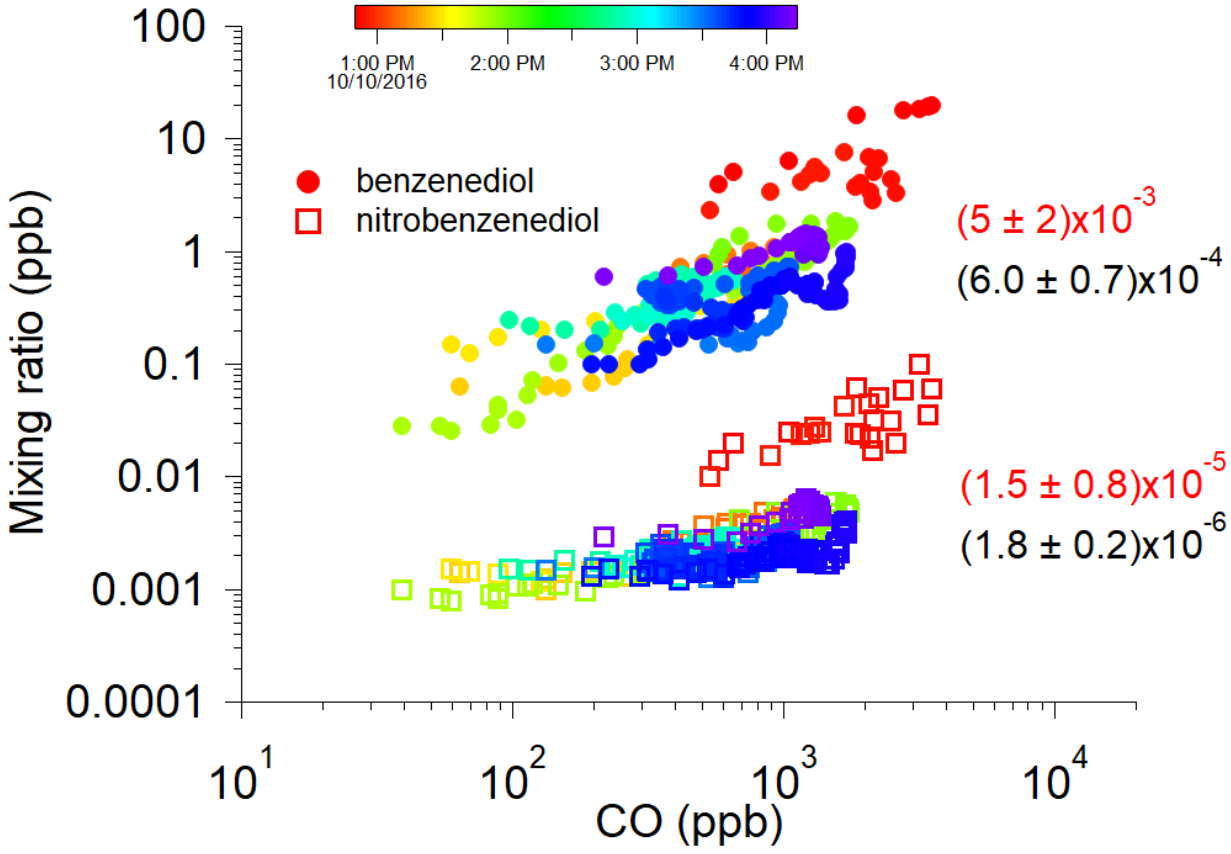

Figure A3.1. Mixing ratios of benzendiol (circles) and nitrobenzenediol (squares) increase as a linear function of CO. Mixing ratios at the start of the burn (red markers) are the highest of the fire for both compounds. Emission ratios (ERs) are significantly higher at the 95% confidence interval during the initial (red text) than remainder (black text) of the fire.

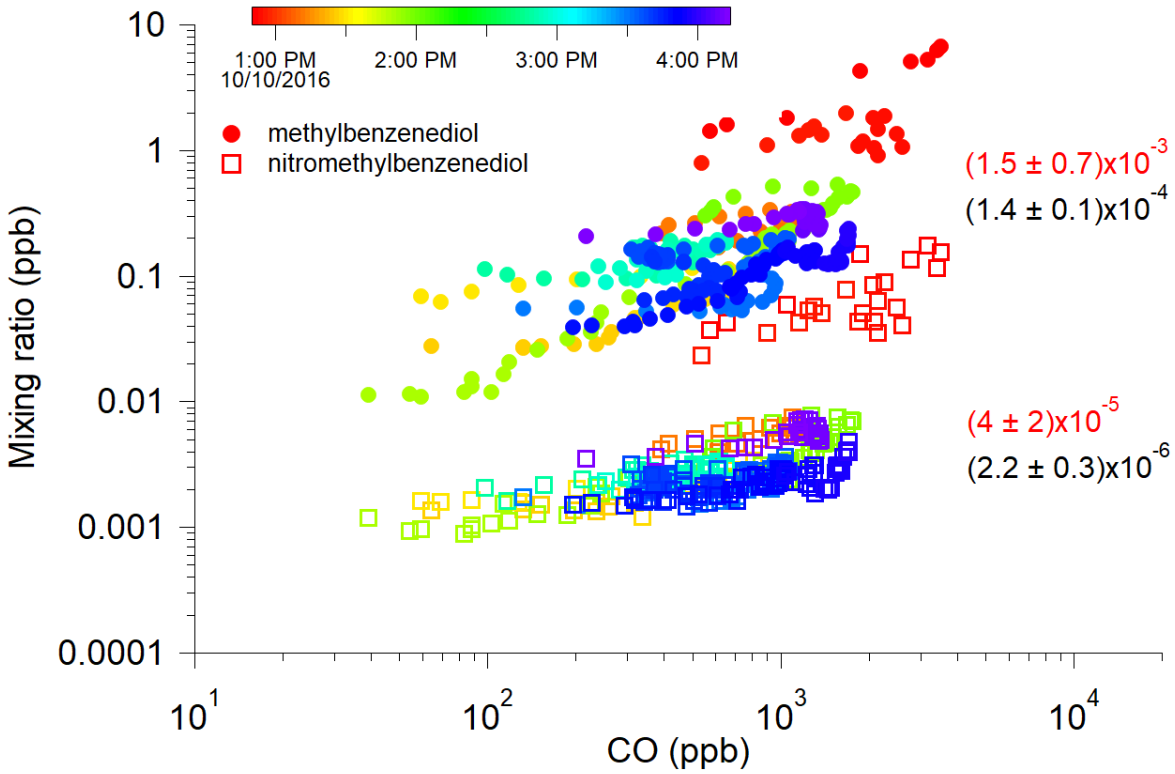

Figure A3.2. Mixing ratios of methylbenzenediol (circles) and nitromethylbenzenediol (squares) increase as a linear function of CO. Mixing ratios at the start of the burn (red markers) are the highest of the fire for both compounds. Emission ratios (ERs) are significantly higher at the 95% confidence interval during the initial (red text) than remainder (black text) of the fire.

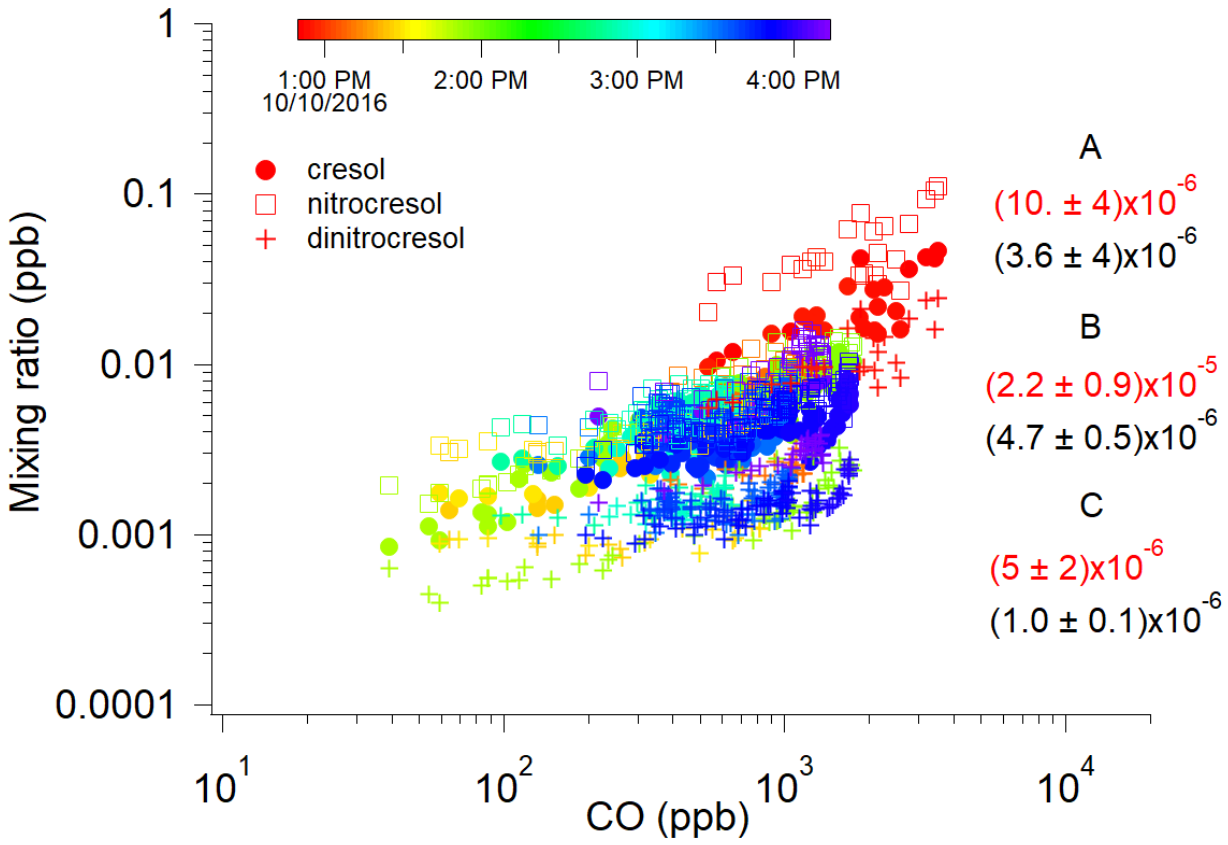

Figure A3.3. Mixing ratios of cresol (circles, A), nitrocresol (squares, B), and dinitrocresol (crosses, C) increase as a linear function of CO. Mixing ratios at the start of the burn (red markers) are the highest of the fire for all compounds. Except for cresol, emission ratios (ERs) are significantly higher at the 95% confidence interval during the initial (red text) than remainder (black text) of the fire.

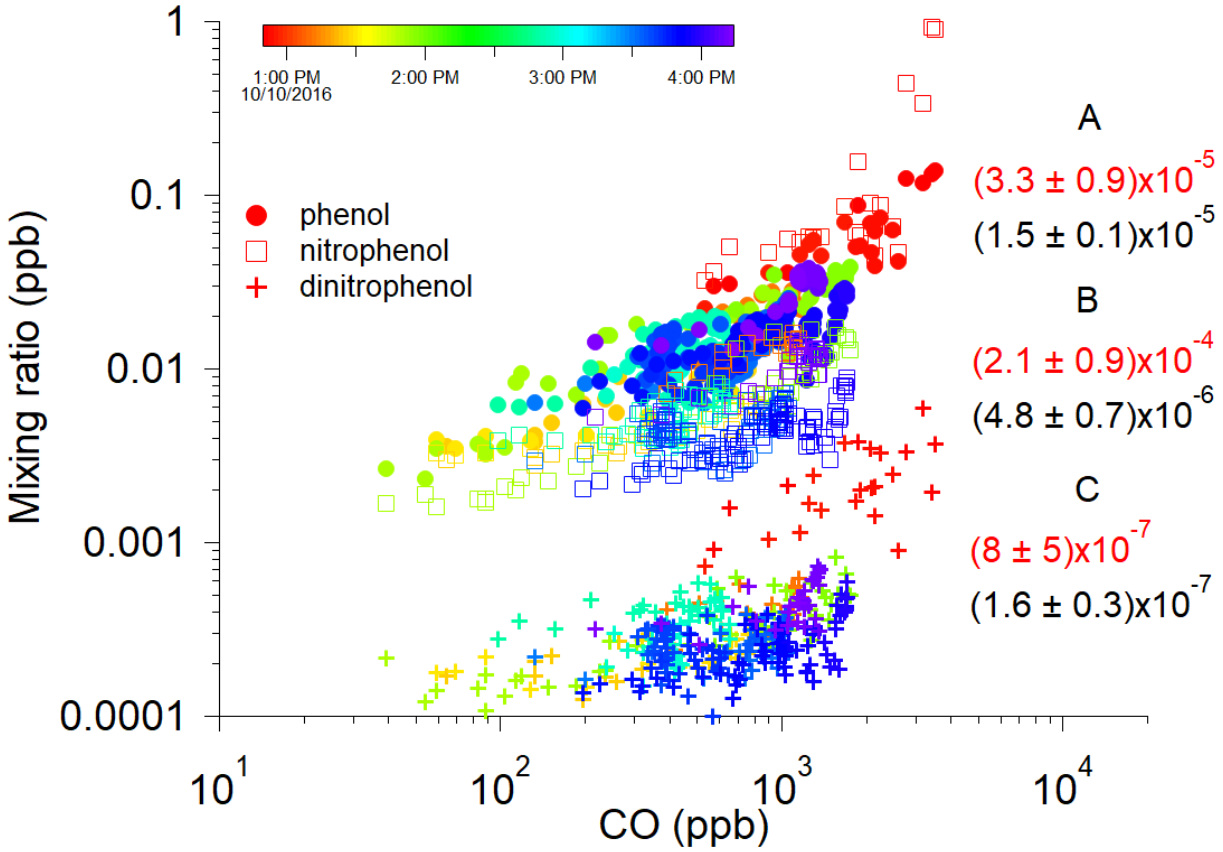

Figure A3.4. Mixing ratios of phenol (circles, A), nitrophenol (squares, B), and dinitrophenol (crosses, C) increase as a linear function of CO. Mixing ratios at the start of the burn (red markers) are the highest of the fire for all compounds. Except for phenol, emission ratios (ERs) are significantly higher at the 95% confidence interval during the initial (red text) than remainder (black text) of the fire.

Figure A3.5. Photo of Manitou Experimental Forest Observatory (MEFO) shows the two separate locations where inlets were installed: the tower site and ground site. Sites were horizontally separated by ~15 m.